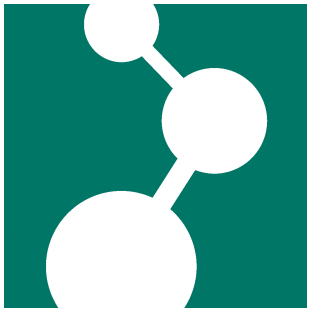

Stress & Structure of thin Polymer Brush Films

Dissertation

zur Erlangung des Grades
"Doktor der Naturwissenschaften"
im Promotionsfach Chemie

am Fachbereich Chemie, Pharmazie und Geowissenschaften
der Johannes Gutenberg-Universität Mainz

Jannis Walther Ochsmann
geboren in Münster/Westfalen
Mainz, Mai 2012

Contents

Abstract

Polymer brushes have unique properties with a large variety of possible applications ranging from responsive coatings and drug delivery to lubrication and sensing. For further development a detailed understanding of the properties is needed. Established characterization methods, however, only supply information of the surface. Experimental data about the inner "bulk" structure of polymer brushes is still missing.

Scattering methods under grazing incidence supply structural information of surfaces as well as structures beneath it. Nanomechanical cantilevers supply stress data, which is giving information about the forces acting inside the polymer brush film. In this thesis these two techniques are further developed and used to deepen the understanding of polymer brushes.

The experimental work is divided into four chapters. Chapter 2 deals with the preparation of polymer brushes on top of nanomechanical cantilever sensors as well as large area sample by using a "grafting-to" technique.

The further development of nanomechanical cantilever readout is subject of chapter 3. In order to simplify cantilever sensing, a method is investigated which allows one to perform multiple bending experiments on top of a single cantilever. To do so, a way to correlate different curvatures is introduced as well as a way to conveniently locate differently coated segments.

In chapter 4 the change in structure upon solvent treatment of mixed polymer brushes is investigated by using scattering methods and nanomechanical cantilevers amongst others. This allows one to explain the domain memory effect, which is typically found in such systems.

Chapter 5 describes the implementation of a phase shifting interferometer - used for readout of nanomechanical cantilevers - into the μ-focused scattering beamline BW4, allowing simultaneous measurements of stress and structure information.

The last experimental chapter 6 deals with the roughness correlation in polymer brushes and its dependence on the chain tethered density.

In summary, the thesis deals with utilization of new experimental techniques for the investigation of polymer brushes and further development of the techniques themselves.

1. Introduction

1.1 General introduction

Polymer chains physically attached to a surface - also known as polymer brushes- are a field of research, which is receiving a lot of interest from a theoretical, fundamental and applied science point of view. The interest stems from the unique characteristics of polymer brushes compared to an unbound thin polymer film.

The progress in controlled radical polymerization opened a pathway to obtain polymer brushes with a defined molecular weight while keeping the experimental effort at a manageable level.[1] By this means, a huge variety of different polymer brushes, with different physical and chemical properties, have been synthesized.[2]

The most obvious advantage of polymer brushes, when compared to an unbound polymer film, is its increased stability against solvents, simply because of the fact, that due to their physical connection to the substrate, they cannot be dissolved. However, in the recent years many other unique features of polymer brushes have been identified. One of them is its increased stability against mechanical wear.[3] This is important for nano- and micromechanical systems with moving parts for example data storage systems or lithography based on scanning probe techniques.[4-7] For larger surface areas these properties can be used as lubrication. When rubbed against each other, two polymer brush coated surfaces show orders of magnitude lower friction, when compared to uncoated or surfaces coated with unbound polymer.[8, 9] Raviv et al. demonstrated this with polyelectrolyte brushes which might be used for artificial implants.[10]

In the field of biotechnology, polymer brushes are used for molecular recognition, biosensing and protein separation.[11] Andruzzi et al. for example used oligo(ethylene glycol) containing polymer brushes to suppress protein absorption and nonspecific cell adhesion.[12]

Especial interest is centered on the behavior and possibilities of responsive polymer brushes.[13-16] Upon an external stimulus, e.g. change in temperature or pH, the conformation of the polymer brush is changed. This can be used to alter the

properties of the polymer brush coated surface to release substances or to detect the external stimulus itself.

Despite of the advantageous properties and the advance in synthesis, the applications of polymer brushes are still in its infancy. In order to mature not only a further development in polymer brushes synthesis but also a detailed understanding of the properties itself is needed.[17]

Theoretical studies have come a long way in predicting and scaling the behavior of homopolymer[18, 19] as well as mixed polymer[20] and other responsive polymer[13] brushes. Experimental studies, however, have been mainly limited to the investigation of the surface properties of the polymer brush. A large variety of methods like scanning probe microscopy (SPM), Fourier transform infrared (FT-IR) spectroscopy, X-ray photoelectron spectroscopy (XPS), scanning electron microscopy (SEM) and contact angle measurement[17] yield only structural and chemical information of the upper most layer. Experimental data on the inner "bulk" structure is sparse. This is mainly because of the small sample volume. When investigating polymer brushes someone usually deals with film thicknesses in the nm-range and polymer amounts in the range of µg.

Scattering methods under gracing incidence allow one to gain information of the surface as well as the structure beneath it. The film thickness and roughness of the investigated thin film can be obtained by X-ray reflectivity (XRR). To achieve more detailed structural information, especially about lateral structures, one has to investigate the diffuse scattering. This is done by grazing incidence small angle scattering (GISAXS). Although gaining popularity, this method is far from being standard in the investigation of polymer films. This is mainly because of the needed high X-ray intensity, typically only available at synchrotron light sources and the required data analysis.

A completely different approach to gain information about the inner structure of polymer brushes are nanomechanical cantilevers (NMCs).[21] By analyzing the bending of NMCs coated with polymer brushes information about forces acting inside the polymer brushes can be gained.[22, 23] In combination with structural information this allows to draw further conclusions on the inner structure.

1.2 Aim

To deepen the understanding of polymer brushes, further information of the inner structures is needed. Therefore the aim of this work is to use scattering method as well as NMCs to deepen the understanding of polymer brush systems. NMCs are a powerful, but so far a rarely used tool in the investigation of polymer brush systems. Therefore another goal of this work is to improve and simplify the readout of NMCs.

1.3 Outline

The following chapter introduces the theoretical background and the experimental methods of polymer brushes as well as the methods used for structural and stress evaluation.
In order to investigate mixed polymer brushes on NMC sensors, a method was needed to coat the NMC single sidedly. To do so, a "grafting-to" approach was developed. The required synthesis of an active-ester end-functionalized polymer and the developed "grafting-to" method is described in chapter 3.
To perform the bending experiments, required for stress calculation, a phase shifting interferometer (PSI) was assembled. In collaboration with the University of Genoa software was programmed to perform the measurement and analysis of the NMC. In chapter 4 the setup was used to investigate the possibilities of local NMC readout in an effort to simplify NMC readout.
In the succeeding chapter 5, polystyrene-poly(methyl methacrylate) mixed polymer brushes are studied. In order to gain a deeper inside into the reason for the observed change in structure upon treatment with selective and nonselective solvents, a detailed structure investigation as well as stress measurements were performed.
In chapter 6 the feasibility of simultaneous investigation of NMC arrays by phase shifting interferometry setup and X-ray scattering methods is explored. The

presented PSI was, therefore, integrated into the synchrotron small angle scattering beamline BW4, HASYLAB, DESY.

The last chapter 7 deals with the investigation of roughness correlation in polymer brushes. By GISAXS measurements multiple polymer brush samples with varying grafting densities were investigated.

The thesis concludes with a summary of the main results and an outlook integrated in the concluding remarks.

2. Fundamentals & methods

2.1 Polymer brushes

A *polymer brush* is the notation for a group of polymer chains attached to a solid surface. By tethering the polymer to the surface its properties are altered compared to the unattached polymer film. The different behavior has two reasons first, the tethering of the chains itself, and secondly, the close proximity to neighboring chains cause the polymer chains to stretch away from the surface.
One main characteristic of a polymer brush is the distance between the grafting points of two adjacent polymer chains. In this work the distance is expressed as the grafting density Γ, which is defined as number of chains occupying a certain area,

$$\Gamma = \frac{1}{A} \quad \textbf{(1)}$$

with A being the area occupied by one grafted polymer chain. The grafting density can be calculated by using the formula,

$$\Gamma = \frac{d\rho N_A}{M_n} \quad \textbf{(2)}$$

with d being the film thickness, ρ bulk density of the polymer, N_A the Avogadro number and M_n the number average molecular weight, as obtained by XRR and Gel permeation chromatography (GPC) measurements, respectively.
A single chain grafted is commonly referred to as a *mushroom*. When the distance between two adjacent chains approaches the size of the polymer chain, the grafted chains start to overlap and the film becomes a polymer brush. This is referred to as the *brush-mushroom transition*. A quantitative measure for this is the chain tethered density,

$$\Sigma = \Gamma \pi R_g^2 \quad \textbf{(3)}$$

with R_g being the radius of gyration of an untethered chain. The obtained values can be interpreted as the number of chain occupying an area that a free non overlapping polymer chain would normally occupy.[24] Due to fluctuation in grafting density and molecular weight, a clear transition from a mushroom to a brush at the values of $\Sigma \geq 1$ is not observed. In literature varying values for the start of overlap and the resulting stretching of polymer chains can be found, differing from investigated polymers as well as in the used experimental methods[25, 26]. In an effort to clarify the matter Brittain and Minko et al. suggest a differentiation in three regime: $\Sigma < 1$ = mushroom-regime; $1 < \Sigma < 5$ = mushroom-to-brush transition and $\Sigma > 5$ = brush regime.[24] For consistency, all tethered polymer chains are called brushes in this thesis.

2.1.1 Theory

The first who described the polymer brushes in a good solvent theoretically are Alexander[27] and de Gennes.[18] To avoid unfavorable segment-segment interactions, due to the close proximity of the chains, the chains stretch away from the surface. However, by doing so the polymer chains reduce their number of possible conformations, in other words, the chains lose conformational entropy. By stretching away from the surface, the polymer chain also increases the favorable interaction between polymer segments and solvent molecules. The free energy of the polymer brush F can, therefore, be described as the sum of the internal energy F_{int} and the elastic energy F_{el}.

$$F = F_{\text{int}} + F_{el} \quad \textbf{(4)}$$

In their model Alexander and de Gennes assumed a step-like density profile of the polymer brush leading to a constant density inside the polymer brush. They also

assumed that all polymer chains are equally stretched resulting in the polymer chain ends to be at an equal distance to the surface (Figure 2.1A).
In a further development of the Alexander-de Gennes model, Milner, Witten and Cates[19, 28] used self-consistent field theory. By this means, they obtained a parabolic density profile, which allowed the polymer chain end to be at an arbitrary position (Figure 2.1B).

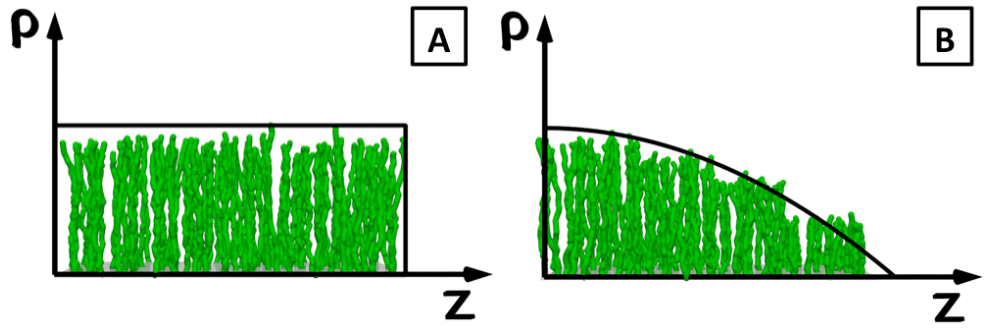

Figure 2.1: Density profiles and schematic representation of the Alexander-deGennes and Milner-Witten-Cates brush model.

Both models predict a linear dependency of the film thickness on the number of segments N and, therefore, on the molecular weight of the grafted polymer chains M_n.

$$d \propto N \propto M_n \qquad \textbf{(5)}$$

2.1.2 "Grafting-from"

In a "grafting-from" approach a polymer brush is obtained by "growing" the polymer away from the surface (Figure 2.2A). This is done using an initiator-functionalized surface and polymerization of the monomer on top of the surface. Numerous polymerization methods have been used in this way.[1] In recent years "grafting-from"-techniques using living radical polymerization, especially ATRP (Chapter 2.3.2), have become popular. This is due to the ability to obtain grafted

polymers with narrow molecular weight distributions and straightforward experimental procedures.[29]

The biggest advantage of the "grafting-from" technique is the high grafting density of the obtained polymer brushes. During the polymerization the already polymerized monomer is swollen by the monomer/solvent solution. This allows the monomer to freely diffuse to the growing chain end and continue the reaction. Only at high grafting densities and molecular weight distributions the diffusion gets hindered and the polymerization is stopped.

2.1.3 "Grafting-to"

In a "grafting-to" approach a polymer brush is obtained by attaching an already polymerized chain to a surface (Figure 2.2B). To do so, usually a functionalized polymer is attached to a surface carrying a complimentary functional group. The biggest advantages are the simple synthesis and characterization of the used polymers. Typically, the used polymers are obtained by living polymerization techniques by using either a functionalized starter or stopping the polymerization with a specific reactant, the end-functionalization is achieved. The consecutive "grafting-to" step can be performed in solution or melt, where usually higher grafting densities are obtained. Compared to the "grafting-from" approach only polymer brushes with lower grafting densities are achieved.

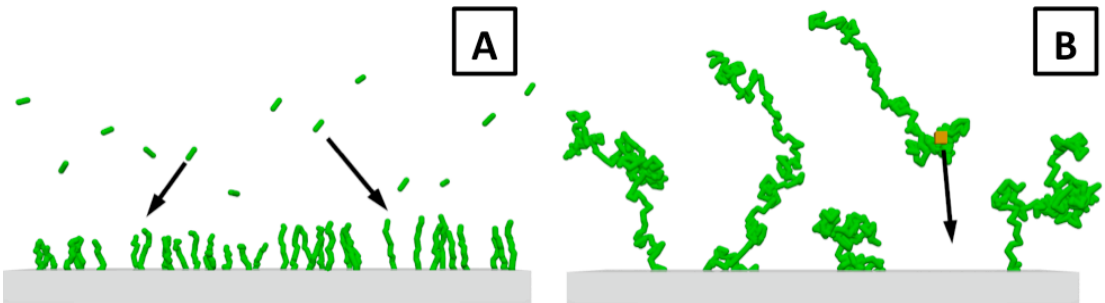

Figure 2.2: Schematic representation of the "grafting-from"(A) and "grafting-to" (B) preparation methods for polymer brushes.

2.2 Mixed polymer brushes

Mixed polymer brushes are composed of two different polymers attached to the same surface. Because of the immiscibility of the polymers, micro phase separation between the two polymers occurs. This adds an additional force to the still present conformational penalties due to the brush state.

Mixed polymer brushes can be obtained, like normal homopolymer brushes, by "grafting-from" as well as "grafting-to" approaches.

Zhao et al.[30-33] used a mixed initiator self-assembled monolayer (SAM) in a "grafting-from" approach. By using two different living radical polymerization methods (Chapter 2.3) they were able to consecutively polymerize two different polymers from the same surface.

To obtain mixed brushes by a "grafting-to" approach, usually two end-functionalized homopolymers are applied to the same surface. Minko et al.[34-36] used carboxyl-terminated polymers attaching them to an epoxy-functionalized surface. To do so, a precursor polymer film was spin-coated on the surface. By heating the precursor film above its glass transition temperature, the carboxyl-groups could react with the epoxy-groups thereby attaching the polymer chain to the surface. By adjusting the time of heating, the grafting density of the resulting "grafted-to" homopolymer film could be altered. After extraction of excess unbound polymer, the second homopolymer is applied via the same way. The second homopolymer now binds with the remaining epoxy groups. After extracting the unbound homopolymer, the mixed polymer brush film is obtained.

The scientific as well as commercial interest in mixed polymer brushes stem from their response to external stimuli.[13] When exposing mixed polymer brushes to a selective solvent for one of the polymers or a good solvent for both polymers, structural changes on the surface film can be observed. Zhao et al. for example treated a PMMA-PS mixed polymer brushes obtained by "grafting-from" polymerization with selective and non-selective solvents (Figure 2.3). Upon treatment with a selective solvent for PMMA, a dimple structure was formed at the

surface of the film. Upon treatment with a non-selective solvent, a flat surface was observed.

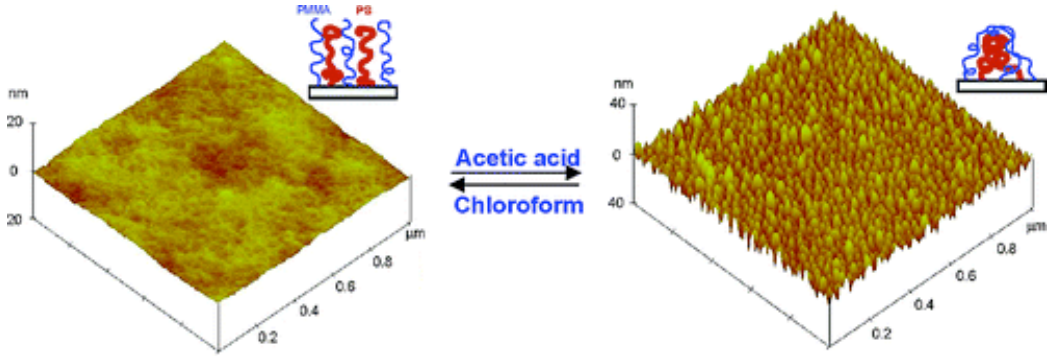

Figure 2.3: Topography image obtained from SPM measurement performed on "grafted-from" PMMA-PS mixed polymer brushes after treatment with acetic acid and chloroform. [37]

Contact angle and XPS studies showed an increase in PMMA at the surface after treatment with the selective solvent acetic acid.

Santer et al. observed a domain memory effect in "grafted-to" mixed polymer brushes. Using SPM, they imaged the same surface area after each treatment with a selective and non-selective solvent. By comparing the images obtained after treatment with a selective solvent they could find a partial reappearance of the domains. They introduced a quantified measurement for domains forming at the same position, with the same size and shape upon cyclically change. The highest memory effect was observed for mixed polymer brushes having the same molecular weight. The authors attribute the domain memory effect to small fluctuation on grafting points nucleating the domains in the mixed brushes.[38-40]

Mixed polymer brushes have also been studied theoretically. Using simulation, the dependence on grafting density, composition[41], chain-length asymmetry, solvent quality and selectivity was investigated.[20, 38, 42, 43]

Müller et al.[41, 42] studied the microphase separation of binary brushes using Single-Chain-in-Mean-Field simulations. For mixed polymer brushes with symmetric chain lengths, they got circular domain formation in films with a fraction number of 0.625-0.75 upon treatment with a good as well as a selective solvent.

While the change of surface properties is well investigated, no experimental investigation has been done on the reason for such behavior and the bulk composition of the mixed polymer brushes. In chapter 5 X-ray scattering methods and surface stress measurements will be used to obtain a better understanding of the observed switching behavior.

2.3 Living radical polymerization

Obtaining polymers by free radical polymerization is much more convenient than anionic polymerization. The requirements for the purity of the monomer and on the exclusion of water are much less stringent. Free radical polymerization is also much more tolerant in terms of functional groups, e.g. hydroxy and amine groups, and can be carried out in bulk, organic solvent and aqueous media. Because of the radical nature of the growing chains, the chain propagation is very fast compared to the chain initiation and, therefore, the rate-determining step. During a polymerization usually one chain is initiated, grows and then terminates either by recombination or disproportionation of the radical. Even at low conversion rate, high molecular weight polymer can be found. Unfortunately, this also results in a broad distribution of molecular weight after the consumption of all monomers.

In anionic polymerization the rate-determining step is the initiation itself. In theory, all chains start growing at the same time and since no termination reaction can occur all chains grow until all monomers are consumed. Therefore, polymer with a narrow molecular weight distribution can be obtained. The drawbacks of course are the high demand on purity, the limitation to aprotic solvents and monomers.

Living radical polymerization allows one to obtain polymer with narrow molecular weight distributions while keeping most of the advantages of the free radical polymerization. When looking at the anionic polymerization, two criteria have to be fulfilled. No termination reaction may occur, and all chains have to start growing simultaneously, in other words, the initiation has to be the rate-determining step. All living radical polymerization techniques do so by

transforming the growing radical chain in a dormant species. The dormant species is in equilibrium (Figure 2.4) with the radical at the end of the growing chain, with the equilibrium being mainly on the side of the dormant species. This results in a low average concentration of radicals in the reaction mixture.

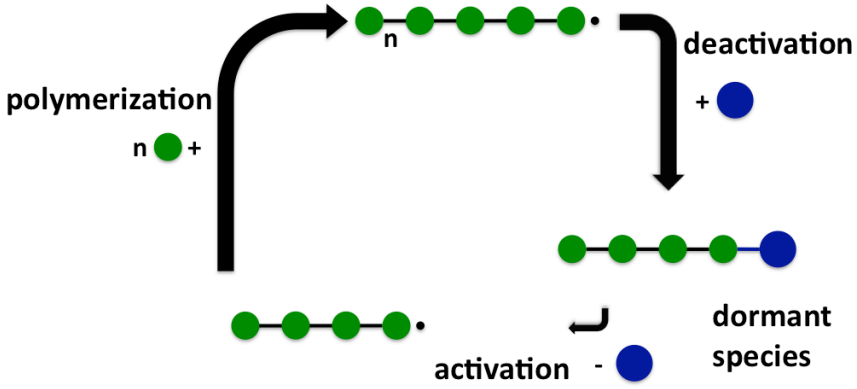

Figure 2.4: Schematic representation of the principle of living radical polymerization.

The reaction is only terminated when two radicals meet. By lowering the concentration of the radicals as done in the living radical polymerization nearly all termination reactions can be suppressed. Since the chains can only grow when they are not in the dormant state, the overall chain propagation rate is very slow. The chain initiation step, therefore, becomes the rate-determining step, and a linear increase of molecular weight is achieved. This results in a narrow molecular weight distribution, and the degree of polymerization (DP) can be calculated by initial monomer (M) and initiator (I) concentrations.

$$DP_n = \frac{[MM]_0}{[I]_0} \qquad \textbf{(6)}$$

In this work two living radical polymerization techniques were used, reversible addition-fragmentation chain transfer (RAFT) polymerization for the synthesis of active ester end-functionalized polymers and atom transfer radical polymerization for the synthesis of poly (methyl methacrylate) (PMMA) brushes.[44] Both techniques will be introduced in the following chapters.

2.3.1 Radical addition-fragmentation chain transfer polymerization

In RAFT polymerization the living character of the polymerization is achieved by the addition of a RAFT-agent to an otherwise standard reaction mixture. The RAFT-agent is usually a thiocarbonylthio-compound. The polymerization is initiated by a standard radical initiator, e.g. azobisisobutyronitrile (AIBN), and the dormant species is created by reaction of two chains with the RAFT-agent (Figure 2.5).

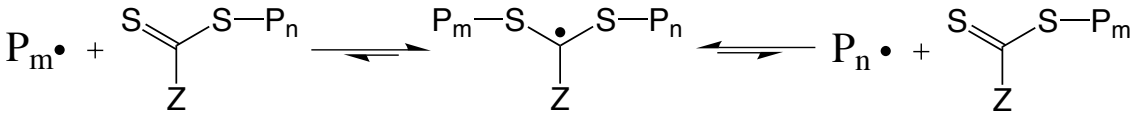

Figure 2.5: Reaction scheme of the formation of the dormant species in RAFT polymerizations.

Usually, a high excess of RAFT-agent compared to the initiator is used to ensure a high concentration of dormant species. The reaction is optimized by adjusting the reactivity of the RAFT-agent to the used monomer. This is done by introducing different side groups in the RAFT-agent.[45] Usually, a RAFT-agent can only be used for a group of similar monomers, e.g. methacrylates, with satisfactory yield. Lowering the concentration of the RAFT-agent and increasing the reaction temperature can also increase the conversion rate. However, this goes along with a broader molecular weight distribution. At the conclusion of the polymerization the RAFT-agent is attached to one of the polymer chain ends. This allows to obtain end-functionalized polymers by simply attaching the desired functional group to the RAFT-agent. One has to keep in mind that the functional group also influences the reactivity of the RAFT-agent itself. In this work a pentafluorophenol-functionalized RAFT-agent was used to obtain functionalized polystyrene (PS) and PMMA (Chapter 3) for the synthesis of polymer brushes by a "grafting-to" technique.[46, 47]

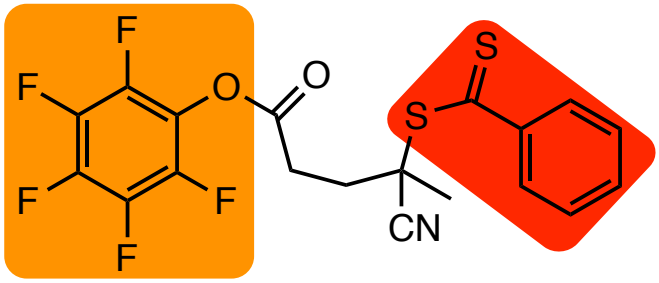

Figure 2.6: Molecular structure of the used RAFT-agent, the pentafluorogroup is shaded in orange and the thiocarbonylthio in red.

2.3.2 Atom transfer radical polymerization

In atomic transfer radical polymerization (ATRP) a transition metal based catalyst is used to generate the living character of the polymerization.[48] Unlike in the RAFT case, the polymerization is not started by usual initiators, but from a special initiator, mostly an alkyl halide. The halide reacts with the metal of the catalyst under the formation of an alkyl radical. This radical can now react with the monomer to start the growth of the polymer chain. After addition of a few monomers, the radical at the end of the polymer chain again reacts with the halide, now attached to the metal. The polymer chain is now in its dormant state. After reacting back to its reactive form, more monomers can be added until the chain is converted back into its dormant form. The main factor controlling the reactivity of the system is the used metal-based catalyst system of ligand and transition metal ion.[49]

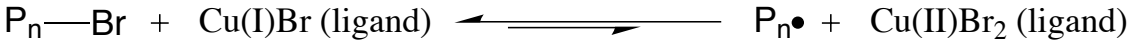

Figure 2.7: Reaction scheme of the equilibrium reaction in ATRP.

Since the polymer chain only grows at the initiator side, ATRP can be conveniently used to obtain polymer brushes via the “grafting-from” approach. Therefore, the used initiator is immobilized on the surface and afterwards the polymerization is carried out. Since the amount of initiator is very low on the surface, most

polymerizations are conducted using additional ATRP-starter in solution.[29, 50] Several studies have shown that for "grafted-from" polymer chains grown on particles the resulting polymer in solution has the same molecular weight as the one grafted on the particles.[51, 52] Whether or not this is also true for flat surfaces is an ongoing discussion. Koylu et al.[53] for example used a cleavable ATRP starter "grafted-to" a surface. After polymerization with additional free ATRP starter they compared the polymer grown in solution to the cleaved polymer brushes. With increasing conversion, they observed a higher molecular weight in the polymer brush than in the free polymer. Gorman et al.[54] investigated the "grafting-from" polymerization from different confined surfaces and found that on every surface the polymer brushes had a lower molecular weight and a higher PDI than the freely grown polymer in solution. Many other investigations can be found in the literature using different experimental methods as well as theoretical calculations.[55-57]

In summary one can say that no general consensus has been found on this matter so far. However, the studies showed that even if the found molecular weights were not similar, the obtained free unbound polymer were a good estimate of the polymer grown away from the surface.

2.4 Nanomechanical cantilever sensors

2.4.1 Theory & application

Nanomechanical cantilever sensors are miniaturized sensors mostly used for the detection of chemical and biological analytes. Typical sensor arrays (Figure 2.8) used in this work consists of 8 NMCs, similar to the ones used in scanning probe microscopy, which are attached to a supporting chip. For measurements the NMC is coated with the material of interest or an appropriate detecting layer.

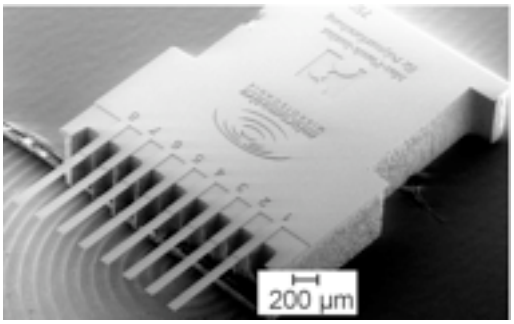

Figure 2.8: SEM image of a nanomechanical cantilever sensor array.

The NMC can be operated in two different modes, dynamic and static. In dynamic mode the cantilever is excited and the resonance frequency is determined. Changes in the coating are detected by measuring the change in resonance frequency. This allows to measure changes in mass and elastic modulus of the NMC coating. In this work only measurements in static mode were conducted. In static mode the bending of the cantilever is measured. The bending is caused by stress applied through the coated layer. Since forces from the top and bottom coating would offset each other, the NMC has to be coated only on a single side.

In general, "stress" describes the force acting within a deformable body, usually caused by external forces acting upon the body itself. A NMC can be described as a simple bar coated on side. A simple example is a NMC coated with gold, the stress is then caused by the difference in elastic moduli of the NMC and the gold. When the coating is thin compared to the bar (<5%), the resulting stress σ can be calculated using Stoney's formula:

$$\sigma = \frac{E d_c^2}{6(1-\nu)} \kappa \qquad \textbf{(7)}$$

E is the elastic modulus of the bar; d_c is the thickness of the bar, ν the Poison ratio and κ the curvature of the bar.

By using thin and flexible NMCs, as used in scanning probe microscopy (Chapter 2.6.1), stresses down to 1 mN/m can be resolved. This makes NMC a valuable tool to measure forces in nanometer thick films.

Butt et al.[21] were one of the first to use NMC bending experiments to measure changes in surface stress. By coating a gold-coated NMC with alkanethiols they

were able to measure changes in surface stress upon changing pH. Berger et al.[58] measured the change in surface stress upon the assembly of alkanethiols on top of a gold-coated NMC itself. In the past years, multiple sensors relying on bending measurements have been developed, either relying on changing curvature caused by absorption of a target molecule or by the change of the coating on top of the NMC.[59, 60] By this means, sensors for a large variety of applications have been developed[61, 62] ranging all the way from biological[63] and medical[60] to chemical[64, 65] and material science applications.

With the help of controlled radical polymerization methods (Chapter 2.3), NMCs coated with polymer brushes were obtained. By this means, changes in surface stress in homopolymer brushes upon exposure to different solvents were investigated.[66] By simultaneously preparing polymer brushes on NMC and large silicon samples, stress measurements were compared to neutron reflectivity data obtained under similar conditions. This allowed a direct correlation between the obtained stress values, measured brush thicknesses and volume fraction profiles of the brush.[23] Additionally, other stimuli-responsive brushes like Poly(N-isopropylacrylamide)[67] and polyelectrolyte brushes[68, 69] were investigated by NMCs.

Polymer brushes on top of a NMC were also obtained by "grafting-to" techniques (Chapter 2.1.3). Lenz et al.[22] used this to investigate the thermal response of surface grafted two-dimensional polystyrene/polyvinylmethylether blend films.

In the case of polymer films and, especially, polymer brushes, forces acting inside the polymer film are transduced to the NMC and result in a change in curvature (Figure 2.9).

Attractive forces, for example, result in a tensile stress bending the NMC upwards. Compulsive forces bend the NMC downwards, because of compressive stress.

The stress inside the polymer brushes is transduced into the substrate. To measure such forces, NMC sensors have become a valuable tool in recent years.[21, 70-73] By this means, surface stress changes, due to polymer brush swelling[60, 69, 74, 75], polyelectrolyte adsorption[76] and stress upon thermal treatment[22, 70-72] could be measured at extremely high resolution.

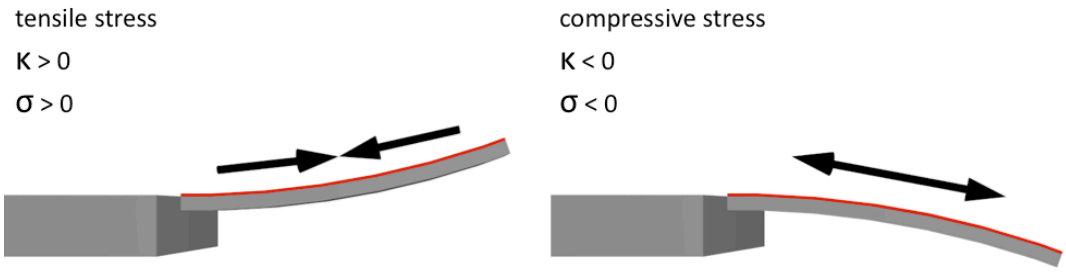

Figure 2.9: Schematic representation of cantilever bending upon forces acting inside the coating layer.

Historically, most investigations relied on measurements of the relative deflection of a NMC; using laser beam deflection methods.[77, 78] Under the assumption of constant bending along the cantilever, the change in curvature is determined.[21] However, this method has some critical limitations. Since only changes in bending are measured, no information about the initial state of the cantilever can be obtained. Absolute values of curvature remain, therefore, inaccessible. A distinction between the buildup of tensile stress and the reduction of compressive stress of the NMC-coating is not possible. Also measurements in liquid were only possible with certain limitations. Because changes in refractive index of the surrounding liquid would misalign the laser, only measurement in liquids with similar refractive indices were possible.

In recent years, different groups addressed this problem by recording 3D-topography images of single NMCs and even whole arrays. Hereby interferometry[79, 80] or laser scanning [81] techniques were applied. Both methods allow to measure complete profiles of NMC. Based on these profiles absolute values of curvature were calculated.[82]

2.4.2 Phase shifting interferometry

Interference is the phenomena of two superimposing waves forming a new wave with higher or lower amplitude. The two extreme cases are constructive and deconstructive interference, visible in the light and dark regions of a typical

interferogram. In interferometry this phenomena is used for high precision measurements of distance or refractive index.

In an interferometer, typically, a beam is split into two identical beams using a beam splitter. After following different paths the two beams are recombined creating an interference pattern. Since the beams originate from the same source, the difference in phase is only due to their different paths, e.g. path length. This allows to one obtain topographical information of an investigated surface or structure.

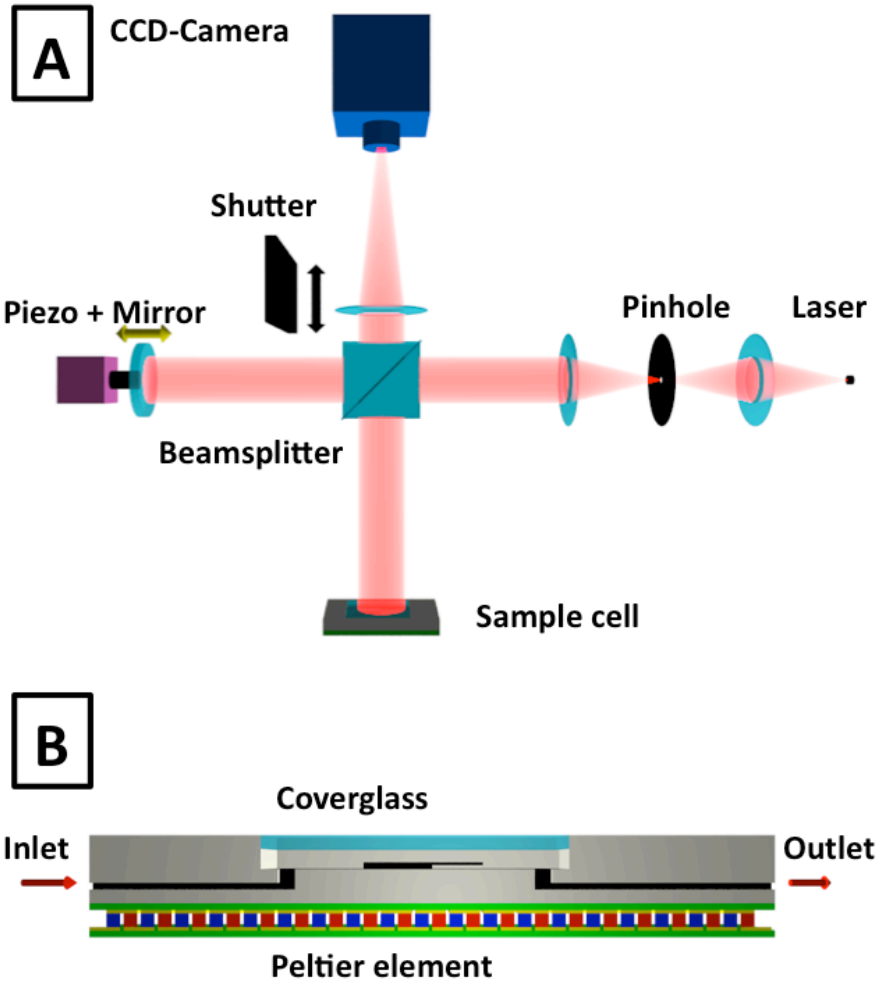

Figure 2.10: Schematic drawing of the used Twyman-Green interferometer (A) and the sample cell (B). The sample cell has a glass window for the in- and outgoing light as well as in- and outlets for gases and liquids. The temperature can be controlled by the peltier element attached to the bottom of the cell.

Phase shifting interferometry (PSI) describes a data collection and analysis method. In contrast to standard interferometry, not one but multiple interferograms are recorded and analyzed. Each interferogram is recorded at a known difference in phase between the reference and the test beam. The phase of the interfered beam can be obtained by looking at variations in the intensity pattern of the recorded image. Typically this is done by a point-by-point calculation for each recorded pixel.[83]

In this work a Twyman-Green interferometer (Figure 2.10) was assembled to obtain 3D-topography images of NMC sensors. The software for data acquisition and analysis was developed in cooperation with Roberto Raiteri and coworkers from the University of Genoa. A detailed description can be found in the following paragraph.

2.4.3 Home build setup

The built Twyman-Green interferometer was assembled from cheap of the shelf parts (Figure 2.11). For mounting and positioning of the components a LINOS microbench system (Linos Photonics GmbH & Co.KG) was used. To obtain a point-like source, the light from a laser diode (784 +/- 1 nm, 2,5 mW, RLD-78MAT4S, Laser Components GmbH) was focused onto a pinhole (0,02 mm) mounted in a spatial filter module (C30x37,5, Linos Photonics GmbH & Co.KG) using a biconvex lens (F=50; D=22,4; Linos Photonics GmbH & Co.KG). Another biconvex lens (F=50; D=22,4; Linos Photonics GmbH & Co.KG) was used to obtain a parallel laser beam. The laser beam was then split up by a cubic beam-splitter (beam splitter cubes VIS, 20x20x20; Linos Photonics GmbH & Co.KG). Part of the beam was directed on to the sample placed in a sample cell. The sample cell has a glass window for the incoming and outgoing laser beam as well as gas in- and outlets. The temperature (T=10-150±0,1°C) was controlled by a peltier element attached to the bottom of the cell (Figure 2.10/Figure 2.11). The sample cell was mounted on an adjustable holder (adjust.x. m, Linos GmbH), attached to a rail system. The other part of the beam passed through a shutter and was reflected by a mirror (Ø =25,4;

d=5;L/10;RAGV; Linos Photonics GmbH & Co.KG) mounted onto a piezo-actuator (PAZ 020, Thorlabs Inc.). The piezo-actuator was connected to a closed-loop controller (BPC201, Thorlabs Inc.), which allows adjusting the position of the mirror at an accuracy of 5 nm. The piezo-actuator was mounted on an adjustable stage (adjust.x s, Linos GmbH), fixed to a rail system. Both reflected beams passed through the beam splitter and were then focused on a CCD-camera (Marlin F-046B; resolution = 780x582, pixel size = 8,3µm x 8,3µm; 53fps; Allied Vision Technologies GmbH) using a biconvex lens (F=50; D=22,4; Linos Photonics GmbH & Co.KG). For alignment, the shutter was closed so that only light coming from the sample reaches the CCD-camera. This allowed to focus the laser light on the cantilever by adjusting its height and also to remove any tilt. The shutter was then opened; piezo and mirror were tilted and moved in the laser beam direction to obtain the desired interference pattern (Figure 2.12). To reduce noise, the setup was placed in an acoustic-isolation box, placed on a vibration-isolated table.

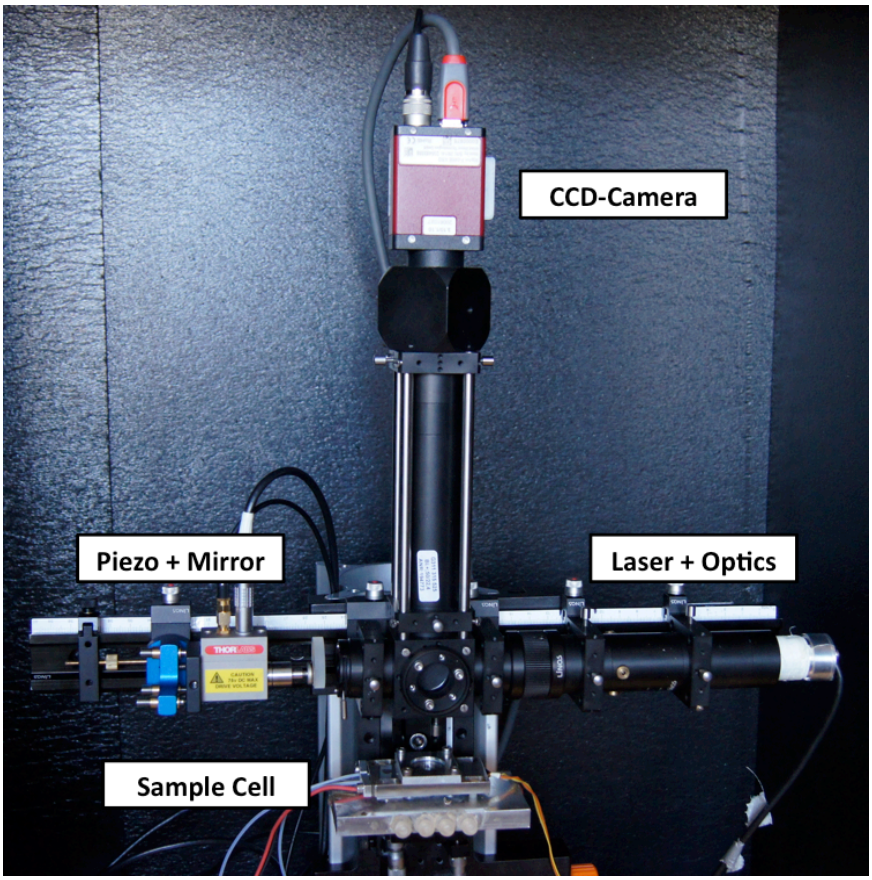

Figure 2.11: Image of the home-built Twyman-Green interferometer.

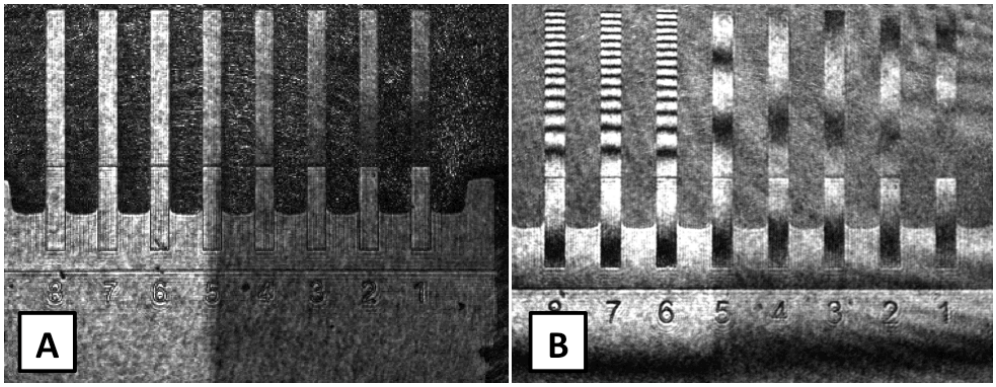

Figure 2.12: CCD-camera image of the focused NMC array (A) and with interference fringes (B).

2.4.4 Data acquisition and analysis

For data acquisition and analysis, software was developed using LabVIEW 8.5 (National Instruments). The software allows the user to conveniently select each NMC as well as part of the chip as area of interest. Line profiles can either be drawn by hand or are integrated automatically. For curvature measurement of NMCs, usually, multiple profiles are placed automatically along the long axis of the cantilever. To obtain a 3D-topography image of the NMC, multiple images are recorded at different mirror positions. Multiple algorithms to reconstruct the phase are implemented. The algorithms vary in the number of needed images and, therefore, differ in measurement speed as well as precision. The algorithms are the three-step technique, the four-step technique, the Carré technique and the Hariharan five-step technique.[84, 85] The maximum measuring frequencies are 1,42 Hz, 1,08 Hz, 1,04 Hz and 0,87 Hz respectively. As a degree of precision the root mean square difference of two images of the same region is evaluated. The average root mean square of 200 measurements performed on uncoated areas of the chip resulted in values of 3,175, 1,945, 2,187 and 2,012 respectively.[86] All values are below the threshold for a well-calibrated system of $1/100\lambda = 7{,}85$.[87]

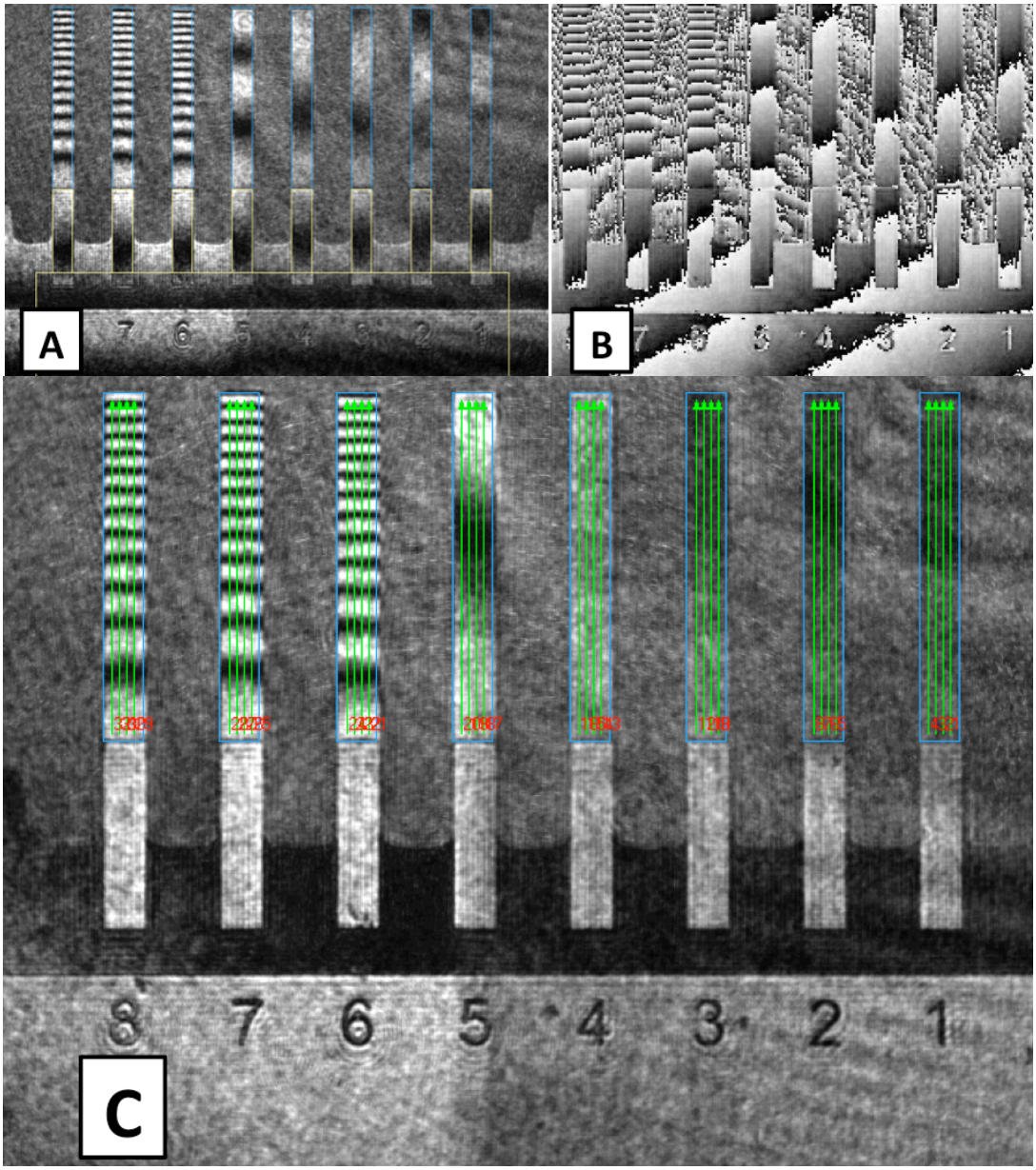

Figure 2.13: NMC image with selected area of interest (A) and obtained wrapped phase image (B). Automatically selected line profiles on top of the cantilevers (C).

The so obtained phase information is only in a range of 0 to 2π causing jumps between adjacent pixels. To remove these jumps, phase unwrapping is performed (Figure 2.14). Basically, a multiple of 2π is added or subtracted whenever the difference between two pixels is greater than π. To perform the required phase unwrapping, two different methods can be used. The first being a guided path following algorithm[88] for low noise phase maps, and the second a two dimensional, quality guided, non continuous-path following algorithm[89] suitable for high noise

phase maps. Since the unwrapping is a time consuming step, it can be limited to the selected line profiles. From the obtained unwrapped phase image the topography image H(x,y) can be calculated using the following formula,

$$H(x,y) = \frac{\lambda}{4\pi}\varphi(x,y) \tag{8}$$

with λ being the wavelength of illumination and φ the phase. The selected line profiles can be simultaneously analyzed and averaged out to obtain an averaged profile of each cantilever. The profile can be fitted with a linear, cubic, circle or parabolic function. The fit can either be performed along the whole length of the NMC or in segments to obtain local information. To extract local curvature values κ, the area of interest is fitted with a parabolic function.

$$z(x) = a_0 + a_1 x + \frac{\kappa}{2}x^2 \tag{9}$$

$$\kappa = \frac{d^2 z(x)}{dx^2} \tag{10}$$

$$\Delta\kappa = \kappa_2 - \kappa_1 \tag{11}$$

As an example, the profiles from 750 µm long NMCs consisted of 230 data points with a pitch of 3,2 µm. Multiple measurements at room temperature yielded a standard deviation of $\Delta\kappa = 2{,}6\times10^{-9}\mu m^{-1}$.

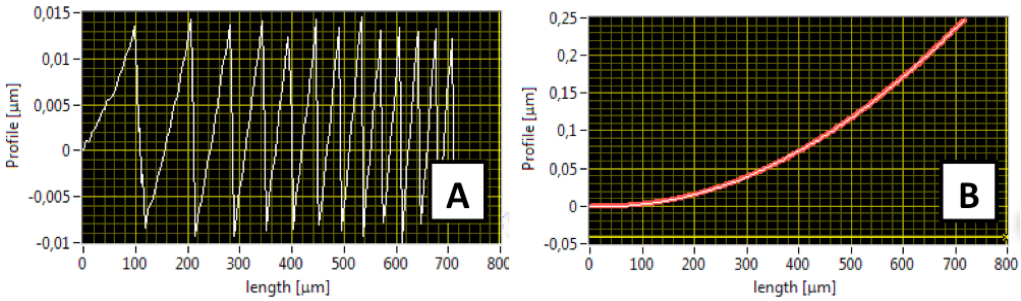

Figure 2.14: Obtained averaged line profile before unwrapping (A) and after unwrapping with parabolic fit along the complete length of the cantilever (B).

All analysis can be done during the experiment or after the completion of the experiment in a separate offline mode. Thereby, the topography of the NMC can be followed during the measurements while still being able to modify the analysis after the completion of the experiment.

2.4.5 Nanomechanical cantilever coating

To allow comparable studies of different systems, and to account for unwanted effects, NMC arrays carrying multiple cantilevers are utilized. By using uncoated NMCs as reference, the obtained data could be corrected for bending caused by unwanted effects. This demands for an individual coating of single NMCs of an array.

To obtain a constant radius of curvature along the whole length of the NMC, a homogenous single sided coating on the NMC is necessary. The preparation of such coatings on NMCs is a difficult task. The small sample geometry as well as the requirement for the NMC to be only coated on one side, are two facts that complicate the task at hand. The fragile nature of the NMCs, and the fact that single NMCs have to be coated individually, makes it even harder. To assure single sided and/or partial coatings, the use of a protecting layer has proven to be a reliable option.[66] Therefore, a thin gold layer is applied to the back of the cantilever array before the coating process, and is removed again after the coating has been applied. The biggest disadvantage of this method is that the gold is removed by KI/I_2 in aqueous solution and the coating, therefore, must not be soluble in water.

For the coating itself, microcapillaries, microfluidic networks and plotting techniques[90, 91] have been utilized. The coffee stain effect[92] and heterogeneities in wetting of the polymer solution complicate the coating. To circumvent such problems, the NMC surface can be pre-functionalized using self-assembled monolayers.[91] Recently, Liu et al.[93] obtained a homogenous polymer coating by transferring a self-assembled monolayer of polymer colloids from an air/water interface on a NMC. By consequently heating the precursor film above the T_g, the colloids melt and form a homogenous polymer film.

In comparison to that, coating of the NMC with polymer brushes has several advantages. Since polymers are bound to the NMC, they can be exposed to solvent without being washed off. In a “grafting-to” approach heterogeneities in the precursor coatings are negligible since the majority of the polymer is washed of after fixation of the chains.
In this work the inkjet plotting technique has been utilized to prepare "grafted-to" polymer brushes on individual NMCs. The preparation of "grafted-from" polymer brushes on top of NMCs could only be done in solution. To obtain uncoated NMCs a protective gold layer has to be applied to the back and also to a couple of NMCs on the top.[23, 66, 74]

2.4.6 Inkjet-printing

To individually and partially coat the cantilever with the polymer brushes, a device is needed to deposit small amount of the precursor polymer solution with micrometer precision.[22] To do so, the Nano-plotter NP 2.1 (GeSIM, Grossmerkmannsdorf, Germany) was used. For printing, the plotter (Figure 2.15) relays on the principle of ejecting liquid through a small nozzle, as commonly used in office printers. The pulse required for the ejection of the liquid is generated using a piezo crystal attached to the nozzle. In this work so called *Nanotips* were used producing drop volumes of 0,4 nl. The printed solutions are provided in a microtiter plate allowing the deposition of multiple solutions in a single step. The deposition process is controlled by the software “NPC16”. By applying the software SpotFrontEnd©, printing procedures were obtained including spotting patterns, washing, drying and control steps by stroboscope camera. This enables one to dispense multiple polymer solutions with high accuracy and reproducibility.

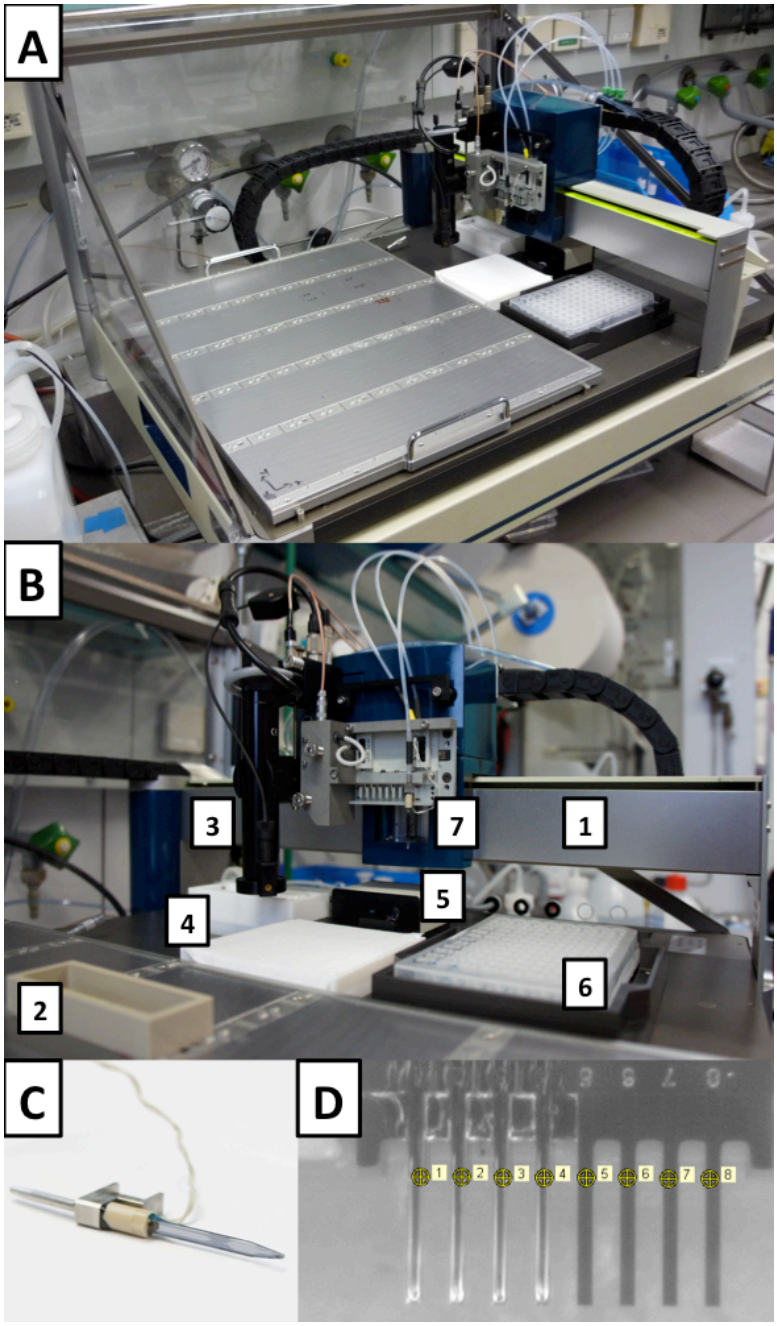

Figure 2.15: Image of the Nanoplotter (A) used for NMC coating. Close-up image showing the positioning system (B1), the NMC holder (B2), the camera for positioning (B3), the washing and drying stations (B4), the stroboscopic camera (B5), the microtiter plate (B6) and the nozzle (B7). Image of the used Nanotyp (C) and image (D) taken by the positioning camera of a NMC array right after deposition of polymer solution.

2.5 X-ray scattering

2.5.1 X-ray reflectivity

When a monochromatic incident beam hits onto a sample surface under a certain incident angle α_i, the beam is reflected and scattered at the sample surface. The exiting beam can be described by the exit angle α_f perpendicular to the surface, and the angle Θ parallel to the surface. The wavevector transfer, $q = k_f - k_i$ where k_i and k_f are the incoming and outgoing wavevectors, can be described by its single x, y and z components.

$$q = \begin{pmatrix} q_x \\ q_y \\ q_z \end{pmatrix} = \frac{2\pi}{\lambda} \begin{pmatrix} \cos(\alpha_f)\cos(2\Theta) - \cos(\alpha_i) \\ \cos(\alpha_i)\sin(2\Theta) \\ \sin(\alpha_i) + \sin(\alpha_f) \end{pmatrix} \quad \textbf{(12)}$$

In a X-ray reflectivity (XRR) experiment the sample is investigated by steadily increasing the incident angle α_i. To obtain the desired reflectivity curve, the intensity of the reflected beam is constantly measured at $\alpha_f = \alpha_i$ and $\Theta = 0$. The wavevector transfer, therefore, has only a z-component, $q_z = (4\pi/\lambda) \sin \alpha_i$. Since q_z is perpendicular to the surface, the XRR measurement only yields information perpendicular to the surface. In a typical XRR experiment the angle is increased from 0,1-5°, and the reflected intensity is measured and normalized to the incoming intensity. In the case of X-rays, the beam comes from an optical thinner medium (air) to the optical thicker medium. Up to the material dependent critical α_c the incoming beam is completely reflected. The resulting reflectivity is, therefore, steady and equal to 1. At angles above α_c part of the beam is refracted at the surface. The resulting angle α_t can be expressed by Snell's law

$$n_0 \cos(\alpha_i) = n_1 \cos(\alpha_t) \quad \textbf{(13)}$$

with n being the refractive indices of the respective layers (Figure 2.16). For X-ray the refractive index can be described as follows.

$$n = 1 - \delta_{ref} - i\beta_{ref} \quad \textbf{(14)}$$

The real part δ_{ref} describes the scattering of the X-ray beam at the electrons of the atoms. The imaginary part $i\beta$ describes the absorption of the X-rays

$$\delta_{ref} = \frac{\lambda^2 \rho_{el} r_0}{2\pi} \quad \textbf{(15)}$$

$$\beta_{ref} = \frac{\lambda \mu_{abs}}{4\pi} \quad \textbf{(16)}$$

with ρ_{el} being the electron density, r_0 the electron radius and μ_{abs} the mass absorption coefficient. For X-ray wavelengths used in this work, δ_{ref} values are typically in the order of 10^{-6}-10^{-5} and the μ_{abs} values are even lower in the order 10^{-7}-10^{-8}. The resulting refractive indices are smaller and close to 1.

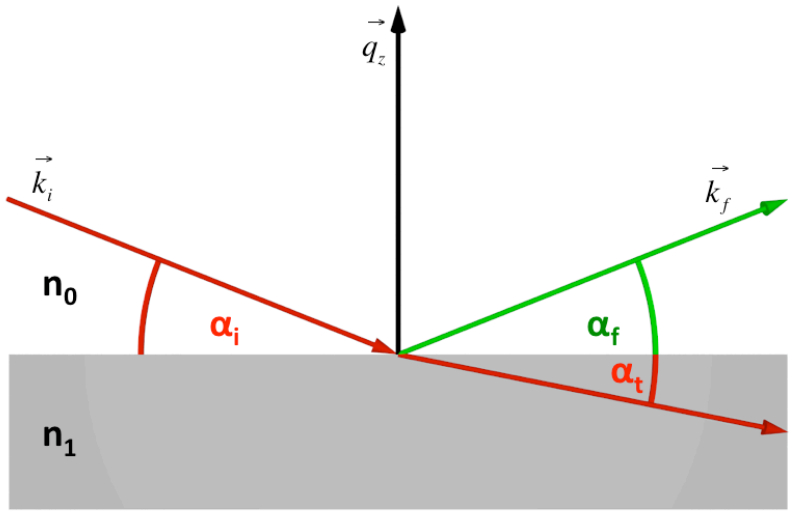

Figure 2.16: XRR scattering geometry, the incoming and outgoing angles are exaggerated for better illustration.

The refractive index of air is 1, and α_t is equal to 0. For small incidence angle one can estimate the critical angle to be

$$\alpha_c \approx \sqrt{2\delta_{ref}} \tag{17}$$

The critical angle is, therefore, only dependent on the electron density of the medium. For incident angles above the critical angle ($\alpha_i > \alpha_c$), the reflected amplitude can be expressed by the single wavevectors

$$r = \frac{k_{z0} - k_{z1}}{k_{z0} + k_{z1}} \tag{18}$$

The Fresnel reflectivity is expressed by

$$\overline{R} = r \times r^* = \left| \frac{k_{z0} - k_{z1}}{k_{z0} + k_{z1}} \right|^2 \tag{19}$$

If not a bare surface, but a thin film on top of a surface is investigated, the incoming beam is reflected and refracted at the air/film as well as the film/substrate interface (Figure 2.17).

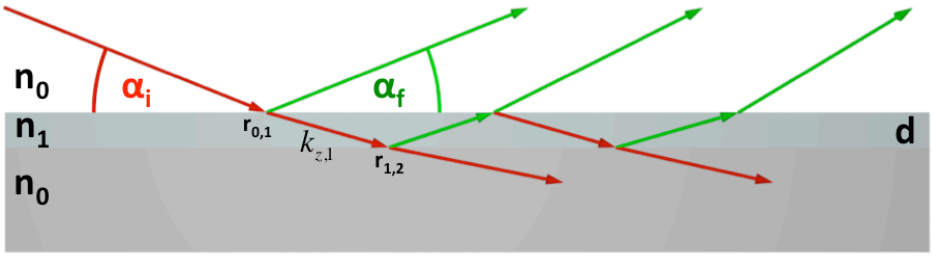

Figure 2.17: Schematic representation of the X-ray beam path for a one layer system in a XRR experiment.

The reflected intensity is then given by

$$\overline{R_F} = \left| \frac{r_{0,1} + r_{1,2} \exp(2ik_{z1}d)}{1 + r_{0,1}r_{1,2} \exp(2ik_{z1}d)} \right|^2 \tag{20}$$

Figure 2.18 displays a calculated reflectivity curve for a 20 nm thick polystyrene film on top of a silicon substrate. The oscillations in the curve are caused by the destructive and constructive interference of the reflected X-rays. From the distance between the minima or maxima of the oscillation, the thickness of the film can be calculated.

$$d = \frac{2\pi}{\Delta q_z} \tag{21}$$

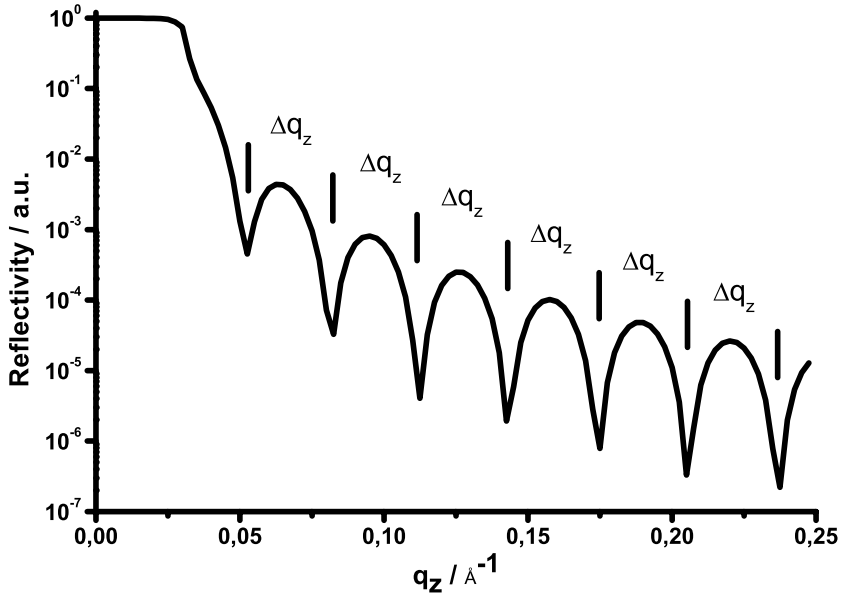

Figure 2.18: Simulated XRR curve of a perfectly flat 20 nm thick polystyrene film on a perfectly flat silicon substrate.

So far all equations have been derived under the assumption of perfectly flat surfaces and interfaces, but in reality all interfaces/surfaces have statistical height variations, they are rough. When the radius of a rough structure is larger than the coherence length of the probing beam, one speaks of *waviness*. If the structure is smaller, it is called micro-structured roughness. In general, both types of roughness lead to a local deviation of the angle of incidence α_i from the average value. In general, this will cause an overall reduction of the recorded intensity. Additionally, the amplitude of the oscillations will be damped, because of the reduced interference caused by the shift in phase between the two interfaces (Figure 2.19). One approach to account for local height deviations from the average value is by Gaussian statistics.

$$G(z) = \frac{1}{\sqrt{2\pi}\sigma_{av}} \exp\left(\frac{-z^2}{2\sigma_{av}^2}\right) \quad \textbf{(22)}$$

With σ_{av} being the standard deviation of the interface from the average value. When roughness is considered the overall reflectivity can be expressed as

$$\overline{R} = \overline{R}_F \exp(-4k_z^2\sigma_{av}^2) \quad \textbf{(23)}$$

From the equation one can conclude that XRR measurements become more sensitive to roughness with increasing α_i.[94, 95]

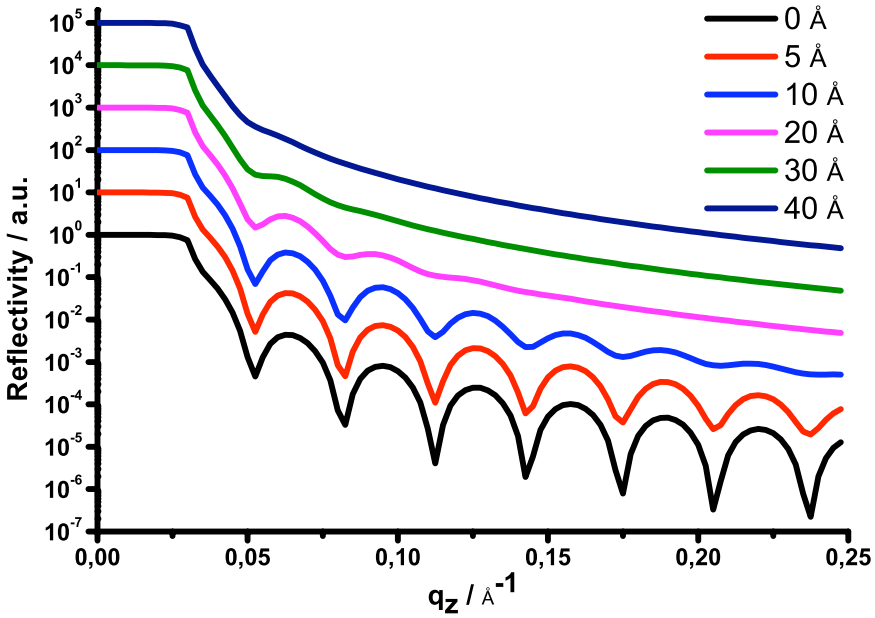

Figure 2.19: Simulated XRR curves of a 20 nm thick PS film with different PS/air interface roughness on a silicon substrate with 0 Å PS/silicon interface roughness. The curves are shifted for better visibility.

2.5.2 2D-X-ray reflectivity

In this work performing XRR measurements on a defined µm-large area were desirable for the investigation of NMCs (Chapter 6) as well as the determination of the film thickness in order to investigate correlated roughness (Chapter 7). To do

so, the measurements were conducted at the BW4 beamline using a µ-focused X-ray beam. At the beamline no XRR option is implemented, therefore the 2D-detector had to be utilized to perform XRR measurements. Lenz et al. did this by recording more than 100 2D-detector images at different angles of incidence. For each image the intensity at the corresponding α_f pixel position was determined and normalized to the incoming intensity. By this means, a complete XRR curve could be recorded.[22] Although functional, the method has one major disadvantage, its long measurement time (≈ 2 hours). This is mainly caused by the amount of required images and the slow readout of the detector.

In this work a method developed by Frömsdorf et al. was utilized. The sample is aligned and the angle of incidence is set $\alpha_i = 0°$. The beam shutter is opened and the angle of incidence is uniformly increased to higher incidence angles. The beam shutter is closed and the 2D image is read out. The obtained 2D image (Figure 2.20) shows the trail of the intensity at $\alpha_i = \alpha_f$. To analyze the data, a cut is performed in the q_z direction; several pixels are summed up in the vertical direction and normalized to the maximum intensity to obtain a reflectivity curve.

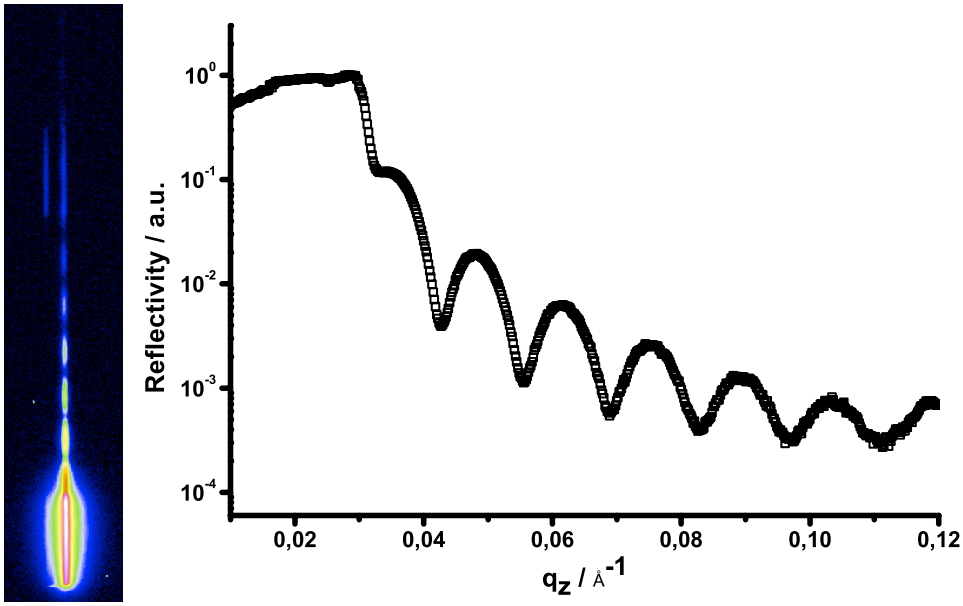

Figure 2.20: 2D-detector image obtained from 2D-XRR measurement with corresponding XRR curve.

The main advantage of this technique compared to the method by Lenz et al. is the reduction in measurement time. Due to the high incoming intensity a measurement can be performed in 30 s. This allows to largely increase the amount of samples measured in a given time. Considering the fact that beamtime at high flux sources is always limited, this reduction in measurement time is a crucial factor. One disadvantage of the method is the counting rate limitation of the used detector. The available 2D-detector has a maximum counting rate of 70000 counts/pixel and a readout noise of 10 counts/pixel. Because of this only three orders of magnitude in the reflectivity can be probed in a single measurement. This can be compensated by dividing a single measurement in multiple measurements ranging from different regions in incident angle and varying the incoming intensity. Since the hexapod used for measurement did not allow varying movement speeds, only a single measurement with maximum incoming intensity was performed. The measurements were performed from angles of α_i 0-2,5°. This resulted in XRR curves in a q_z-range from 0-0,12 $Å^{-1}$. Measurements performed with the 2D-goniomter stage were divided in 3 parts with intervals from 0,1-1,6°, 0,4-1,8° and 0,6-2° with varying incoming intensity. This resulted in XRR curves with a q_z-range from 0-0,24 $Å^{-1}$.
Another disadvantage is that the diffuse scattered intensity at $\alpha_f \neq \alpha_i$ is also recorded. This is especially problematic when only one measurement is performed. Fitting the measured data is, therefore, not possible. The film thickness can still be calculated from the width of the oscillation, which is not altered from the background or by comparison with simulated XRR curves. Roughness and electron density profiles, however, are not accessible.

2.5.3 Data evaluation

The X-ray reflectivity data was fitted with the parratt formalism[96] using the software Parratt32©. The starting values of the scattering length densities (Appendix 1) were determined using the Scattering Length Density Calculator

supplied by the NIST Center for Neutron Research.[97] If no fit could be performed, the film thickness was calculated from the differences of the oscillation minima.

2.5.4 Grazing incidence small angle X-ray scattering

In a gracing incidence small angle X-ray scattering (GISAXS) experiment, a X-ray beam is directed onto a sample at a small angle of incidence α_i. The resulting scattered intensity is recorded with a 2D-detector. In contrast to XRR where the sample is only probed in the horizontal direction, this allows one to probe the surface in the horizontal as well as the lateral direction. Information about the structure of the film in the horizontal direction can be obtained by analyzing the 2D-image in $q_\perp = \sqrt{q_z^2 + q_x^2}$ direction. In the lateral direction the 2D-image is analyzed in $q_{||} = \sqrt{q_x^2 + q_y^2}$. For small α_i and α_f, $q_\perp$ and $q_{||}$ can be approximated as q_z and q_y since $q_x << q_z, q_y$.

A typical 2D-GISAXS image has three distinct features, first, the direct beam which is only refracted at the sample surface, and second the so-called, *specular peak* at $\alpha_f = \alpha_i$. Due to their high intensity both signals are usually blocked by a beam stop to avoid damage to the detector. The third feature is the yoneda peak at $\alpha_f = \alpha_c$. Since the majorities of the incoming photons either pass through the sample or are reflected to the specular position, the remaining diffusely scattered intensity is very low. In addition to that, the diffusely scattered intensity is distributed over a relative large area. Because of this, high flux radiation sources are needed to perform such measurements.

To analyze the 2D-image for horizontal information, an intensity profile in the q_z-direction is obtained by summation of several pixels along the q_z-direction of the image. For lateral information the same procedure is done in the q_y-direction at the yoneda maximum (Figure 2.21).

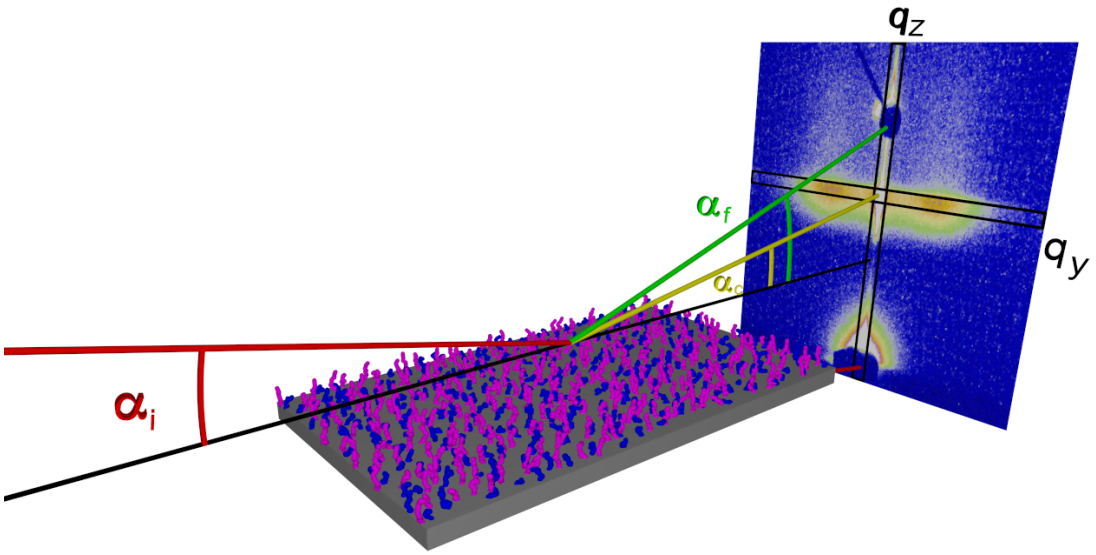

Figure 2.21: GISAXS geometry.

As visible in XRR curves, the angle of incidence has a large impact on the amount of X-rays reflected at the surface and underlying interfaces. At small angles of incidence below the critical angle of the sample, the beam does not penetrate the surface. The obtained GISAXS data are, therefore, only from the surface structure. If the angle of incidence is increased to an angle equal or slightly above the critical angle, data from the surface as well as the films internal structure are probed by the GISAXS experiment. At angles larger than the critical angle, the GISAXS experiment mainly yield information about the internal structure of the film.

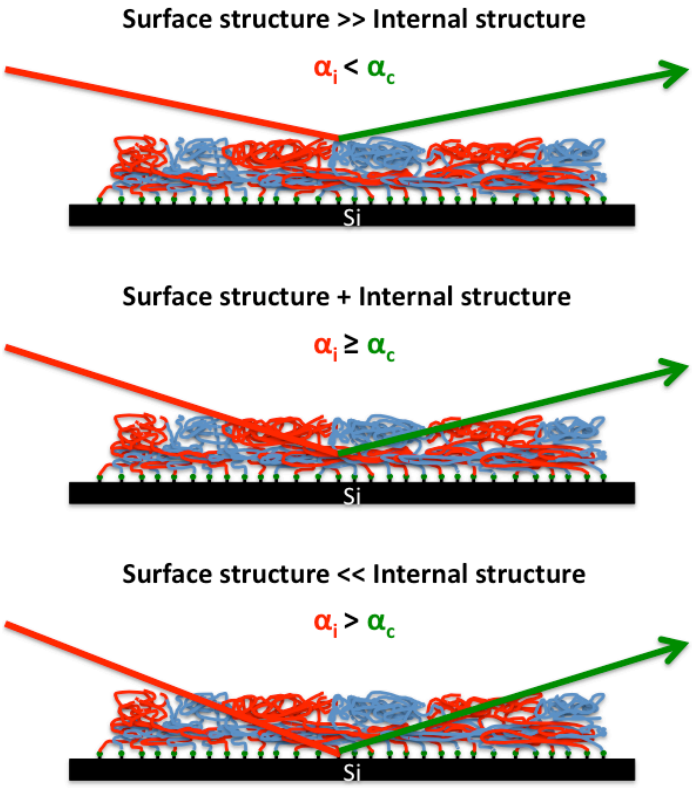

Figure 2.22: Schematic representation of the angle dependence on the penetration depth in GISAXS experiments.

The obtained scattering data contains averaged information of structures in the nanometer size range. Typically, an area around 1 mm^2 is investigated depending on the angle of incidence and the size of the beam.

2.5.5 Lateral data evaluation

The lateral intensity profiles were analyzed using a global scattering function. This global model describes scattering from specimen in terms of multiple structural levels by combining exponential laws, power laws and Bragg based interference functions. The scattering objects are described by their radius of gyration, mean centre-to-centre distance, and their fractal dimension. Lenz et al.[98] demonstrated that this data analysis, usually used in SAXS data analysis, is also applicable for GISAXS for the analysis of polydisperse samples like polymer films.

$$I(q) \approx \sum_{i=1}^{n} G_i \exp\left(-\frac{q^2 R_{gi}^2}{3}\right) + B_i \left(\frac{-q^2 R_{g(i-1)}^2}{3}\right) \left[\frac{\left(erf\left(qR_g/\sqrt{6}\right)\right)^3}{q}\right]^P \quad \textbf{(24)}$$

The first term describes the size of a spherical averaged particle (R_g) and the second term corresponds to the Porod regime. The exponent P gives rise to the geometry of the scattering object. Perfect spherical particles would result in a P = 4 while cylindrical particle would yield P = 3.
To account for the interference between the scattering objects, an interference function is introduced.

$$I_{corr}(q) = I(q)S(q) \quad \textbf{(25)}$$

The interference function S(q) describes the correlation with help of a radius of correlation ξ and a packing factor K.

$$S(q) = \frac{1}{1 + KF(q,\xi)} \quad \textbf{(26)}$$

with F(q, ξ) being the "form factor" for structural correlations.

$$F(q,\xi) = 3\frac{\sin(q\xi) - q\xi\cos(q\xi)}{(q\xi)^3} \quad \textbf{(27)}$$

The data analysis was done using the free available software Irena[99] for Igor Pro, Wavemetrics Inc.

2.5.6 Roughness correlation

Roughness correlation describes the complete or partial transfer of a roughness profile from an interface to the overlying interface. The phenomena can be figuratively compared to a field covered with snow. When the field is only covered with a little bit of snow, the profile of the underlying field can still be identified. Depending on the amount of snow, the transferred interface is smoothed; only

larger surface characteristics are visible at the surface. The two interfaces are, therefore, specified as partially correlated. If more snow covers the field, the surface becomes flat and no characteristic of the underlying surface is visible. Hence the two interfaces field/snow and snow/air are uncorrelated (Figure 2.23).
The effect was first observed in thin liquid films. The roughness correlation was attributed to van der Waals interactions of the small molecules with the underlying substrate suppressing thermally stimulated capillary waves.[100] The discovery of the giant magneto resistance[101], nowadays used in hard disk drives, sparked a huge interest in multilayer thin films. Interfacial and correlated roughness plays a role in these kinds of systems and was investigated in this regard.[102, 103] Specular and off-specular X-ray scattering were the dominant methods of choice.[104, 105] Studies from Gibaud et al[106] showed that, due to the interdependence of the interfaces, the standard models used for X-ray reflectivity data evaluation (Chapter 2.5.1) are not applicable to fit the scattering data. Only the layer distance can be obtained using the distance between oscillation minima.

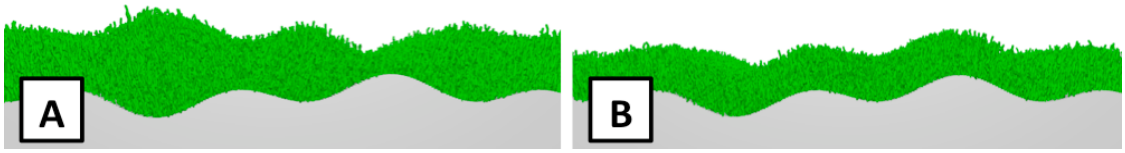

Figure 2.23: Schematic representation of an uncorrelated (A) and a partial correlated (B) polymer brush film.

When the roughness profiles of the two interfaces of a single layer system are independent of each other, the diffuse scatterings are also independent of each other. The resulting intensity is, therefore, uniformly spread across the reciprocal space. When the roughness profile of one of the interfaces is partially replicated to the other interface, the diffuse scattering of the interfaces is partial in phase coherence. Due to the partial replication the resulting Bragg points are spread into diffuse sheets of intensity in the q_x-direction (Figure 2.24).

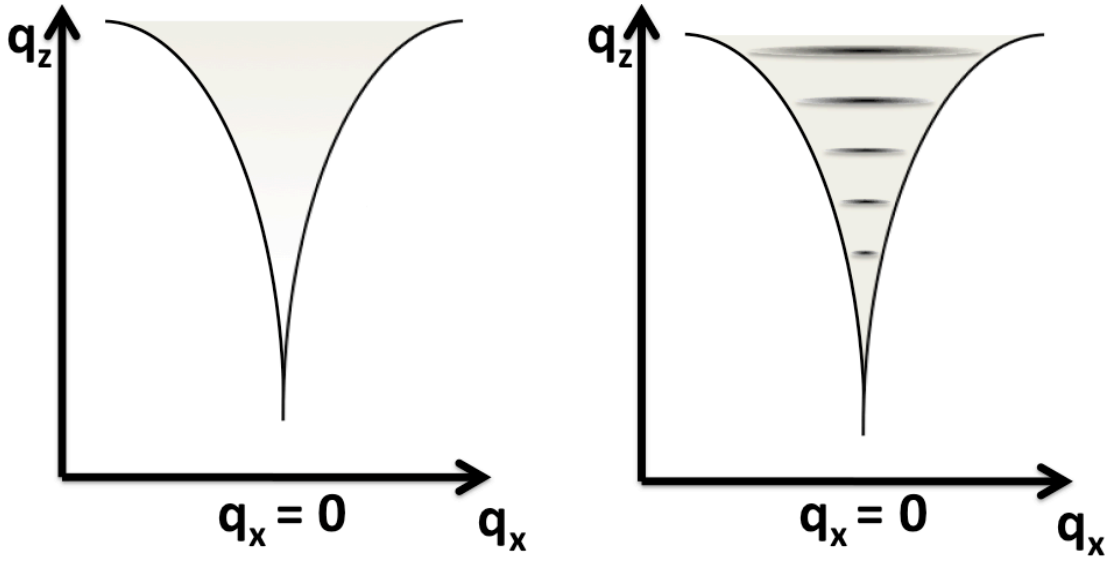

Figure 2.24: Schematic q_z vs. q_x intensity plot for an uncorrelated and correlated film.

Experimentally roughness correlation is investigated by performing rocking scans or by analyzing the reflected intensity in the q_z-direction using a 2D-detector.

2.5.7 Setups

The X-ray reflectivity measurements were conducted using a XTD 3003 TT, Seifert, Rudolfstadt, Germany diffraction system. As X-ray source a Cu-anode ($\lambda_{Cu\text{-}K\alpha}$ = 1,5486 Å) was used with a beam size of 1000 x 100 µm² (horizontal x vertical).
The 2D-XRR and GISAXS measurements were performed at the BW4 beamline, HASYLAB, DESY, Germany (Figure 2.25). With the help of the micro-focus option, a beam size of 32x17 µm² (horizontal x vertical) were obtained, small enough to address single NMCs.[107-109] The incoming beam intensity can be altered using a motor driven filter wheel with eight circular holes. The holes are equipped with aluminum foils of different thicknesses allowing the primary beam to be attenuated from 60 to 1 % intensity. The sample is placed on a two-circle goniometer with an x/y/z translation stage. For simultaneous investigation of a NMC by µ-focused X-rays and PSI (Chapter 6) the samples are placed on a hexapod

M-824 (Physik Instrumente (PI) GmbH & Co. KG, Karlsruhe, Germany). The hexapod was placed on an additional z-stage for height adjustment.

The signal was recorded using a marCCD 165-detector, which has an active area diameter of 165 mm, with 2048x2048 pixels having a size of 79,1 x 79,1 μm^2. The detector has a readout time of 3,5 s and a readout noise of 10 counts/pixel. The sample detector distance was around 2 m.

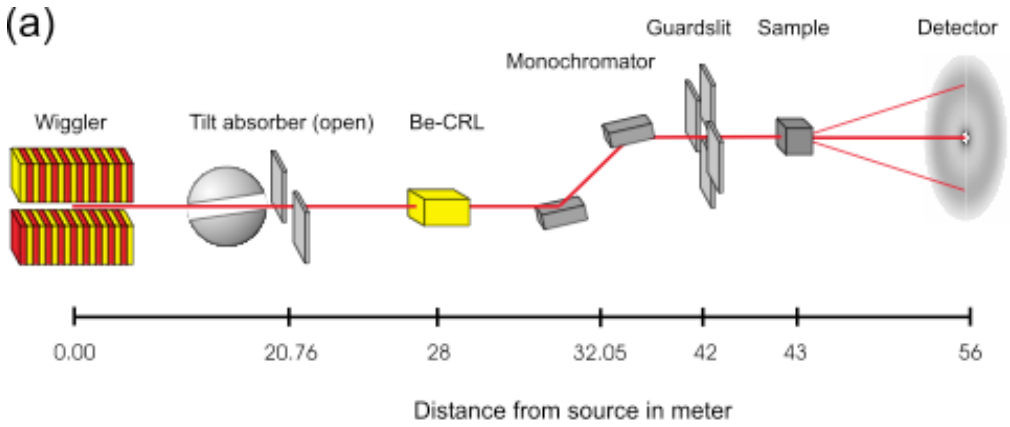

Figure 2.25: Layout of the beamline BW4 at HASYLAB, DESY. [107]

2.6 Miscellaneous experimental techniques

2.6.1 Scanning probe microscopy

Scanning probe microscopy (SPM) is a method to obtain information of surfaces in the nanometer range. Therefore, a tip is attached to a cantilever and scanned across the surface. For the investigation of hard surfaces the type is in the so-called *contact-mode* and in permanent contact with the surface. Polymer surfaces can not probed like this. The tip would simply stick to the surface. Because of this the *tapping mode* is used. The cantilever is, therefore, excited close to its resonance frequency and scanned across the surface. The amplitude of the cantilever is damped by interaction of the tip with the surface, e.g. van der Waals forces. A feedback loop system maintains a constant amplitude by adjusting the height of the sample. From the required adjustment in height at each sample position a topography image is obtained. From the differences in phase the so-called *phase image* is created supplying information on elastic properties of the surface.[110]
Scanning probe microscopy images were obtained in tapping mode using an Dimension 3100 scanning probe microscope, Veeco Instruments GmbH. OMCL AC 160 TS, Olympus, Japan cantilevers were used with a resonance frequency of approx. 300 kHz and a spring constant of 42 N/m as specified by the manufacturer.

2.6.2 Gel permeation chromatography

Gel permeation chromatography (GPC) is a relative method to determine the molecular weight and polydispersity of polymer samples. Therefore, a polymer sample is applied to a column containing porous beads. The retention time of each polymer chain depends on its hydrodynamic volume, while the smaller polymer chains are eluted later compared to bigger polymer chains. By comparing the elution time to known samples the molecular weight as well as the polydispersity can be determined.[44]

GPC measurements were performed by the polymer analytic service group at the Max Planck Institute for Polymer Research using the following setup:
Pump: Waters 515 HPLC Pump; Autosampler: Waters WSIP 717; Columns: 3 Polymer standard service columns (SDV) in series, dimension 8x300 nm, porosity 500, 10^5, 10^6 Å filled with poly(styrene/divinyl benzene); Detector: RI ERMA Inc. 7512 ERC, eluent: Toluene, Tetrahydrofuran (flowrate 1 ml/min); Standards: low-polydispersity poly(methyl methacrylate), Operating Temperature: room temperature

2.6.3 Nuclear magnetic resonance

Nuclear magnetic resonance (NMR) spectroscopy is a method to determine the chemical structure of molecules. To do so, the investigated sample is placed in a strong magnetic field. NMR-active nuclei (e.g. ^{1}H) align either parallel or antiparallel to the external field possessing two energy levels with a difference depending on the local magnetic field. From the difference in the resulting resonance frequency the chemical environment can be determined.[44]
NMR measurements were performed using an Avance DPX 250, Bruker, 250 MHz. All samples were measured in deuterated chloroform as solvent. The obtained spectra were calibrated using the solvent as reference and analyzed with the software MestReC.

2.6.4 Contact angle measurement

The measurement of a contact angle is a method to determine the surface tension of a given surface. To do so, a liquid drop is placed on the surface and imaged by a video system. In equilibrium the contact angle at the liquid/vapor/solid interface is specific for any given system. If the liquid and vapor phase is kept constant, changes in contact angle allow conclusion about the change in surface tension of

the solid interface. Comparison with literature values also allows conclusion about the composition of the investigated interface.[111]
Contact angle measurements were conducted on a Krüss, DSA10-MK2. The static contact angle was measured in air under ambient conditions using MilliQ water.

2.6.5 Near edge X-ray absorption fine structure

Near edge X-ray absorption fine structure (NEXAFS) is a surface sensitive method to determine elements and their bonding environment. For the investigation of polymer films, the samples are irradiated with soft X-rays. Photoabsorption and photoelectron emission result in electron holes near the core, subsequently the holes are filled by dropping down of higher-level electron accompanied by emission of a fluorescence photon or auger electron. Due to the low energy of the photons, multiple scattering events occur at neighboring atoms yielding information of the bonding environment.
To record a spectrum the total electron yield is measured as a function of irradiated X-ray energy. Since electrons created deep within the sample loose to much energy to overcome the samples work function, they do not contribute to the total energy yield. Therefore only depths of a few nanometer contribute to the measurement.[112, 113]
The measurements were performed at the BEAR beamline at ELETTRA, Trieste, Italy.[114] The spectra were recorded by measuring the neutralization current of the grounded sample during X-ray irradiation. The incident angle was set to α_i = 30° and the energy was scanned from 270 to 380 eV with an energy resolution of 0,5 eV. The raw data is corrected for background, normalized by the synchrotron ring current and corrected for the beamline spectrum.

2.7 Wafer cleaning procedure

If not stated all silicon wafers were cleaned using the following procedure. The wafers were put in dichloromethane, placed in an ultrasonic bath for 15 min and dried with a stream of nitrogen. Consequently the wafers were immersed in a solution of ammonia, hydrogen peroxide and distilled water (1:1:5 vol./vol.) and heated to 70°C for 20 min. The wafers were then rinsed with distilled water and dried with a stream of nitrogen. The wafers were either used immediately or stored under an argon atmosphere.

2.8 NMC cleaning, gold deposition and removal

The NMC arrays were directly immersed in a solution of ammonia, hydrogen peroxide and distilled water (1:1:5 vol./vol.) and heated to 70°C for 20 min. Afterwards the NMCs were carefully rinsed with distilled water and dried in a stream of nitrogen.

To ensure one-sided coatings of the NMC, the backside of the NMC was passivated by evaporation of a 30 nm thick layer of gold via thermal evaporation (0,1 nm/s, p ≈ 2 x10^{-5} mbar) (BALTEC MED 020, BALTEC, Balzers, Lichtenstein). For partial gold deposition, a shadow mask was placed over the NMC array.

After conclusion of the coating process, the protective gold layer was removed by immersing the NMC array in a KI/I_2 solution and rinsing with Millipore water.

3. "Grafting-to" of pentafluorophenol end-functionalized polymers

3.1 Introduction

In order to study polymer brushes with NMCs a method was required to obtain polymer brushes on top of single NMCs. Ideally, the used method should meet the following requirements:

- The obtained polymer brushes should have a defined molecular weight with a narrow molecular weight distribution.
- Each polymer chain should be attached to the surface by a single bond.
- The method should allow the preparation of mixed polymer brushes.
- The method should allow the preparation of partial coated NMCs.
- The method should allow the preparation of polymer brushes on NMCs as well as large-scale samples with the same characteristics.

A partial coating of NMCs by a "grafting-from" approach, like introduced by Bumbu et al.[66], would require multiple gold masking steps of the NMC and is not practically given the fragile nature of NMC arrays. A "grafting-to" approach using a UV-sensitive linker as used by Lenz et al.[22] result in multiple bonding sites of each polymer chain with the surface.

Recently, Roth et al.[115] presented a RAFT-starter carrying a pentafluorophenol functional group. This active ester function allows to one react the resulting polymer with amine functionalities. By utilizing a controlled radical polymerization, the end-functionalized polymer has a controlled molecular weight and a low PDI. Minko et al.[35] obtained mixed polymer brushes by depositing carboxyl-terminated polymers on an epoxy-functionalized silicon surface. Consecutively the precursor film is heated above its T_g, the carboxyl-group of the polymer chains reacts with the epoxy group on the surface, thereby grafting the polymer to the surface.

In this work the RAFT-starter, developed by Roth et al., is used to obtain pentafluorophenol (PFP) end-functionalized PMMA and PS. On the lines of the

"grafting-to" method, described by Minko et al., the PFP-polymer was deposited on an amine-functionalized surface and heated above its T_g to form the desired polymer brush.

3.2 Experimental

3.2.1 Pentafluorophenol-poly(methyl methacrylate)

1,44 ml (13,5 mmol) of freshly distilled methyl methacrylate, 11,1 mg of AIBN, 2 ml of dioxane and 120,8 mg of pentafluorophenyl-(4-phenylthiocarbonylthio-4-cyanovalerate)[115] were added to a Schlenk tube under an argon atmosphere. The mixture was degassed by three freeze-pump-thaw cycles. The polymerization was carried out at 75°C for 12 hours. The polymer was precipitated three times in methanol from THF The reaction yielded 2,8 g (69%) of pink pentafluorophenol-poly(methyl methacrylate) (PFP-PMMA) with a molecular weight M_n(GPC)= 16200 g/mol with a PDI (GPC) = 1,08.

3.2.2 Pentafluorophenol-polystyrene

5,63 ml (48,8 mmol) of freshly distilled styrene, 11,1 mg of AIBN, 3 ml of toluene and 120,8 mg of pentafluorophenyl-(4-phenylthiocarbonylthio-4-cyanovalerate) were added to a Schlenk tube under an argon atmosphere. The mixture was degassed by three freeze-pump-thaw cycles. The polymerization was carried out at 110°C for 4 days. The polymer was precipitated three times in methanol from THF. The reaction yielded 2,2 g (40%) of pink pentafluorophenol-polystyrene (PFP-PS) with a molecular weight M_n(GPC)= 13500 g/mol with a PDI (GPC) = 1,15.

3.2.3 (3-Aminopropyl)dimethylethoxysilan self assembled monolayer

The cleaned wafers were put into a Schlenk tube filled with argon gas. Two drops of (3-aminopropyl)dimethylethoxysilan (APDES) (Figure 3.1A) were added and the Schlenk tube was evacuated for approximately 1 s. The Schlenk tube was placed into a vacuum oven at 120°C for 14 h. Subsequently the wafers were extracted with dichloromethane in a soxhlet extractor for at least 5 h.

3.2.4 "Grafting-to" of PFP-functionalized polymer

1 ml of a 2 wt% toluene solution of PFP-PMMA/PFP-PS (Figure 3.1B/C) was spin-coated onto a APDES-functionalized wafer for 30 s at 1000 rpm. Afterwards the film was heated to 120°C for 90 min/12 h. The wafers were cooled down to room temperature and extracted with dichloromethane for at least 5 h.

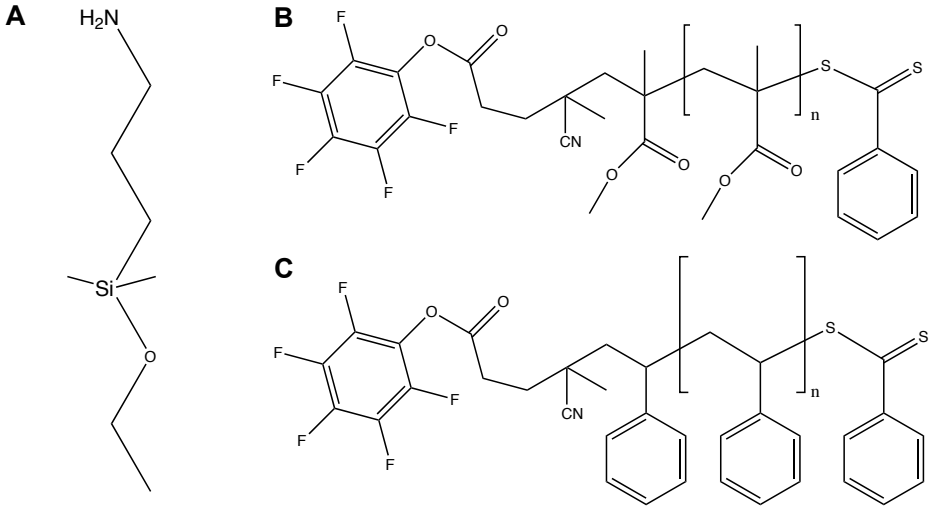

Figure 3.1: Chemical structures of the used silane (A) and the obtained active ester end-functionalized PMMA (B) and PS (C).

3.3 Results & discussion

To obtain polymer brushes via a “grafting-to” approach, an active-ester end-functionalized polymer was synthesized. The PFP-PMMA (M_n = 16200 g/mol) had a low PDI of 1,08 characteristic of a controlled radical polymerization. Due to the decreased reactivity of the styrene compared to the methyl methacrylate, the reaction time as well as the temperature had to be increased, in order to obtain polymer with a similar molecular weight (PFP-PS: M_n = 13500 g/mol). Both changes in experimental condition cause an increase in the resulting PDI to 1,15. In spite of the higher value, the PDI is well within the limits for a living radical polymerization. The pink color, stemming from the thiol-group, of the obtained polymer as well as the resulting NMR spectra confirm the presence of the thiol-group at the end of the polymer.

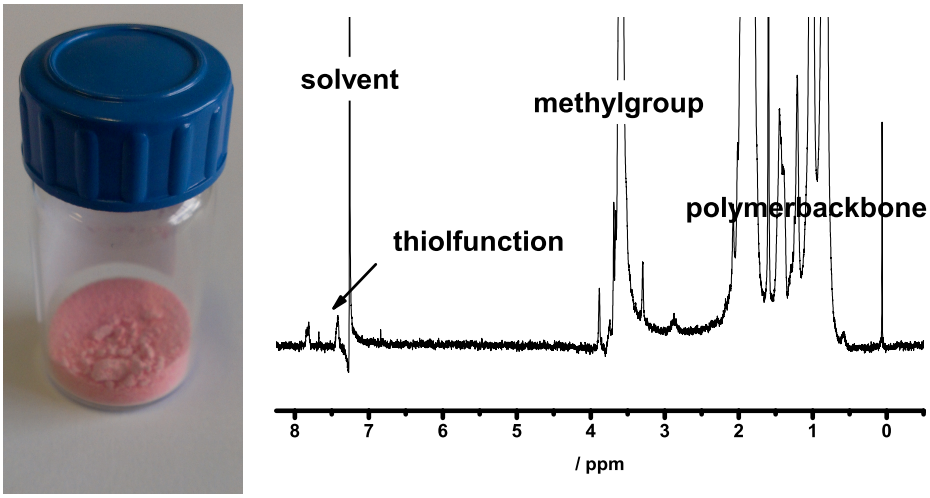

Figure 3.2: Optical image and NMR spectra of PFP-PMMA.

The needed amine-functionalized surface was produced by a vapor phase reaction. The obtained film showed a film thickness of 0,8 nm measured by XRR (Figure 3.3), corresponding nicely to the proposed monolayer of APDES.

XRR curves (Figure 3.3) after the deposition of the precursor polymer film, and subsequent heating, confirm the formation of a d_{PMMA} = 3,6 nm and d_{PS} = 6,0 nm thick polymer film. This corresponds to grafting densities of Γ_{PMMA} = 0,13

chains/nm² / Γ_{PS} = 0,28 chains/nm² and chain tethered densities of Σ_{PMMA} = 3,44/ Σ_{PS} = 10,41. The data is in good agreement with the anticipated increase in "grafting" with increasing heating time.

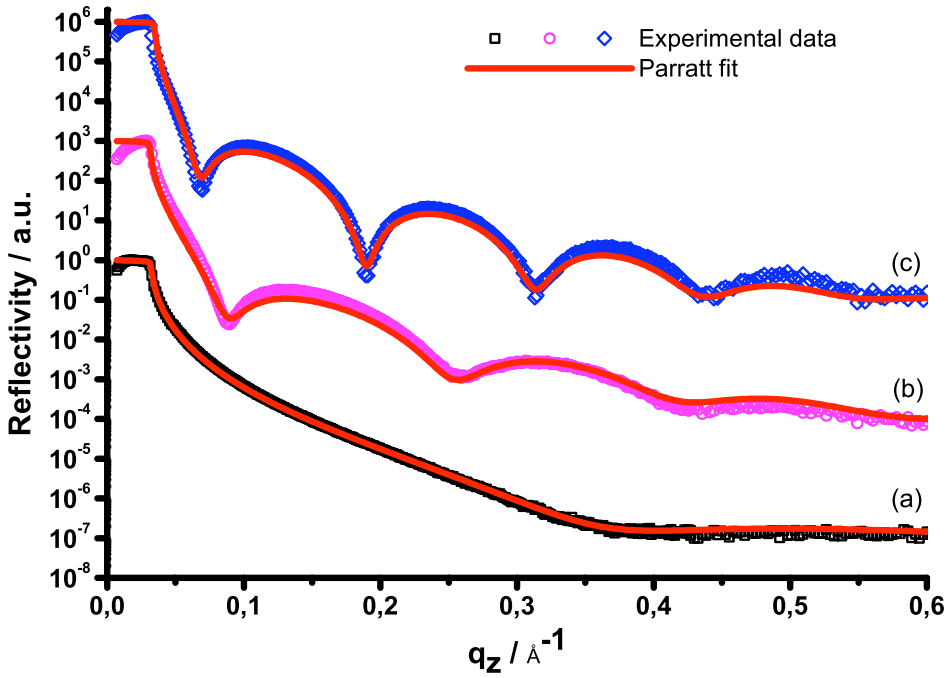

Figure 3.3: X-ray reflectivity curves of the self assembled monolayer of APDES (a) and the obtained "grafted-to" PMMA (b) and PS (c) brush films.

During the deposition of the film it only takes several seconds for the solvent to evaporate. Afterwards, the polymer chains are immobilized preventing the active-ester end group to react with the amine-functionalized surface. When the sample is heated above the glass transition temperature of the polymers, the chains are mobilized again. This enables the formation of covalent bonds between the surface and the polymer by the reaction of the amine-function on the surface and the active ester end groups. The time-span of heating is much longer compared to the deposition; because of this almost all bonds are formed during the heating procedure. The resulting film thickness is independent of the thickness of the deposited film since only the polymer chains close to the surface will react. The resulting film thickness is, therefore, a function of temperature as well as the time of heating. This allows one to tune the grafting densities by varying the time as well as the temperature of the heating step.

3.4 Conclusion

The presented “grafting-to” method is a viable option to obtain polymer brushes. The used controlled radical polymerization produces end-functionalized polymers with low PDIs. Due to the end-functionalization, the chains have only one way to bind to the surface. The fact that the resulting film thickness mostly depends on the heating time allows one to tune the grafting density. This is very helpful for the production of mixed polymer brushes by a step-by-step “grafting-to” technique (Chapter 5). Application of the PFP-polymer by spin coating for large area sample, or by inkjet printing for NMC samples has no effect on the resulting brush thickness. This guarantees a high comparability of the samples. The applicability of inkjet printing also allows one to obtain partial coating of NMC, by simply modifying the printing pattern.

In summary, one can conclude that the presented method fulfills all the requirements set for the preparation of mixed polymer brushes on large-scale samples as well as for the partial coating of NMCs.

4. Simplifying nanomechanical cantilever sensors

Part of the chapter is being prepared for publication in:

Ochsmann, J.W.; Cavaliere, A.; Lenz, S.; Raitieri, R.; Gutmann, J.S.; Berger, R.; Sensors and Actuators B: Chemical, in preparation.

4.1 Introduction

Besides the benefit of obtaining absolute curvature, the readout of NMC by PSI has also a great flexibility in terms of sample geometry. Since the topography of the entire illuminated area is obtained, the number and configuration of the NMCs can be chosen freely within the area. Determination of individual curvature values can be done by suitable software analysis. Kelling et al.[116] demonstrated a setup were 8 different NMCs on 4 separate arrays could be read out simultaneously under the same conditions. By this means, they envisioned the simultaneous readout of 160 NMCs on 20 separate arrays.

Helm et al. demonstrated that the investigation of NMC segments at the apex of the NMC is enough to obtain reliable curvature values when compared to the entire bending profile[79]. The question whether the position of the segment on the NMC matters or not remained unanswered. By directly measuring the curvature the obtained values do not depend on the size of the investigated area. This should allow to directly compare different segments, regardless of their size. Consequently, it should be possible to perform multiple bending experiments on a single NMC. If possible, this would be an elegant way to increase the readout curvature per NMC and consequently per measurement.

In this chapter the home built interferometer is used to investigate NMC coated with Au, PS and PMMA brushes. In order to compare changing curvature values, a procedure is introduced to measure the degree of correlation.

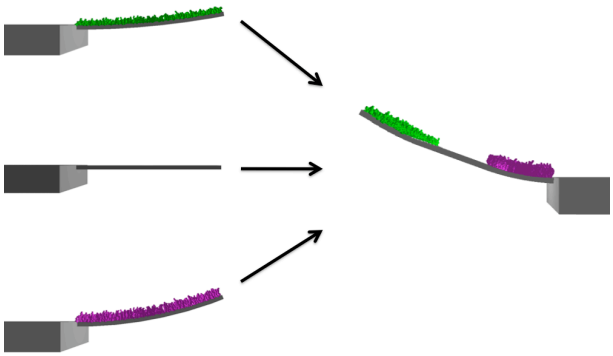

Figure 4.1: Schematic representation of the concept of multiple bending experiments performed on a single NMC.

4.2 Experimental

4.2.1 NMC coating

The gold-coated NMCs were prepared by evaporation of a 50 nm thick layer of gold via thermal evaporation. Partial Au coatings of NMC were obtained by placing a glass slide over part of the NMC array inside the evaporation chamber.
For polymer coating of the NMC the "grafting-to" technique developed in chapter 3 was utilized. Two drops, each about 0,4 nl, of 2 wt% toluene solution of PMMA or PS, were deposited at the top, the middle and the end of the NMCs using the Nano-Plotter. For partial coated NMCs no solution was deposited at the middle position. Consecutively the NMCs were heated to 120°C for 14 h.

4.2.2 Bending experiments

Heating experiments were conducted by heating the sample from 25°C to 50°C at a rate of 0.1°C/ min. During the heating a measurement was performed every 10 s.
The polymer-coated NMC were exposed to acetic acid (AA) and dichloromethane (DCM) vapors by directing nitrogen gas (p = 1,2 bar) through a gas-washing bottle

filled with acetic acid and dichloromethane respectively. In between the NMC were exposed to pure nitrogen gas. To avoid condensation of solvent inside the sample cell, the temperature was set to T = 25°C. Meanwhile a measurement was performed every 5 s.

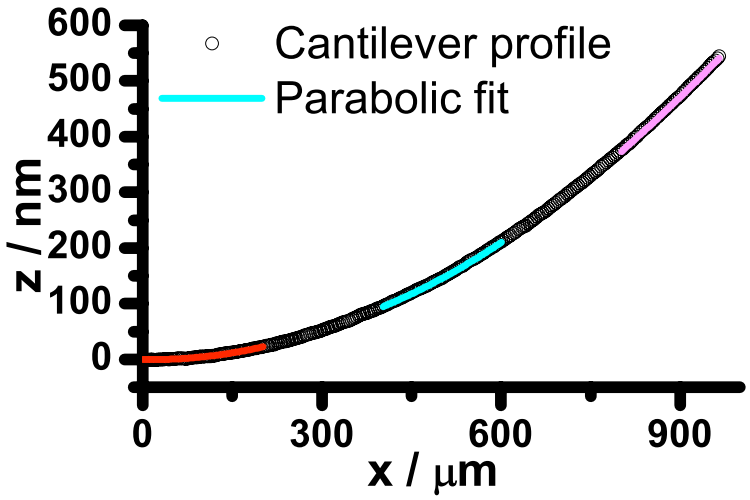

Figure 4.2: NMC profile with segmental parabolic fit obtained for local curvature measurements.

4.2.3 Local curvature measurements

During the heating experiments, the change in curvature was followed by fitting the entire NMC profile and monitoring the change in curvature over time. For the local curvature analysis the offline mode was utilized. The NMC segment of interest was selected and fitted for each measurement of the conducted experiment. Thereupon, the step was repeated for each segment of interest (Figure 4.2).

4.3 Results & discussion

4.3.1 Correlation of constant curvature values

At first the possibility and limitations of segmental NMC curvature analysis within the PSI setup are investigated. Therefore, a NMC coated with Au by thermal

evaporation was investigated. Such Au coatings are homogeneous in thickness and roughness and are easy to be prepared. Thus, one does not expect severe differences in the curvature along the NMC. As a start the gold-coated NMC was measured at constant room temperature. To investigate the minimal segment size Δx applicable to our setup, the length was decreased from the full length of a NMC (1 mm) stepwise down to the smallest length applicable to a parabolic fit (3 pixels at the CCD camera ≈ Δx = 10 µm in our setup). Each segment was centered in the middle of the investigated NMC (Figure 4.3a). For comparison of the curvature values $\kappa_{\Delta x}$, obtained from each segment to the overall curvature κ_{Full} value, the relative curvature value κ_{rel} was calculated.

$$\kappa_{rel;\Delta x} = \frac{\kappa_{\Delta x}}{\kappa_{Full}} \tag{28}$$

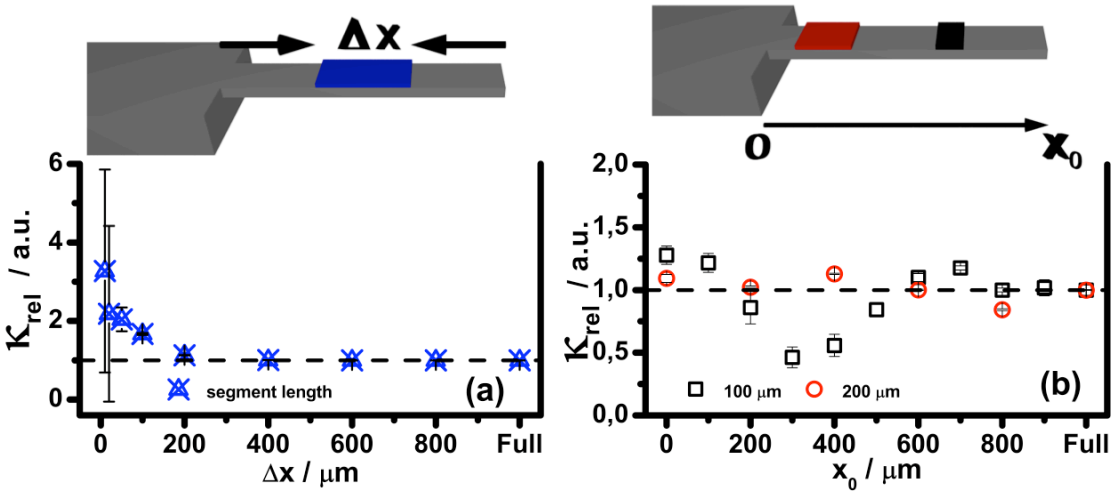

Figure 4.3: :(a) Relative curvature κ_{rel} plotted against the investigated segment length (Δx). (b) Relative curvature κ_{rel} values for 100 µm (black squares) and 200 µm (red circles) plotted against the segment starting position (x_0). The dashed line and value indicated with "Full" mark the value $\kappa_{rel;Full}$. Illustration shows schematic representation of Δx and x_0.

For measurements at constant room temperature (Figure 4.3a) segments Δx > 400 µm showed a value of 0.99< κ_{rel} <1.01. For smaller segments of Δx = 100 µm and Δx = 200 µm also the dependence of the curvature on the segments starting position x_0 (Figure 4.3b) was investigated. Therefore, the curvatures were determined along the whole length of the NMC at 10 or 5 different positions (x_0), respectively

(Figure 4.3b). Since averaging over these values would result in a loss of information, the average deviation from the ideal value 1 was calculated. For 100 µm segments an average deviation of 20 ± 6%, and for a 200 µm segment an average deviation of 8 ± 1% from $\kappa_{rel} = 1$ was measured. The maximum deviation were obtained for $\kappa_{rel;100\mu m;x0=300\mu m} = 0{,}46$ and $\kappa_{rel;200\mu m;x0=800\mu m} = 0{,}84$. Smaller segments sizes of 50, 20, 10 µm showed $\kappa_{rel} > 2$.

4.3.2 Correlation of changing curvature values

NMC sensors are typically used for the measurement of a change in curvature of a functionalized NMC relative to a reference. Therefore, the absolute value of curvature κ is here of minor interest, but the change in curvature $\Delta\kappa$ is rather important. To generate a change in curvature, the gold-coated NMC was heated from 25°C to 50°C. The absolute curvature κ_{abs} was recorded for different sized segments (Δx) as well as positions (x_0) for 100 µm and 200 µm large segments as described above. Comparison of the changing curvature values by calculating κ_{rel} , as done so far, is not practically. Information which of the two κ_{abs} is changing or stays constant would be lost.

The analysis of the correlation of two changing curvature values κ_{abs} was, therefore, done by plotting the curvature values against each other. As an example, the curvature κ_{Full}, obtained along the full length of the NMC, is plotted against the curvature $\kappa_{200\mu m;x0=200\mu m}$, of a 200 µm segment ($x_0 = 200\mu m$)(Figure 4.4). The complete set of all correlation plots can be found in the appendix. The resulting plot was then fitted with a linear dependence

$$y = mx + b \qquad \textbf{(29)}$$

with m being the slope and b the y-curvature offset.

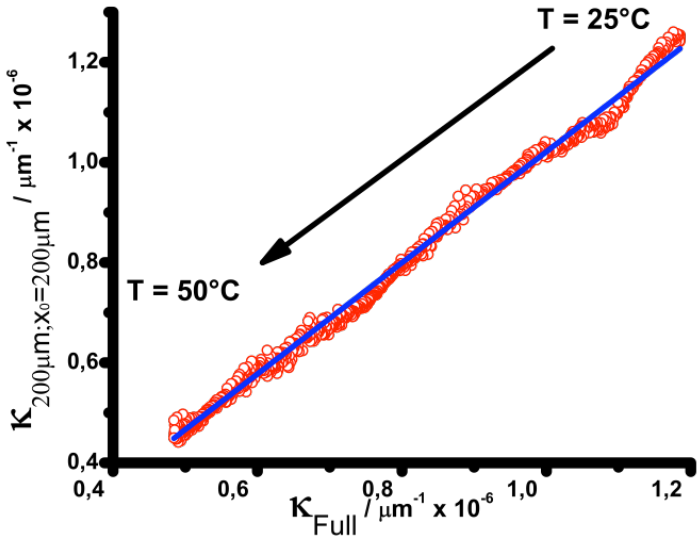

Figure 4.4: Example of a κ_{Full} vs. $\kappa_{200\mu m;x0=200\mu m}$ plot for correlation of changing curvature values of a gold-coated NMC during heating from T=25°C to T=50°C. x_0 indicates the starting position of the investigated segment on top of the NMC. Open symbols display experimental data. Lines display linear fit.

A perfect compliance between the measured curvature values would result in a straight line with a slope of m = 1. A slope of m = 0 would resemble a constant value of curvature, characteristic of a reference signal. A negative slope m would indicate a change in curvature $\Delta\kappa$ in the opposite direction as the curvature plotted on the x-axis.

Although the correlation between two curvature values does not result in a slope of m = 1, they still might be linear correlated. This might be the case for NMC which (i) are only partially coated, (ii) have coatings with different grafting densities or (iii) thickness. To measure this degree of linear correlation, the correlation coefficient Pearson R (RP) is used. The coefficient describes the correlation between two linear dependent variables. A perfect correlation has the value $R_P = 1$, while a value of $R_P = 0$ describes two linear uncorrelated variables. For the example shown in Figure 4.4 this resulted in $m_{200\mu m;x0=200\mu m} = 1{,}11$, $R_{P200\mu m;x0=400\mu m} = 0{,}99$ and $b_{200\mu m;x0=200\mu m} = -4.4\times10^{-8}$ µm^{-1}. One can therefore conclude that compared to the overall change in curvature, the investigated segment shows a higher change in curvature with a high linear dependence.

If the correlation results in $m \approx 1$ and $R_P \approx 1$, the y-curvature b can be seen as a measure for the offset in absolute curvature values of the two correlated values.

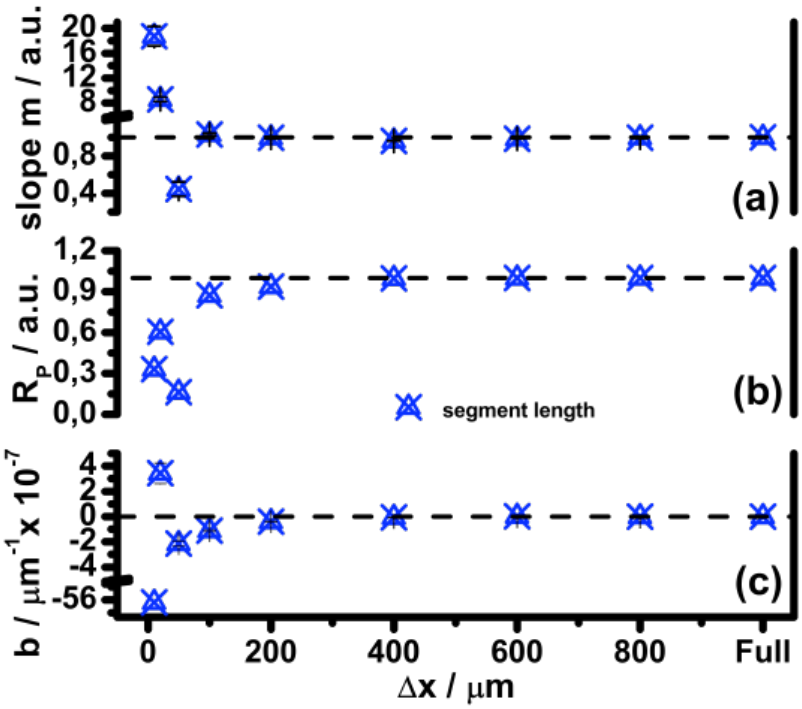

Figure 4.5: Slope m (a), Pearson R R_P (b) and y-intercept b (c) values for different segment length obtained from the curvature measurement of a gold coated NMC during heating from 25°C to 50°C.

In order to compare the obtained data, the slope and R_P values were plotted against the segment size Δx (Figure 4.5). Larger segments Δx > 400 μm resulted in slopes of 0,96 < m < 1 and a R_P > 0,99. This is evident of a high degree of compliance and linear correlation. The resulting low values of the y-curvature offset (b < 4×10^{-8} µm^{-1}) are evident of a also high compliance of the absolute values.

In order to investigate the influence of x_0, 100 µm and 200 µm, long segments along the full length of the NMC were investigated (Figure 4.6). For both segment sizes the slope values m < 1 and m > 1 were obtained. Since averaging over these values would result in a loss of information, the average deviation from the ideal value 1 was again calculated. Segments of 200 µm length showed an average deviation of 5% from a slope of 1 and an average $\overline{R_P}$ > 0,99. The y-intercept showed an averaged deviation of $\overline{b}_{200\mu m}$= $2,9\times10^{-8}$ µm^{-1}. The maximum deviation was found for $m_{200\mu m;x0=200\mu m}$ = 1,11 , $R_{P200\mu m;x0=400\mu m}$ = 0,99 and $b_{200\mu m;x0=200\mu m}$ = -

$4{,}4\times10^{-8}$ μm^{-1}. The high R_P values of all segments are evident of a high compliance. The deviations in slope are, therefore, probably due to local heterogeneities in the NMC coating. Since there is a deviation from m = 1, no conclusion about the offset in absolute curvature values can be drawn from b.

Segments of 100 µm resulted in an average deviation of 13±1% from a slope of 1 and a $\overline{R_P}$ = 0.90. The y-intercept showed an averaged deviation of $\overline{b}_{100\mu m}$ = $1{,}0\times10^{-7}$ μm^{-1}. The maximum deviation was found for $m_{100\mu m;x0=200\mu m}$ = 0,73, $R_{P100\mu m;x0=100\mu m}$ = 0,82 and $b_{100\mu m;x0=300\mu m}$ = $-3{,}7\times10^{-7}$ μm^{-1}. Reducing the size of the segment also reduces the number of fitted data points. With a pitch of 3,2 µm a 100 µm segment consist only of 31 data points in the presented setup compared to 230 data points of a full NMC. When comparing the values from Δx = 200 µm segments to the corresponding two Δx = 100 µm segments, no correlation in their deviations from the full-length value can be found. One can therefore conclude that the deviations are mainly caused by the uncertainty in the fit due to the decreased number of data points.

Smaller segments Δx ≤ 50 µm showed large deviation from m =1, R_P < 0,6 as well as $|b| > 2\times10^{-7}$ μm^{-1} due to the again reduced number of analyzed data points and the, therefore, increased uncertainty of the fit.

In summary, one can conclude that segments of 200 µm are sufficient to obtain reliable curvature values with an error < 6 % when compared to the curvature value of the full NMC. Even smaller segments of 100 µm still show a relative high compliance with the full curvature value with an error < 13 %.

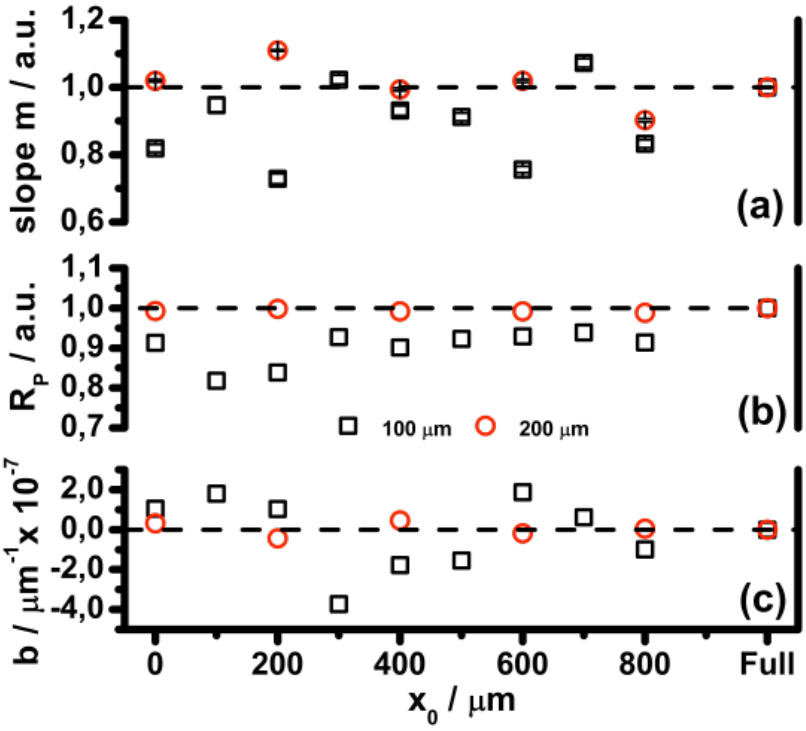

Figure 4.6: Slope m (a), Pearson R R_P (b) and y-intercept b (c) values for 100 µm (black squares) and 200 µm (red circles) plotted against the segment starting position obtained from the curvature measurement of a gold coated NMC during heating from 25°C to 50°C.

4.3.3 Determination of segment position

For the functionalization of NMCs, inkjet printing has been proven to be a powerful tool.[90, 91, 117] With the ability to deposit small volumes on top of individual NMC it is also a promising pathway for partial NMC coatings. However, especially the deposition of polymer solutions goes along with an uncertainty in position and size of the coated area on top of the NMC. This is caused by spreading and/or drying effects, e.g. the coffee stain effect[92]. Therefore, a precise determination of the position of the different coated segments on each NMC would be desirable. Identification of different coated NMC segment, might be done by ellipsometry[74] or optical microscopy.[118] However, this is not possible for optical transparent system,, like thin polymer brush films. In any case it would require additional experimental effort and would be difficult to automatize. Therefore, it is investigated whether

step-wise shifts of the segment that is analyzed can be used to identify different coated segments.

As a simple model system partially gold-coated NMC are used. The partial coating was obtained by a glass slide placed over the tip region of the NMC. The glass slide was slightly tilted with respect to the NMC to obtain different sized uncoated segment on top of the NMC (Figure 4.7). In order to identify the uncoated segment, the NMC was heated from 25 to 50°C. To identify the boundary between the coated and uncoated NMC segments, 100 µm segments were analyzed. The starting positions x_0 were shifted by 10 µm with respect to each other. The obtained curvature values were plotted against the value from the gold-coated segment $\kappa_{100\mu m;x0=300\mu m}$. The resulting slope m was plotted against the starting position x_0 of the investigated 100 µm long segment (Figure 4.7).

Both NMCs show a steep drop in slope increasing from a value of $m \approx 1$ to values around $m = 0$. The values at low x_0 are in good agreement with a gold-coated segment. For a gradual transition between two differently coated segment of the NMC a stepwise decrease of the resulting from $m = 1$ to $m = 0$ would be expected. The resulting plots show rather steep transitions and also slop values of $m < 0$. One can, therefore, conclude that the curvature values of segment, containing both coated and uncoated area, cannot be viewed as a weighted average of the curvature values. The transition between two different coated segments rather results in an increase in uncertainties in the fit. Therefore the sharp transition can be identified as the end of the coated area.

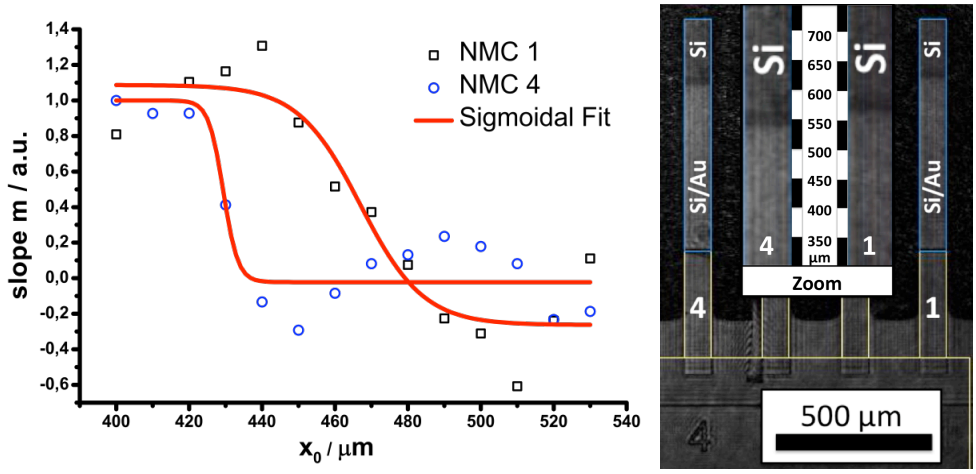

Figure 4.7: Obtained slop values m plotted against the segments starting position on top of the NMC. Empty symbols display experimental values, red line display performed sigmoidal fit. Optical image of the investigated partial gold coated NMC 1 and 4. Inlet shows magnification of the border between the gold-coated and uncoated segment.

If the data points are fitted with a step-like sigmoidal function,

$$y = \frac{A_1 - A_2}{1 + e^{(x - x_0)/dx}} + A_2 \qquad \textbf{(30)}$$

the fit yields inflection points of x_0= 467 µm (NMC 1) and x_0 = 429 µm (NMC 4). Since the transition from the coated to the uncoated area happens at the end of the investigated segment, the segment length (100 µm) has to be added to x_0. The resulting values are in good agreement with values obtained from the optical image of around 570 µm and 530 µm respectively (Figure 4.7).

4.3.4 Polymer brush coated NMC

To further investigate the applicability of local curvature measurement, a NMC coated with polymer brushes is investigated. Especially, NMC coated with stimuli-responsive polymer brushes have attracted scientific interest.[22, 23] By this means, a variety of sensors have been developed.[60, 67, 68] Polymer brush layers are thin and can hardly be seen by standard optical microscopy. Thus, polymer brush layers are a good test system for the local NMC analysis, as outlined above for an Au coating.

Partially coated NMCs with PS and PMMA brushes were obtained using the "grafting-to" technique, with a thickness of d ≈ 5 nm.

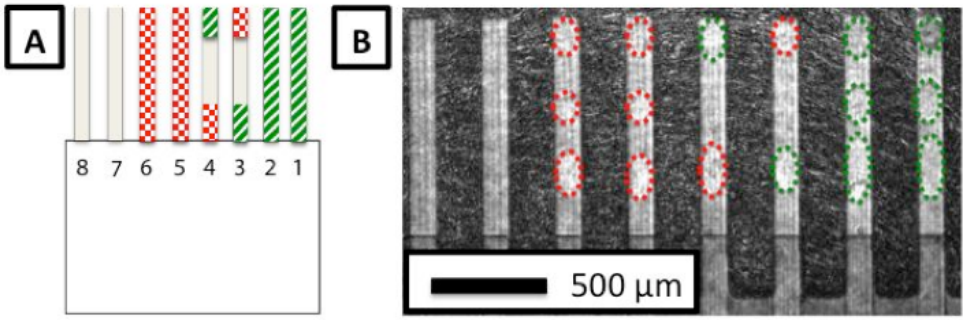

Figure 4.8: Sketch of the NMC array (A) partially coated with PMMA (striped pattern) and PS (checkerboard pattern). Optical image (B) of the investigated NMC array the barely visible areas coated with polymer brushes are circuit in green and red respectively.

The obtained NMC consisted of a region coated with PMMA brushes, an uncoated area in the middle of the NMC and a polystyrene coated area at the tip of the NMC (Figure 4.8). To be able to compare the result to the standard approach, additional NMC were tried be completely coated with PMMA and PS brushes by coating the NMC at the top, at the middle and at the end. Two NMC were left uncoated as reference NMC for comparison to the uncoated middle section. To induce a change in curvature, the NMCs were exposed to stream of saturated acetic acid (AA) vapor, a selective solvent for PMMA, dichloromethane (DCM), a good solvent for both polymers and pure N_2 to remove acetic acid and dichloromethane from both polymers.

At first the coated regions on the NMC 3 and 4 are identified. Therefore, 100 µm long segments are analyzed and correlated. For the coated area at the apex of NMC4, the plot (Figure 4.9a) of the slope m against x_0 shows two transitions corresponding to the edges of the coated areas, fitting the data resulted in inflection points of x_o = 80 µm and 130 µm. Therefore, the coated area ranges from x = 80-230 µm, in good agreement with the printing pattern and the optical image, although a coating closer to the apex was anticipated. At the tip of NMC4 the plot (Figure 4.9b) shows a sharp resulting in a fitted inflection point of x_o = 580 µm. No

second change in slope was measured. Therefore, one can conclude that the tip of the NMC was completely coated as designated from the printing pattern. Since similar results were obtained for NMC 3, segments of 150 µm were investigated at the apex. To obtain similar results to the investigated gold-coated NMC, 100 µm long segments at the tip of the NMCs, ranging from x = 580-680 µm were considered.

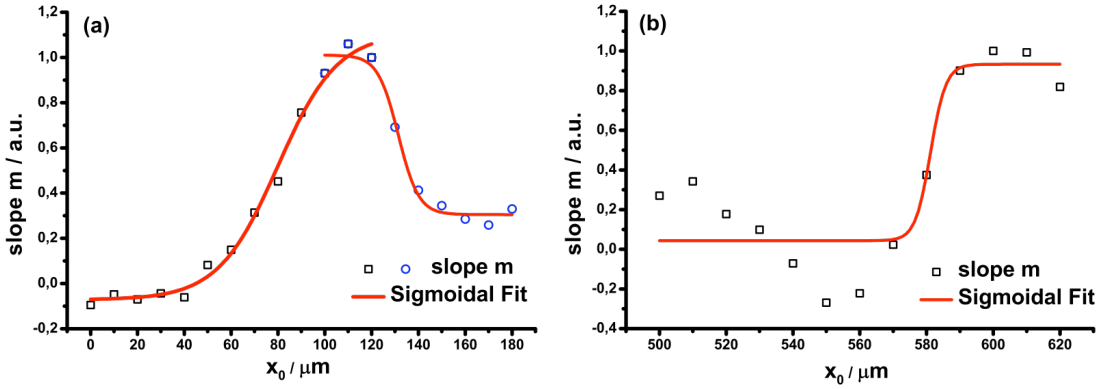

Figure 4.9: Slope of the investigated 100 µm long segment plotted against its starting position for the determination of the coated area at the base (a) and the tip (b) of the NMC 4. Open symbols display experimental data. Lines display sigmoidal fit.

The standard way to plot the measured NMC bending data upon exposure to solvents is to plot the change in curvature vs. time (Figure 4.10). Plotting the change in curvature vs. time allows one to nicely follow the responds of the NMC upon different environments.

Upon exposure to both, AA and DCM vapor, an increase in curvature was measured. Consecutive exposure to pure nitrogen gas let to a decrease in curvature in PS as well as the PMMA coated brushes. Exposition to solvent vapor of a good solvent causes the polymer brush to swell in order to maximize polymer solvent interactions. Bad solvents are also absorbed, but only in a reduced amount.[23] This results in a change in curvature. Due to the increased uptake in the case of PMMA, a higher change in curvature is measured. Subsequent exposure to pure nitrogen results in a decrease in curvature in PS as well as the PMMA coated brushes. The PS coated NMC almost goes back to the initial value, while the PMMA coated NMC equilibrates at a higher value of curvature. This is another indication

of the higher uptake and solubility of acetic acid inside the PMMA brush coating compared to the PS. Exposure of the NMCs to DCM vapor, a good solvent for both polymers, again resulted in an increase in curvature. Both PS and PMMA coated NMC react similar. The higher curvature of the PMMA is simply due to the unequal initial values. Consecutive exposure to nitrogen results in a reduction of curvature to the values before exposure to DCM.

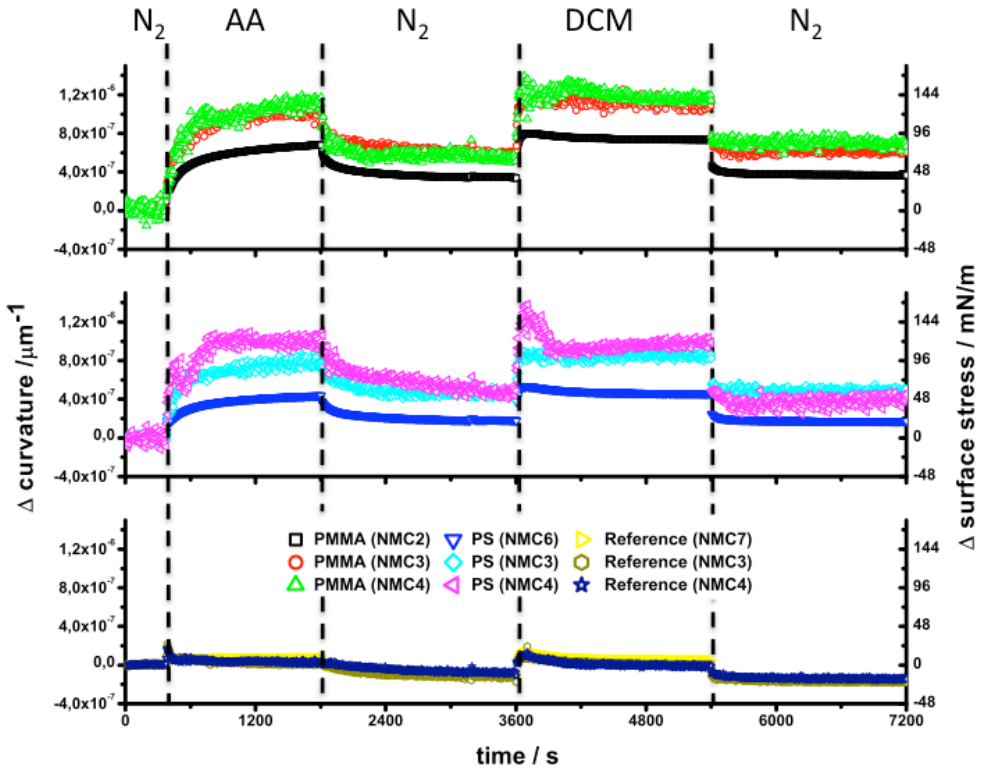

Figure 4.10 Change in curvature and surface stress upon exposure to acetic acid (AA) and dichloromethane (DCM). For partially coated NMC the local curvature is plotted while for the completely coated NMCs the curvature is determined along the full length of the NMC.

The plot also allows to qualitatively compare the different curvature data. One can conclude that the PMMA and PS coated segments as well as full NMC show the same responds upon exposure to the different solvents and nitrogen. Also the reference signal from the uncoated NMC 7 shows a high compliance to the uncoated segments on NMC 3 & 4. However, a quantitative analysis and conclusion on the correlation of changing curvature values is not possible. The data was,

therefore, correlated by plotting the curvature of the full NMC against the local curvature values.

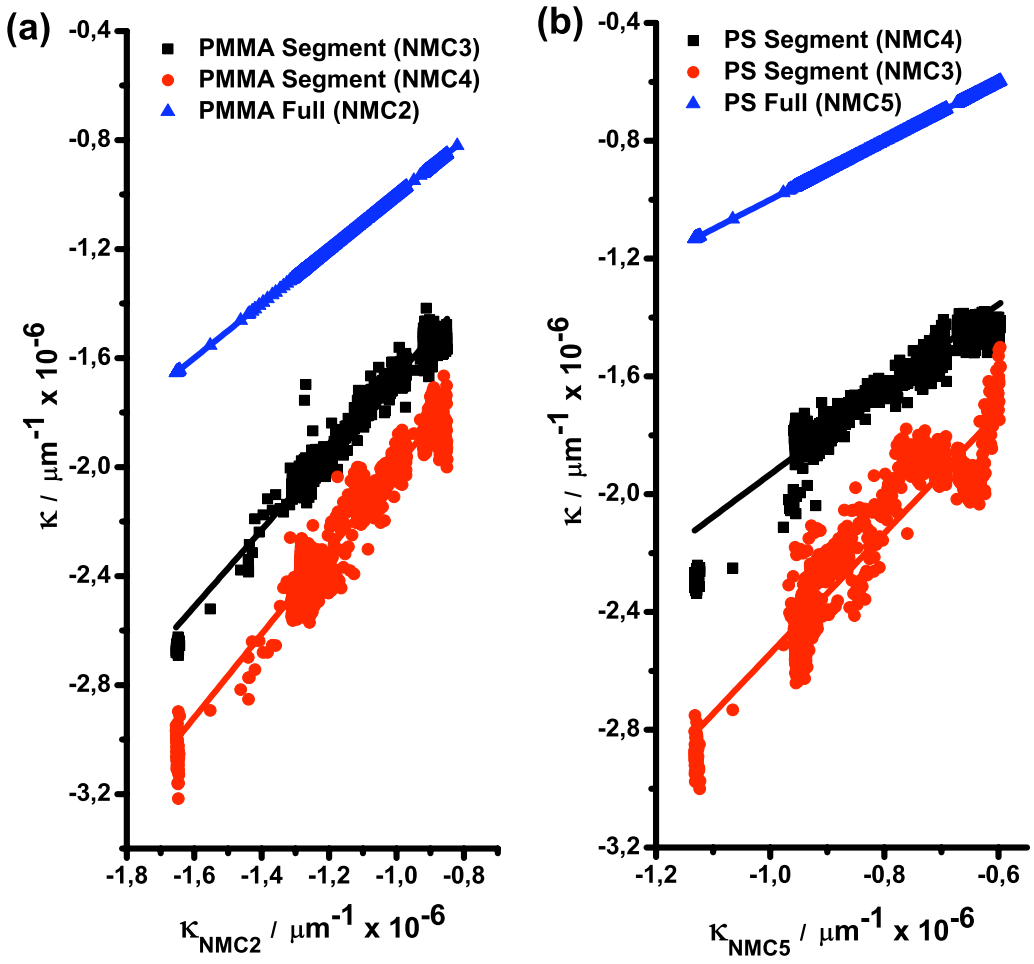

Figure 4.11: Curvature obtained from NMC fitted along its entire length plotted against curvature values obtained from NMC segment for PMMA (a) and PS (b). Symbols display experimental data. Lines display linear fit.

Correlation of the local curvature values of the PMMA coated segments of NMC 3 & 4 with NMC2 (Figure 4.11a) resulted in a $m_{PMMA\ 150/Full}$ = 1,41/ $m_{PMMA\ 100/Full}$ = 1,53 and a $R_{P\ PMMA150/Full}$ = 0,99/ $R_{P\ PMMA100/Full}$ = 0,98 respectively. Correlation of the PS coated segments with NMC 5 resulted in similar values, $m_{PS\ 150/Full}$ = 1,44/ $m_{PS\ 100/Full}$ = 2,04 and a $R_{P\ PS150/Full}$ = 0,96/ $R_{P\ PS100/Full}$ = 0,95. The high R_P values are evident of the linear correlation of the data, indicating a high comparability of the data. The obtained slope values, however, are always greater than 1 indicating a

higher response than the NMC fitted along its full length. This difference is already visible in the curvature vs. time plot.

By analyzing the obtained profiles of the NMC 2 (Figure 4.12a) and 5 one can see that the NMCs are not homogeneously coated. The printing pattern resulted in uncoated area between each drop. The not bend straight segments in between the drops cause an overall smaller curvature value. Local curvature measurements are performed in the center of the polymer coating (Figure 4.12b). Effects caused by the coating are therefore excluded. Although, correlation of the curvature goes along with a loss of the desired information, it was helpful in order to quantify the degree of correlation of changing curvature values.

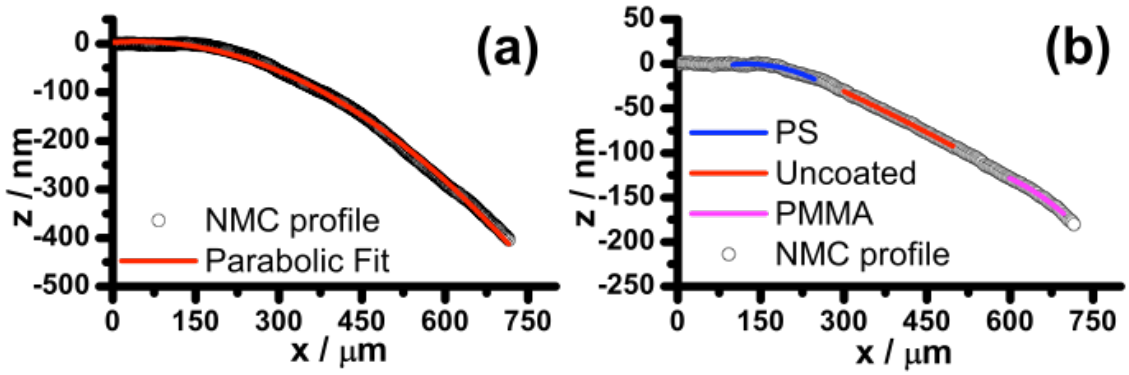

Figure 4.12:(a) Profile of NMC2 coated with PMMA brushes and parabolic fit along the full length of the NMC. (b) Profile of NMC 4 coated with PS and PMMA brushes. Parabolic fits are only performed in the center of the coated segments. Experimental data is displayed by open symbols and parabolic fits by lines.

4.4 Conclusion

The performed NMC bending experiments revealed that multiple measurements on a single NMC are possible. Comparable results for segments down to 100 µm regardless of their position of the investigated segment were obtained. By increasing the number of measurement points per NMC, e.g. by increasing the resolution of the CCD-camera, the deviations can be decreased. With that, even smaller segments below 100 µm would give reliable curvature values. Assuming

suitable NMC functionalization or preparation, the number of sensing areas for surface stress detection can be readily increased by a factor of 5.

Segmental analysis also shows a convenient way to determine the position of individual segments. This greatly simplifies the segmental analysis by avoiding the use of additional experimental effort. Therefore it is also a unique and simple method to account for difficulties in NMC preparation.

Correlation of curvature data might also be used in order to compare different NMCs. Deviation in the slope m with simultaneously high R_P values of alike-coated NMC could be a indication of difference in coating quality, or elastic modulus of the NMC itself.

Furthermore, local stress analysis might be combined with mass detection using higher modes of the resonance frequency [119]. By placing the functionalization layers at knots of higher modes, the mass changes of individual layers might be combined with local stress analysis in the layer.

Although, all measurements were performed using an interferometer, the principle of local curvature may be applied to every NMC readout technique supplying complete NMC profiles.

5. Stress-structure correlation in mixed thin PS-PMMA brush films

Part of the chapter has been published in:

Ochsmann, J.W.; Lenz, S.; Lellig, P.; Emmerling, S.G.J.; Golriz, A.A.; Reichert, P.; You, J.; Perlich, J.; Roth, S.V.; Berger, R.; Gutmann, J.S. *Macromolecules* **2012,** 45, (7), 3129-3136.

5.1 Introduction

Switchable polymer surfaces are a promising field of research.[120] The ability to switch surface characteristics such as morphology and surface energy upon external stimuli make them an interesting research topic. In addition, the possibility to move nano-objects on top of a surface by reversible switching of the polymer surface is a topic of current research.[121] Mixed polymer brushes, consisting of two different homopolymers covalently attached to a surface, are one candidate for these types of polymer surfaces.[30, 31, 34, 37, 122-124] Extensive theoretical research has been done in the last couple of years[125], studying the film morphology in relation to the polymer incompatibilities[20], solvent selectivity[126], composition[20] and chain length asymmetry[127]. Fluctuations in local "grafting-point" positions and its correlations have been investigated. With the help of “Single-Chain-in-Mean-Field” simulations it was shown that small fluctuations in grafting point positions influence domain locations and prevent long-range order.[41, 43] Although these simulations resemble the experimental findings,[38] the applied mean field approach neglects chain conformation. Microphase separation of chemical bond polymer chains requires a large amount of stretching of individual chains. These conformational restrains, and the resulting stress inside the polymer film, are not accounted for in the mean field approach.

In recent years, a domain memory effect has been experimentally observed in mixed polymer brush films. Santer et al. introduced a quantified measurement for domains forming at the same position; size and shape upon cyclically change.[38-40]

The effects of chemical structure and fluctuations of the grafting points have been investigated. The authors attribute the domain memory effect to small fluctuation on grafting points, nucleating the domains in the mixed brush. While this explains the static structure formation, the reason for the domain stability over time remains unsolved.

In this chapter the switching behavior of the mixed polymer brushes, after they have been immersed in a good solvent for both polymers (DCM) and a selective solvent for PMMA (AA), are investigated. The change in structure between the two equilibrium states is investigated by X-ray reflectivity, scanning probe microscopy, contact angle measurement, near-edge X-ray absorption fine structure and μ-focused grazing incidence small angle X-ray scattering. Using these methods enables one to obtain a comprehensive picture about the change in polymer confirmation before and after switching. Via bending experiments on NMCs coated with the PS-PMMA mixed brushes, the change in surface stress was measured. With the help of a phase shifting interferometer the 3D-topography of the NMC is determined. This allows one to obtain the bending profile of each individual NMC and with calculation of the absolute values of surface stress acting inside the film. Measuring these forces, gives a deeper understanding of the network inside the polymer brush and the surface memory effect.

5.2 Experimental

5.2.1 Wafer preparation

The schematic diagram of the preparation route can be found in Figure 5.1. A 2 wt% toluene solution of PFP-PMMA was spin coated onto the APDES-functionalized wafer for 30 seconds at 1000 rpm. Afterwards, the film was heated to 120°C for 90 min. The wafers were cooled down to room temperature and extracted with dichloromethane for at least 5 h.

A 2 wt% toluene solution of PFP-PS was spin coated on top of the PMMA film for 30 seconds at 1000 rpm. The film was afterwards heated to 120°C for 12 h. The

wafers were cooled down to room temperature and extracted with dichloromethane for at least 5 h.

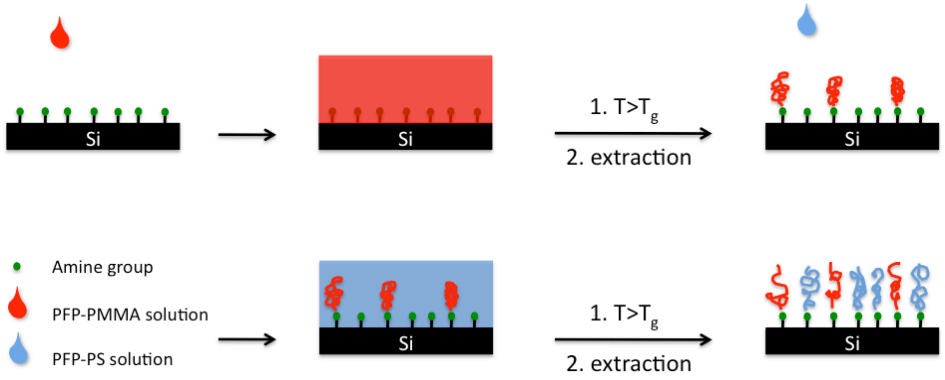

Figure 5.1: Schematic diagram of preparation route for the mixed PS-PMMA polymer brushes.

5.2.2 NMC preparation

For the preparation of homo- and mixed polymer on NMCs, a NMC array coated with gold on the backside was used. After APDES functionalization a 2 wt% toluene solution of PFP-PMMA was selectively applied to a NMC 1-4. The solution was deposited using the Nano-Plotter NP 2.0. The NMCs were printed by the array dispense procedure (ADP), dispensing a column of 15 drops 150 µm apart from each other. Using the program SpotFrontEnd©, the NMCs were aligned properly and a high reproducibility was obtained.

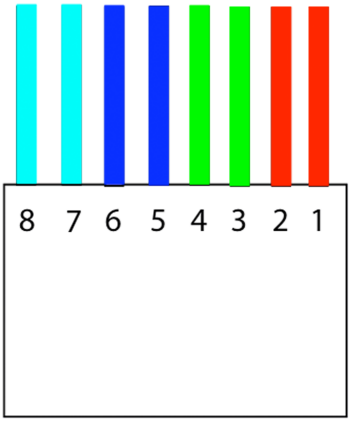

Figure 5.2: Scheme of the NMC array coated with mixed and homopolymer brushes. NMC 1 & 2 (red) are coated with PMMA homopolymer brushes, NMC 3 &4 (green) are coated with PS-PMMA mixed polymer brushes, NMC 5 & 6 (dark blue) are coated with PS homopolymer brushes and NMC 7 & 8 (light blue) are left uncoated as reference NMCs.

Next, the NMC sensor was heated to 120°C for 90 min, cooled down to room temperature and extracted in dichloromethane for at least 5 h. Afterwards, a 2 wt % toluene solution of PFP-PS was printed onto NMC 3-6. The NMC array was subsequently heated to 120°C for 12 h, cooled to room temperature and extracted in dichloromethane for at least 5 h. By this means NMC arrays are obtained, containing two NMCs coated with mixed PS-PMMA brushes, two NMCs coated with PS and PMMA respectively for comparison and two NMCs without polymer brushes as reference (Figure 5.2). At the end the protective gold layer was removed.

5.2.3 Solvent treatment

For the selective solvent treatment, the wafers/NMCs were immersed in conc. acetic acid and heated to 45°C for 30 min. The sample was then quickly rinsed with dest. water several times and dried in a stream of nitrogen gas. The procedure was repeated 3 times. For the non-selective treatment, the wafers/NMC arrays were immersed in dichloromethane for at least 90 min at 45°C and subsequently dried in a nitrogen stream.

5.3 Results & discussion

5.3.1 Film preparation

To obtain mixed polymer brushes on top of the amine-functionalized silicon surface, "grafting-to" approach developed in chapter 3 was utilized. The preparation of the mixed polymer brush film was followed by X-ray reflectivity to verify the proposed mechanism. The obtained reflectivity curves are shown in Figure 5.3. The treatment of the freshly cleaned silicon wafer with (3-Aminopropyl) dimethylethoxysilan leads to the formation of a 0,8 nm thick film. This corresponds nicely to the formation of a monolayer of APDES covalently bond to the silicon surface.

The analysis of the first prepared PMMA film yielded a 3,6 nm thick film with a relative low roughness of σ_{rms}= 0,3 nm. The following spin coating of the polystyrene solution led to an increase in thickness. The resulting film yielded a thickness of 5,1 nm and an increase in roughness to σ_{rms}= 0,5 nm. This consecutive increase in film thickness supports the proposed mechanism of step-by-step "grafting-to" of polymer chains to the same functionalized surface. The SPM images (Figure 5.6) at the end of the assembling process also supports the formation of a continuous and smooth polymer film.

The density ρ of the PMMA and the mixed PMMA-PS brushes were determined by the fit of the X-ray reflectivity. For the PMMA brush the value was 1,19 g/cm^{-3} equal to the literature[128] value of an unbound chain. For the PMMA-PS mixed brush case the value was 1,25 g/cm^{-3}, slightly above the literature values of PMMA and PS.[129] From the measured film thickness d, and the number average molecular weight M_n of the unbound homopolymer measured by GPC, the grafting density was calculated using the formula (2). The resulting grafting densities are Γ_{PMMA} = 0,13 chains/nm^2/$\Gamma_{PMMA\text{-}PS}$ = 0,26 chains/nm^2 with chain tethered densities of Σ_{PMMA} = 3,44/ $\Sigma_{PMMA\text{-}PS}$ = 7,87.

From the measured film thicknesses the brush composition can be estimated. If small differences in density are neglected, the composition of the mixed polymer brush can be calculated by dividing the film thickness of the PMMA film by the value of the PMMA-PS film. To account for the APDES layer, the 0,8 nm is subtracted from both film thicknesses. The PMMA-PS brush films have a composition of ~ 65% PMMA and ~ 35% PS.

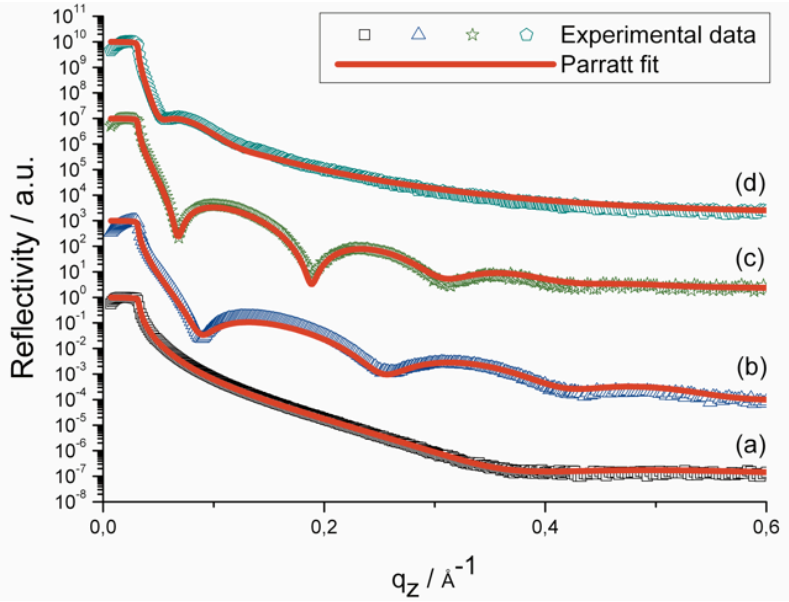

Figure 5.3: X-ray reflectivity curves of the monolayer of APDES (a); APDES/PMMA (b); APDES/PMMA-PS after treatment with dichloromethane (c) and acetic acid (d). Hollow symbols represent the experimental data. Straight lines represent the Parratt fit. The curves are shifted along the vertical axis for improved visualization.

5.3.2 Switching

Reports in literature[127] suggest that switching of the morphology takes several minutes. To check, if that is really the case, it is investigated if the conditions, typically (≈ 90 min at 45°C) used to cause the change in structure, are sufficient or not. To do so, the change in contact angle of a solvent drop of acetic acid and dichloromethane placed on top of the mixed polymer brush film was investigated. When the solvent drop gets in contact with the surface, the change in morphology

is induced. The change in morphology and surface composition causes a change in the contact angle. By measuring the change in contact angle over time, one can get an idea about the timescale of the induced change in morphology.

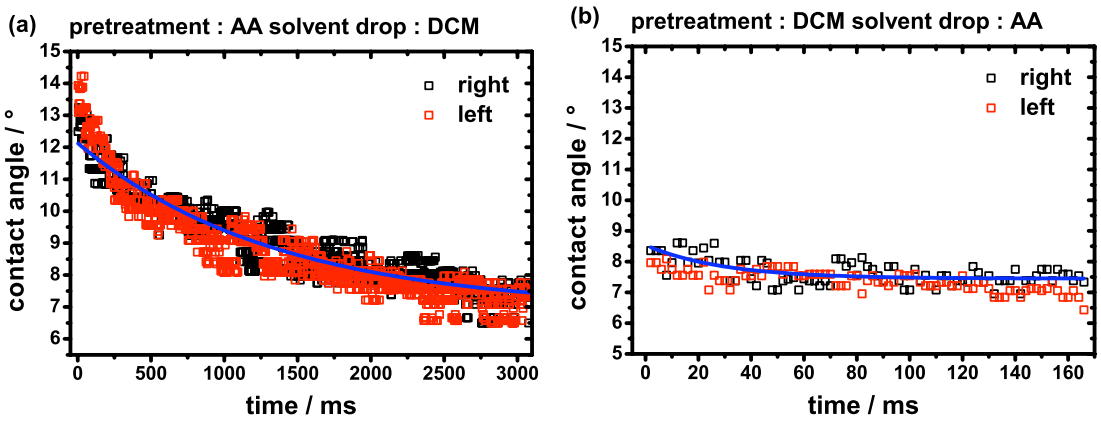

Figure 5.4: Contact angle vs. time for a solvent droplet placed on top of a pretreated mixed polymer brush film. Hollow symbols represent the experimental data. Lines are guide to the eye.

Both measurement showed identical change in contact angle on the right and left side of the drop. The absence of a hysteresis is evident of a homogenous film. The roughness of the film has also no effect, since the expected roughness features are orders of magnitude smaller than the solvent drop ($diameter_0$ = 2 mm). The dichloromethane drop placed on top of an acetic acid treated film shows a rapid decrease in contact angle (Figure 5.4a). After 3 s equilibrium is reached. For an acetic acid drop placed on a dichloromethane treated film the process is even faster and a contact angle of 7° is already reached after roughly 60 ms (Figure 5.4b).

Since the change in contact angle of the dichloromethane pretreated film was so rapidly, the switching was also investigated by NMCs. Therefore, the change in curvature of a dichloromethane pretreated NMC was measured upon exposure to acetic acid. Since the observed timescale of the switching in the contact angle measurement is orders of magnitude too fast for the resolution of the PSI (≈ 1 measurement/s), the NMC was exposed to acetic acid vapor and not to the solution. Decreasing the solvent concentration slows down the change in

morphology, and, therefore the change should happen in a timescale detectable by the PSI.

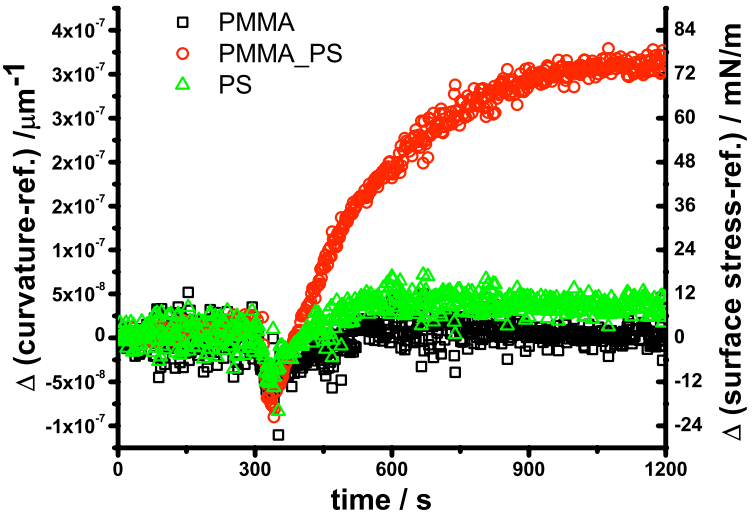

Figure 5.5: Change in curvature of dichloromethane pretreated NMCs upon exposure to acetic acid vapor at time 300s.

Upon exposure to solvent vapor the NMCs coated with homopolymer show an increase in curvature, reaching equilibrium after about 600 s. The mixed polymer brushes show a larger increase in curvature. However, compared to the homopolymer coated NMCs equilibrium is reached much later after 1200 s. The larger change in curvature as well as the longer timescale of the change in curvature is evidence of the change in morphology upon solvent exposure. Under higher solvent concentration in solutions, the change in morphology should happen much faster.

In summary, one can conclude that the change in morphology in solution happens in matter of seconds. The conditions for the morphology change, typically given in literature[38-40] (≈ 90 min at 45°C), are sufficient to reach a complete change in morphology. The elevated temperature should also speed up the change in morphology. Since these conditions proofed to be sufficient and to be comparable to the literature, the same conditions were used for the switching of the films morphology.

5.3.3 Structure

First, the change in structure caused by the switching upon different solvent exposure of the PS-PMMA mixed brushes was examined. Therefore, mixed polymer samples were prepared on silicon wafers and investigated before and after exposure to acetic acid, a selective solvent for PS, and dichloromethane, a good solvent for PS and PMMA, respectively.

Figure 5.6 shows an SPM height image of the same dichloromethane and acidic acid treated film. The immersion of the polymer film in acetic acid leads to the formation of nano domains, showing a dimple like structure. This change in structure is accompanied by a large increase in roughness from σ_{rms}= 0,23 nm to σ_{rms}= 0,65 nm (1x1 μm^2). Multiple line cuts were performed to measure the distance between nano domains. The analysis resulted in an average center-to-center distance of 27,5 ± 8.8 nm of the nano domains.

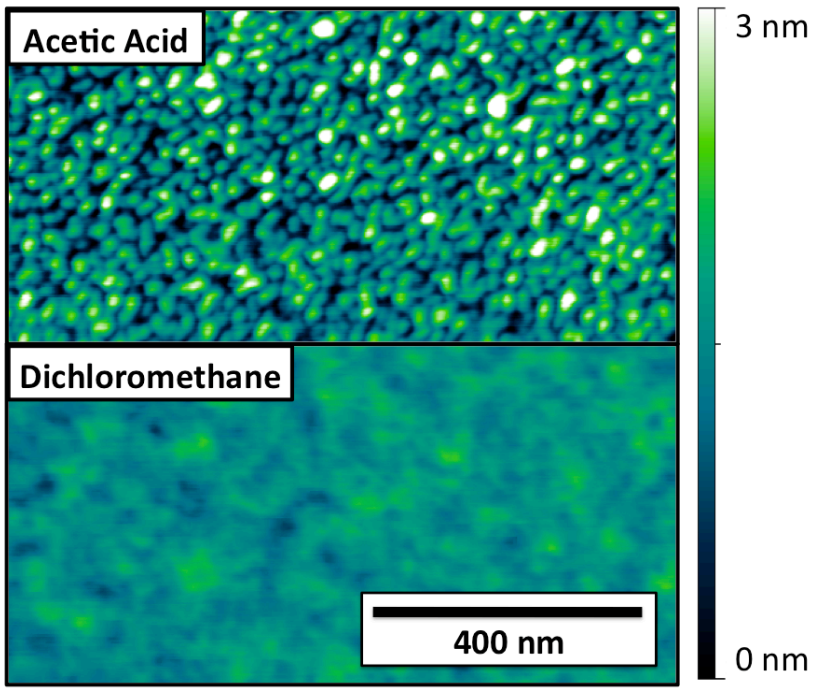

Figure 5.6: SPM topography images of the PMMA-PS mixed polymer brush film after acetic acid and dichloromethane treatment.

The change in structure can also be seen by XRR (Figure 5.3). The fitted reflectivity curve also confirmed the increase in roughness by a factor of ~ 3 which is also clearly visible by vanishing of all but one of the oscillations. The change in structure also leads to an increase in overall thickness from 5,1 nm to 6,7 nm.

To investigate the composition at the surface of the polymer film, contact angle measurements and NEXAFS studies were performed on acidic acid as well as dichloromethane treated films. The dichloromethane treated film showed a water contact angle of 76°. Treating the film with acetic acid led to a decrease in contact angle to 67° when compared to the dichloromethane film. The NEXAFS spectra of the acetic acid treated film shows an increase of the peak at 286,5 eV characteristic of polystyrene compared to the dichloromethane treated film. The peak characteristic for PMMA at 289 eV decreases after treatment of the film with dichloromethane. The measured increase of the more hydrophilic PMMA at the films surface is in good agreement with the measured decrease in water contact angle.

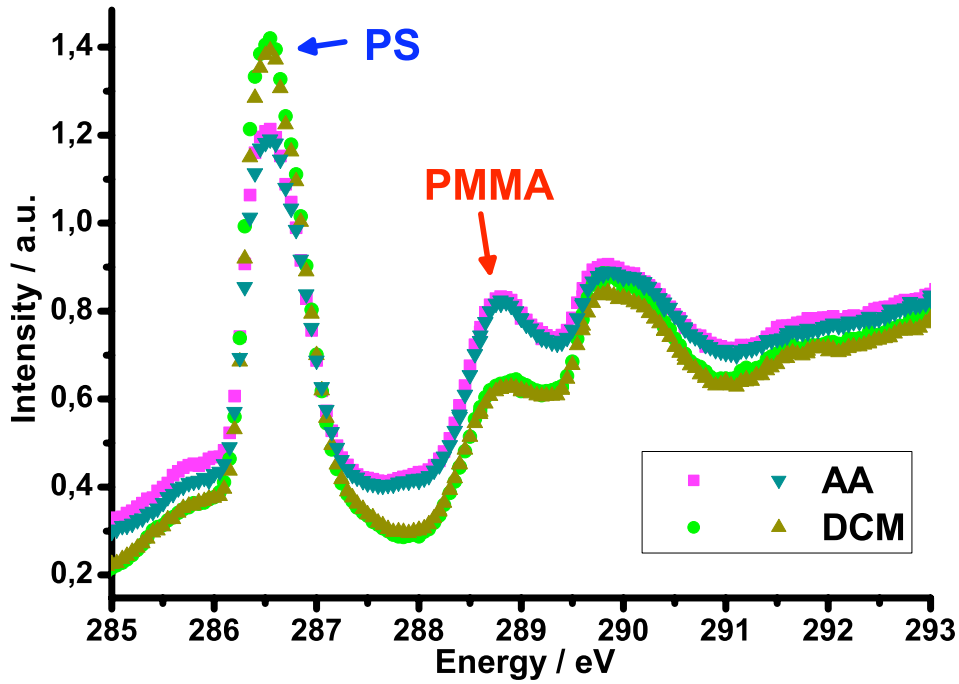

Figure 5.7: NEXAFS spectra of PS-PMMA mixed polymer brush film after treatment with acetic acid and dichloromethane.

Grazing incidence small angle X-ray scattering was performed to obtain a more averaged and quantified information on the morphology of the film. The incident angle was set to α = 0,4° which is above the critical angle of both the polymer film and the silicon substrate. Therefore, structural information from the surface as well as beneath was obtained. The horizontal GISAXS data (Figure 5.8) obtained from the acetic acid treated film showed a large and broad interference peak. Fitting of the data resulted in domains with an R_g= 6,5 ± 1.3 nm and a center-to-center distance of 19,4 ± 3,9 nm. These results can be related to the domains observed from the SPM images. One can, therefore, conclude that the local structural information obtained by SPM can be generalized for the entire sample.

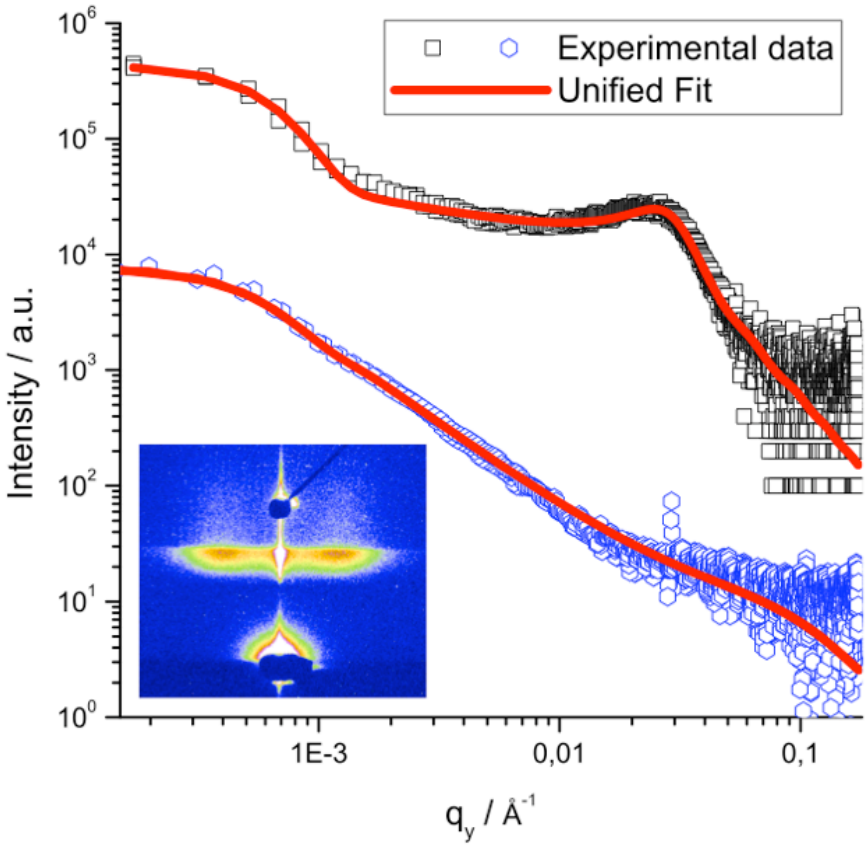

Figure 5.8: µ-GISAXS horizontal detector cuts of the PS-PMMA mixed polymer brush films after dichloromethane (bottom) and acidic acid (top) treatment. Hollow symbols represent the experimental data. Straight lines represent the Unified fit. The upper curve is shifted along the vertical axis for improved visualization. Inset shows the 2D-scattering image of the acetic acid treated film.

The morphology obtained after exposure to the selective solvent acetic acid is in good agreement with theoretical studies done by Müller et al. [41] Using Single-Chain-in-Mean-Field (SCMF) they predicted structures for different solvent qualities and brush compositions. In their calculations a dimple conformation is expected for mixed brushes exposed to a solvent, which is a good solvent for the polymer majority component in the film. As calculated by XRR the majority component of the prepared layer is PMMA (~ 65%), which has a good solubility in acetic acid. Lateral microphase-separation results in the formation of different domains, mainly depending on the brush composition. Highly asymmetric brushes form dimple like structures. The effect is amplified by the acetic acid, which causes the polystyrene to collapse and migrate to the substrate. After the collapse the dimples are covered by PMMA. From the center-to-center distance and the extracted radius of gyration, the average number of chain per domain can be estimated. As visible from the wide peak in the GISAXS scan, the domains have a broad size distribution. A single domain consists of roughly 40-70 single polymer chains. The broad size distribution is probably caused by the preparation method. Each step of the "grafting-to" process is a complete statistical process. A statistical distribution of the different polymer, and a large variance in dimple size is, therefore, anticipated. The large error in the center-to-center distance extracted from the line cuts of the SPM images is another evidence of this. Also the composition of the mixed brushes might play a role. Theoretical calculations predict a transition between dimples to ripple morphology for an increase in the minor component. Mixed morphology would lead to an increase in polydispersity and uncertainty in the radius of gyration. The fitted power law exponent of P = 2,4 is also another evidence of a mixed morphology, proposing an particle arrangement in an arbitrary three dimensional mass fractal.[98] The GISAXS image also reveals a lag of long-range order in case of the acetic acid treated film. As reported in the literature this is caused by fluctuations in the grafting point positions caused by the step by step preparation method.[43]

Theoretical SCMF calculations suggest that microphase separation is still present after the film has been exposed to a good solvent for both polymers. The NEXAFS

measurement suggests that both PMMA and PS are at the polymer-air interface. The previously collapsed PS chain swell due to the osmotic pressure, causing the polystyrene domains to rise to the surface. The SPM images show no contrast in phase mode. This is probably due to the small difference in elastic modulus between PS and PMMA. The horizontal GISAXS analysis also shows no structural peak at the incidence of $\alpha_i = 0{,}4°$. Above the critical angle of both PS and PMMA, the beam penetrates the whole film, giving raise to structural information of the whole film. Since each polymer chain is chemically bound to the substrate, microphase separation can only occur at the surface with a mixed PS/PMMA layer underneath it. Due to the low contrast in electron density between PMMA and PS, no peak is visible in the GISAXS image. In the SPM images no phase differences is visible due to the similarities in elastic modulus.

5.3.4 Stress

To obtain stress values, NMC bending experiment were conducted after treatment with dichloromethane and acetic acid respectively. Figure 5.9 displays the absolute surface stress values for PMMA-PS mixed polymer brush coated NMC, and the NMC only coated with one of the homopolymers. Both NMCs coated with homopolymer brushes as well as the one coated with mixed polymer brushes show a tensile stress upon the exposure to the selective solvent acetic acid. Bending experiments give information about forces acting laterally inside the polymer brush. For the homopolymer case, the tensile stress can, therefore, be attributed to attractive polymer-polymer interactions. These attractive forces are commonly attributed to interchain entanglements.[130, 131] For interchain entanglements to be present, the brushes have to be close enough with respect to the radius of gyration of an unperturbed polymer chain. From the calculated chain tethered densities of the homopolymer brushes of $\Sigma_{PMMA} = 3{,}44$/ $\Sigma_{PS} = 10{,}41$ one can see that the chains are close enough.

For the mixed polymer brushes much higher tensile stress was measured. Structural information suggests that for the acetic acid treated film microphase

separation is the reason for the increase in stress. As discussed earlier, the PS chains collapses and forms dimples close to the substrate surface. Multiple chains have to stretch and migrate to a common location. Since they are chemically bound to the surface, this happens under loss of entropy. Additional stress is induced through the PMMA covering the PS coil. To cover the coil, each chain has to stretch out of their natural configuration. This induces a tensile stress, i.e. the NMC bends towards the polymer layer.

After treatment with the good solvent DCM, the tensile stress in the NMC coated with the mixed brushes decreases. However, when compared to the homopolymer brush films it is higher. The NEXAFS measurement showed an increase in PS at the surface of the film. The measured tensile stress indicates that microphase separation is still present inside the mixed brush layer. This means that the PS and PMMA domains are still present in their previous composition. Treatment with dichloromethane causes the polystyrene to swell, increasing its surface coverage. At the same time, stress caused by PMMA bending over the PS is released. The additional surface stress in the acetic acid treated film is mainly a result of an increased stretching of the chains, caused by the collapse of the PS brushes and the forced reshaping of the PMMA brush domains.

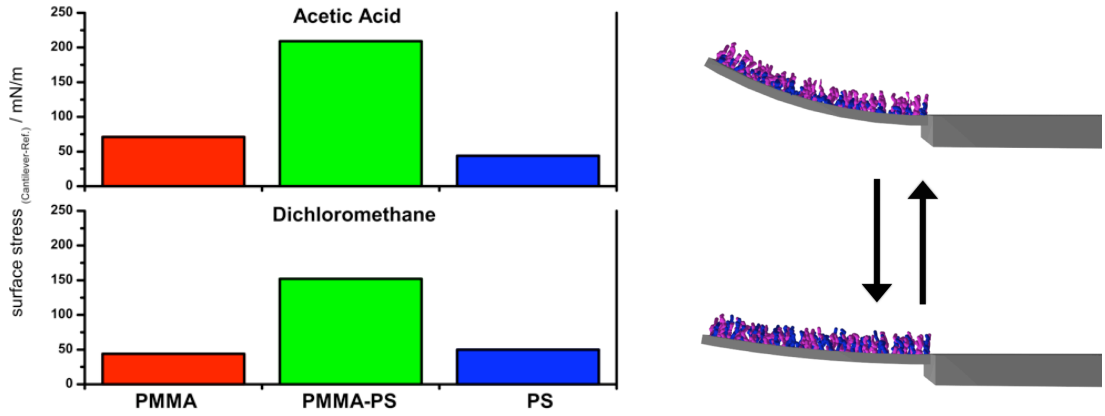

Figure 5.9: Absolute values of surface stress corrected by reference NMC and schematic representation of the measured absolute values.

In summary, the change in stress and structure can be described as followed (Figure 5.10). Microphase separation inside the mixed polymer brush film induces tensile stress in both acetic acid and dichloromethane treated films. Therefore, the required stretching of the chain induces a force causing the NMC to bend upwards. Treatment with acetic acid leads to a collapse of the polystyrene domains, therefore, the increased stretching of the PS and PMMA chains covering the polystyrene domains causes the increase in tensile stress.

With the results, the domain memory effect as reported by Santer et al. [38-40] can be explained. The fluctuations in local composition and grafting density results in domain formation at specific places. Since domain formation involves a high amount of stretching, PS and PMMA domains form most likely at relatively high local grafting densities of their respectively species, minimizing the amount of required stretching. As measured by the bending experiments, treatment with the good solvent dichloromethane changes the surface structure from a dimpled to a flat, but does not dissolve the domains itself. The flattening of the surface is due to the swelling of the polystyrene domain caused by the exposure to the good solvent. Treatment with acetic acid causes the polystyrene domain to collapse, leading to the reappearance of the dimple structure. Since no PS and PMMA domains are dissolved during the switching, the domains are formed at the same place and in the same size as before. The change in surface structure from flat to dimple structure is mainly caused by the collapsed and swelling of the polystyrene domains and the, therefore, necessary rearrangement of the surrounding PMMA. Even under optimal conditions only a surface reconstruction of <80% is reported. The incomplete reconstruction of the dimple structure is caused by difference in rearrangements of the PMMA domains after collapse of the PS domains. Partial reconstruction of energetic unfavorable domains in favor of a more stable conformation is also a possibility.

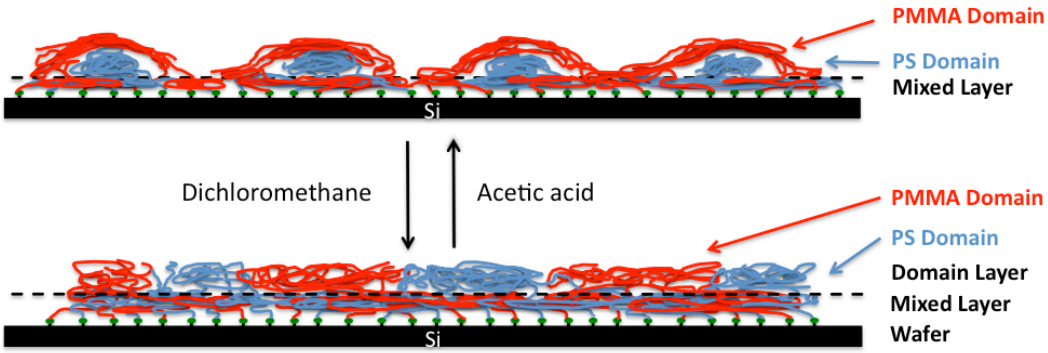

Figure 5.10: Schematic representation of the proposed structural change of the PMMA-PS mixed polymer brush film upon exposure to dichloromethane and acetic acid respectively. Upon exposure to acetic acid the polystyrene collapses to the surface and gets covered by PMMA in an attempt to maximize the favorable PMMA-PMMA contacts. Upon treatment with dichloromethane the PS micro domains swell.

5.4 Conclusion

The results show that microphase separation of the grafted polymer chains combined with the chemical fixation to the surfaces induces a large tensile stress when compared to the homopolymer case. Structural analysis of both, the acetic acid and dichloromethane treated film, concluded microphase separation, which is in good agreement with theoretical calculations. This allows one to explain the phenomenon of the domain memory effect. The change in structure is mainly caused by swelling and collapsing of the PS domains. Since the majority of the domains do not dissolve during the switching procedure, the structure is recovered.

The findings emphasize the importance of chain conformation and the resulting stress in thin polymer brush systems. Bending experiments conducted on nanomechanical NMC sensors are a useful tool to measure such stress. The utilization of phase shifting interferometry to obtain absolute stress values allows an even deeper understanding when compared to relative values.

6. Simultaneous investigation of NMCs by PSI and µ-X-rays

6.1 Introduction

For a comprehensive investigation of thin polymer film phenomena, the investigation of the correlation between stress and structure, as demonstrated in chapter 5, is a promising route. Usually, the structural investigation is done separately to the stress measurement on identical prepared silicon samples.[23] Therefore, the stress and structural changes and/or the sample preparation have to be highly repeatable. This represents an obstacle, limiting the amount of investigated systems.

For this reason a direct structural investigation of the coatings on top of NMCs is desirable. Due to the fragile nature and the small dimensions of NMCs this is not trivial. Scanning probe microscopy, for example, requires a solid support, making it useless for the investigation of coatings on top of flexible NMCs. X-ray scattering techniques, like XRR and GISAXS, do not require a solid support and provide averaged information of the investigated area. By using µ-focus options like the one available at the BW4 in Hamburg, small beam sizes in the dimensions of single NMCs are available. Wolkenhauer et al.[109] were the first to utilize µ-focus X-rays for the investigation of NMC sensors. By horizontally scanning across the sensors and investigating the yoneda peak position, they were able to distinguish between coated and uncoated areas of a partially gold-coated NMC array. They were also able to determine the thickness of the gold coating by recording XRR curves of single NMCs. Lenz et al.[22] introduced a special sample cell and demonstrated the ability to obtain even more structural information by recording GISAXS images of single polymer coated NMCs. This allows a comparison between changes in structure and separately measured changes in stress. However, simultaneous investigation of stress and structure remained inaccessible with the described setup.

In this work a setup for the simultaneous investigation of NMCs by phase shifting interferometry and µ-focused X-rays is presented. To do so, the PSI setup

introduced in Chapter 4 is implemented in the small angle X-ray scattering beamline BW4, HASYLAB, DESY. As a proof of principle, NMCs coated with gold and PMMA brushes are investigated.

6.2 Experimental

6.2.1 Sample preparation

The partial gold-coated NMC array was prepared by evaporation of 50 nm of gold using a mask.

The PMMA brush sample was prepared according to the "grafting-from" approach by Bumbu et al.[66]. To obtain uncoated NMCs as reference, the back as well as part of the top was masked by coating with Au. After immobilization of the starter on the unprotected surface, the polymerization was carried out in dry anisole with additional unbound-starter (2-EiBBr). After conclusion of the polymerization step, the gold was removed and excess polymer was extracted with dichloromethane. The free polymer had a molecular weight of M_n(GPC)= 117000 g/mol with a PDI(GPC) = 1,13.

6.2.2 Setup & alignment

In order to perform simultaneous measurements with the PSI as well as scattering experiments, the task is to simultaneously align the NMC sensors with respect to the interferometer beam path as well as to the synchrotron beam. To do so, the NMC array is placed in a special cell (Figure 6.2) which has a glass window for the laser beam and two Kapton® windows for the incoming and outgoing X-ray beam. Additionally, the sample cell has a gas inlet and outlet allowing measurements under inert gas as well as other gaseous atmospheres. A heating and cooling system enables measurements at different temperatures. The sample cell is mounted on an adjustable holder, which is attached to a rail system. This allows to focus the laser on the NMC by adjusting its height and also to remove any tilt.

The whole interferometer is mounted on a hexapod, which is placed on an additional z-stage. The hexapod enables one to align the NMC array with respect to the beam. Since the hexapod moves the whole PSI-setup, the position of the NMC array, with respect to the laser beam, is not altered during alignment or later measurements. For tilting and rotation of the NMC array, the hexapod allows one to set a pivot point freely in space. For precise rotation of the NMC array the pivot point should be set to the center position of the NMC array. To simplify the determination of these coordinates, the setup is constructed in a way that the NMC array is situated in the [0,0] x-y coordinates of the hexapod, making an alignment in these two coordinates obsolete. Hence, only the height z has to be determined for the pivot point utilizing the additional z-stage. To do so, the height of the hexapod itself and the NMC with respect to the synchrotron beam is determined. The needed z-coordinate of the pivot point is the difference between the two measured height values.

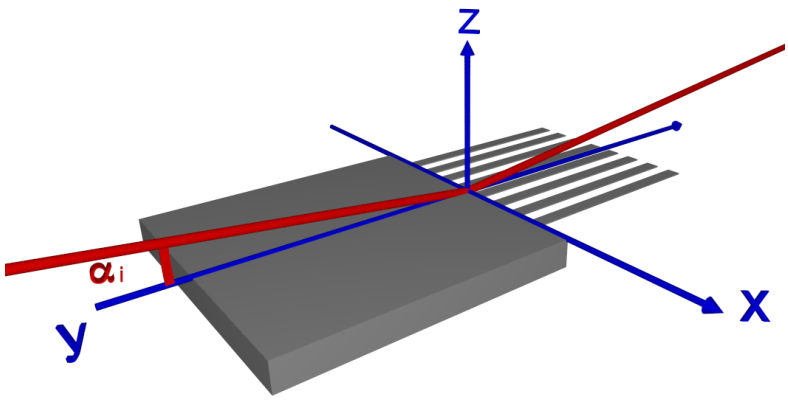

Figure 6.1: Schematic representation of the geometry for the investigation of NMCs by PSI and µ-focused X-rays.

For rough alignment of the NMC with respect to the synchrotron beam, standard rocking scans and scans in the z-direction are performed using the supporting chip of the NMC array as a reference. The position of each individual NMC is obtained by tilting the cantilever by 0,7° in the beam direction and conducting a scan in the x-direction. The intensity is recorded as a function of the x-direction. A profile of the NMC array is obtained, giving the position of each of the 8 NMCs (Figure 6.2D)

in the x-direction. By this means, also any tilt in the direction perpendicular to the beam is removed.

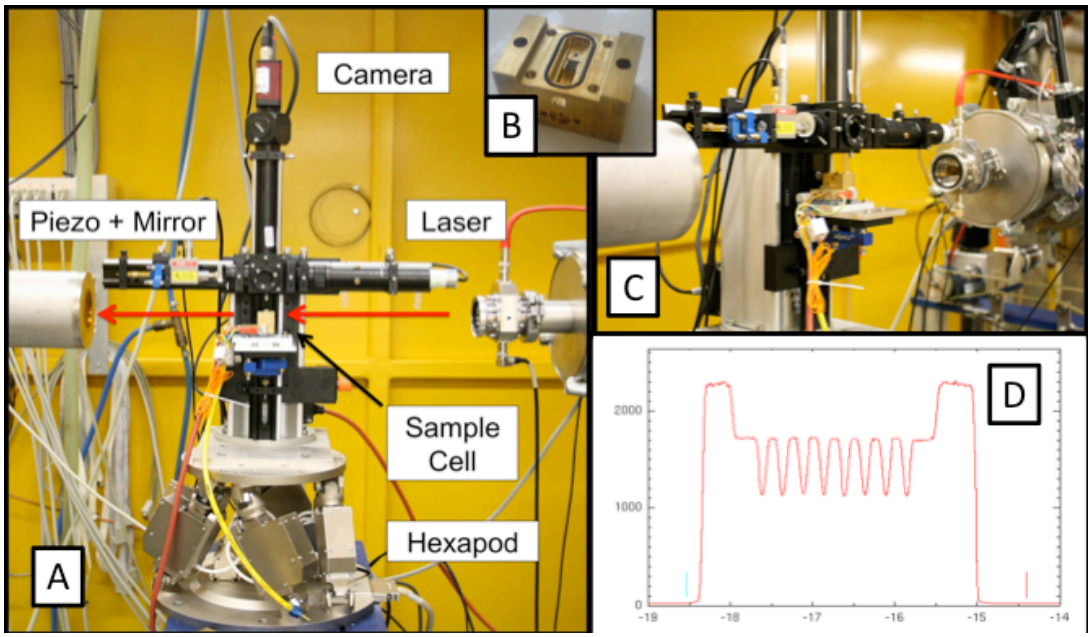

Figure 6.2: Image of the PSI mounted on the hexapod integrated in the µ-focus beamline BW4 (A,C). Close up image of the sample cell holding the NMC array. For better visibility the cover glass and Kapton® windows are removed. Profile obtained by scanning across the NMC array in the horizontal direction for the determination of the individual NMC position (D).

Since NMCs might be bend, precise determination of the incident angle is not trivial. The incident angle is, therefore, aligned using the specular and yoneda peak position on the detector.

For angle calibration a bare silicon wafer is placed on the setup in the same height and sample detector distance as the NMC. Multiple scattering images are recorded at different angles of incident (α_i = 0,4-0,8°). For each image the pixel position of the yoneda and specular peaks are determined and plotted against the angles of incident. A linear fit is performed for each set of data points. The position of the specular peak is a function of $2\alpha_i$. The yoneda peak is a function of $\alpha_i+\alpha_c$. The two lines should, therefore, intercept at $\alpha_i = \alpha_c$. The angle of the intercept is set to the critical angle of Si (α_c = 0,2°). For each desired angle of incident the adjusted

specular and yoneda peak position was calculated. Each NMC was then adjusted so that the specular and yoneda peak position fit these values.
NMCs have a length of 500-1000 µm in the beam direction. In dependence on the incident angle the beam has a footprint of 2600-4600 µm. To assure that only the NMC and not the chip is irradiated; the NMC is moved downwards by 500 µm at the end of the alignment. The loss in intensity is adjusted by increasing the measurement time.

6.2.3 Measurement

The sample cell was heated from room temperature to 50°C in steps of 10°C. X-ray reflectivity measurements were performed after each jump in temperature. At room temperature and at the final temperature of 50°C a GISAXS image was recorded. Throughout the X-ray measurements the curvature of the NMCs was recorded every 3 seconds.

6.3 Results & discussion

6.3.1 Curvature measurement

To analyze the bending experiments, the obtained NMC profiles were fitted along its whole length and the resulting curvature and surface stress was plotted against time.

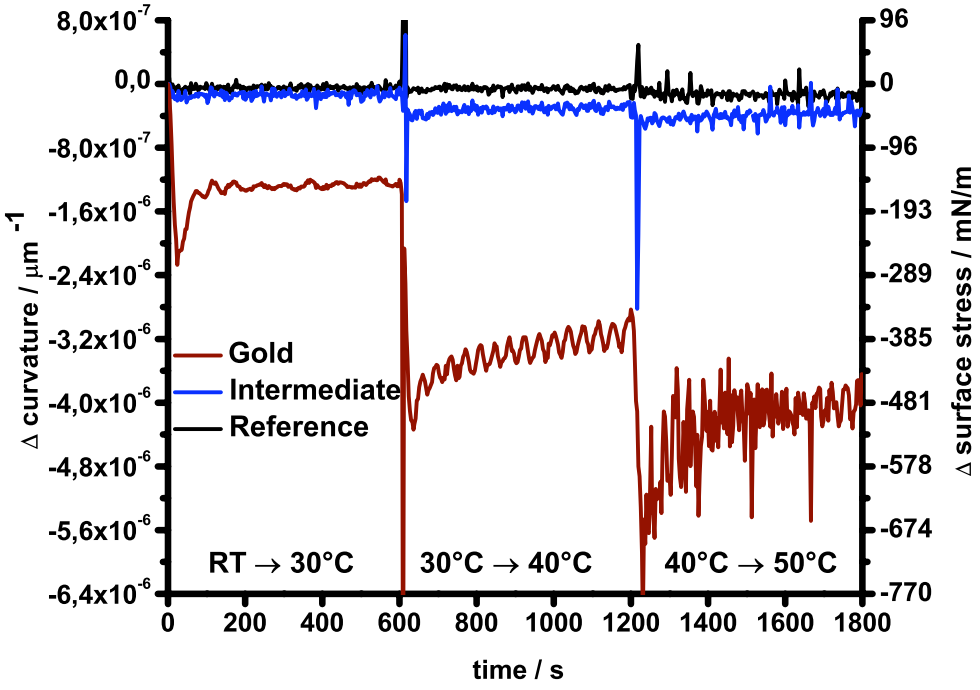

Figure 6.3: Change in curvature and surface stress values of the gold-coated NMC, partially coated NMC (intermediate) and reference plotted against time of the measurement simultaneously conducted with scattering experiments. The temperature was raised in steps of 10°C at 0, 600 and 1200 s respectively.

NMCs coated with gold show a decrease in curvature after every temperature jump (Figure 6.3). This is in good agreement with the previous measurement performed during the segmental investigations of NMCs in a laboratory environment (Chapter 4). Oscillations best visible after the temperature jump to 40°C are due to the temperature instability of the used heating device (± 1°C). The increased noise at T = 50°C is caused by increased convection of heat amplified by the small dimension

of the cell and the heater itself. This can also be seen in the otherwise stable values of the reference NMCs. The NMC labeled intermediate show a similar response like the gold-coated NMC with a smaller amplitude. If these changing curvature values are correlated against the values of the fully gold-coated NMC, one obtains $m_{Intermediate}$=0,09 and $R_{P;Intermediate}$=0,91. From the high linear correlation but low slope value one can conclude that the NMC is partial coated with gold.

NMCs coated with PMMA brushes also show a decrease in curvature, but much smaller when compared to the gold-coated NMCs (Figure 6.4). With increasing temperatures the same increase in noise, due to convection, is visible. Despite the noise the change in curvature as well as reference values can be detected. Measurements performed at room temperature yielded a standard deviation of $\Delta\kappa = 2{,}8 \times 10^{-8}$ μm^{-1}, an order of magnitude higher compared to measurements performed under normal laboratory conditions, where the PSI placed in an acoustic isolation box and on a vibration-isolated table. For a typical used 2 µm thick NMC this results in a $\Delta\sigma$ = 0,4 mN/m.

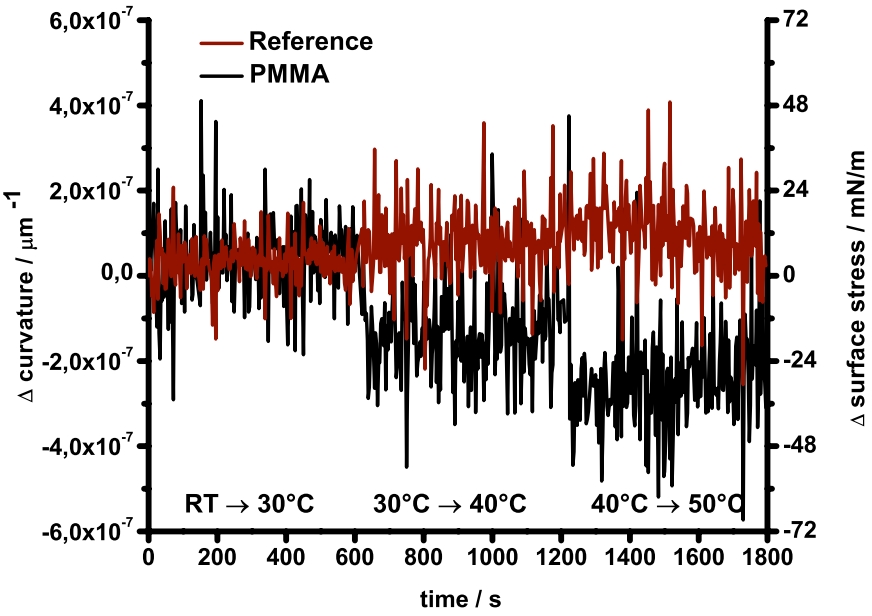

Figure 6.4: Resulting change in curvature and surface stress values of PMMA brush coated NMC sensor and reference plotted against time of the measurement simultaneously conducted with scattering experiments. The temperature was raised in steps of 10°C at 0, 600 and 1200 s respectively.

6.3.2 µ-XRR

For structural investigations of the coating on top of the NMCs XRR measurements were performed. Therefore, the 2D-XRR procedure was used to conduct measurements at RT and at 30°C, 40°C and 50°C. Due to the technical limitations of the used hexapod only measurements up to a q_z-value = 0,13 were possible.

The XRR curves obtained for the gold-coated NMC samples (Figure 6.5) show all expected characteristics. At low q_z values under total reflection one can observe a slightly decreasing reflectivity and a wide total reflection edge. This is due to the absorption of photons by the gold film. The film thicknesses calculated from the width of the oscillations were d_{RT} = 86,8±1,2 nm, $d_{30°C}$ = 86,9±1,2 nm, $d_{40°C}$ = 85,3±0,9 nm and $d_{50°C}$ = 86,5±1,3 nm. Compared to the expected film thickness of 50 nm, this seems to be a big discrepancy. The accuracy of the used approximation to estimate the film thickness depends on the roughness of the investigated film. The approximation is precise for perfectly flat interfaces. However, the investigated gold films typically have a high surface roughness. When one compare the data with a simulated XRR curves of a 60 nm gold film on silicon with a roughness of σ_{rms} = 2 nm, a high degree of similarity is visible.

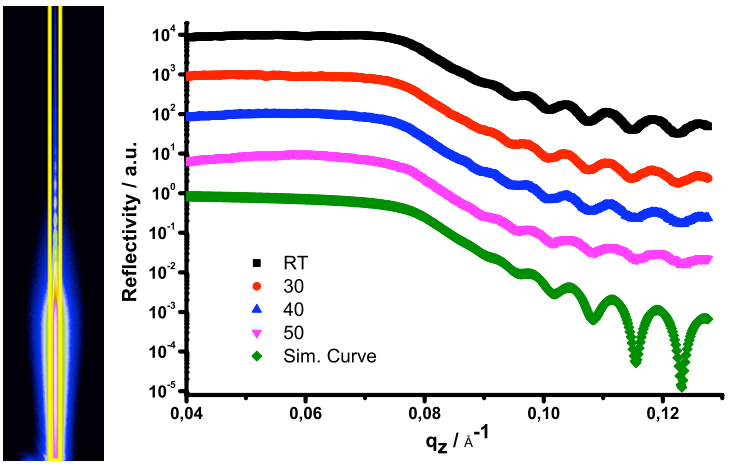

Figure 6.5: 2D-XRR image measured on a gold-coated NMC. XRR curves obtained from 2D images measured at different temperatures as well as simulated curve for a 60 nm thick gold film with σ_{rms} = 2. The curves are shifted in the y-direction for better visibility.

The XRR curves (Figure 6.6) obtained from the PMMA coated NMC also contain all characteristic features. At low q-values two edges can be observed, a small dip corresponding to the critical angle of the PMMA, and a sharp edge due to the critical angle of the silicon NMC. The film thicknesses calculated from the width of the oscillations was d_{RT} = 51,9±2,1 nm, $d_{30°C}$ = 51,3±2,9 nm, $d_{40°C}$ = 52,1±2,4 nm and $d_{50°C}$ = 51,5±2,9 nm. The data is best compared to a simulated curve with a film thickness of d = 46 nm and a roughness of σ_{rms} = 2 nm. This results in a grafting density of Γ = 0,32 chains/nm² and chain tethered density of Σ = 61. This is in good agreement with polymer brushes obtained on standard silicon wafer with similar molecular weights (Chapter 7).

In both cases the oscillations of the measurement seemed to be damped when compared to the simulations. This is due to the recorded diffuse scattering as well as the poor signal-to-noise ratio of the 2D-XRR setup.

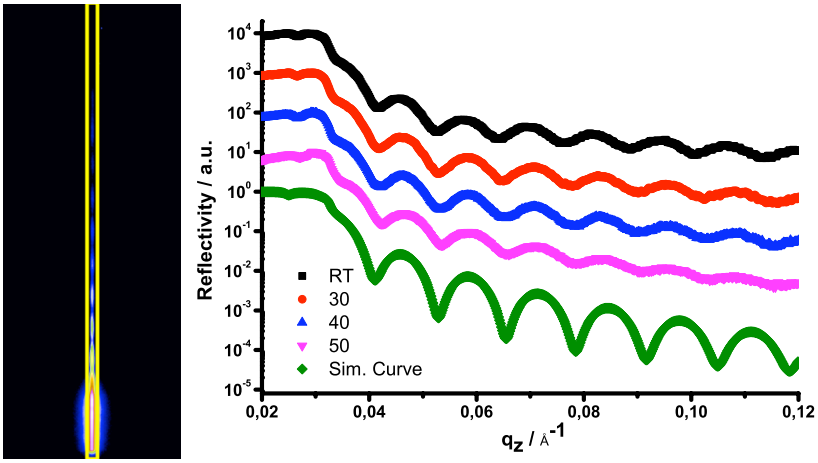

Figure 6.6: 2D-XRR image measured on a PMMA-coated NMC. XRR curves obtained from 2D-images measured at different temperatures as well as simulated curve for a 46 nm thick gold film with a σ_{rms} = 2. The curves are shifted in the y-direction for better visibility.

In summary, one can conclude that 2D-XRR measurements on top of single NMC with the presented setup are feasible. With the obtained XRR curves the film thickness can be determined. All obtained thicknesses at different temperatures are identical within the measuring error. Since no change in thickness was

expected, one can conclude that the elevated temperature have no effect on 2D-XRR measurements.

6.3.3 µ-GISAXS

In addition to the XRR measurement on top of the NMCs, GISAXS measurements were performed. The obtained 2D-images show all characteristic features. The NMC coated with PMMA brushes shows a specular peak (shielded by beamstop), a yoneda peak and additional modulation in intensity. This is evident for a correlated interface typical for "grafted-from" polymer brushes (Chapter 7). The 2D images obtained from measurement of the gold-coated NMC shows a yoneda peak as well as a specular reflected peak (shielded by beamstop). While the specular peak has not shifted in q_z, the yoneda peak has shifted to higher q_z-values. This is caused by the higher electron density in the gold film resulting in a higher critical angle compared to the PMMA brush coated NMC.

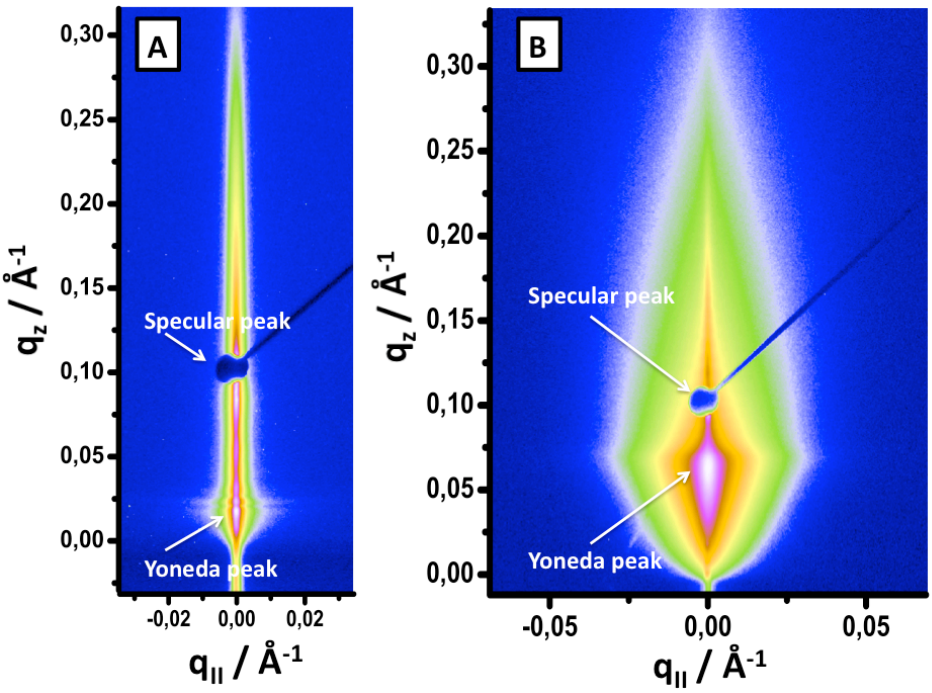

Figure 6.7: 2D-GISAXS images obtained from PMMA brush (A) and gold (B) coated NMCs during simultaneous curvature measurements.

6.4 Conclusion

In summary, one can conclude that the developed setup allows one to perform X-ray reflectivity and gracing incidence small angle X-ray scattering measurement on single NMCs, while obtaining curvature values. Changes in stress can, therefore, directly be correlated to changes in structure (thickness, lateral domain sizes, etc.). The increased noise compared to in-lab measurements might be resolved by a special acoustic-isolation box mounted around the hexapod and the PSI setup. Two Kapton windows at the side of the box allow an incoming and outgoing X-ray beam. The box would also isolate the cell from the environment, thereby reducing the convection of heat and vibration. This would reduce the noise and allow measurement with higher resolutions and higher temperatures.

The use of a different hexapod with adjustable movement speed would allow to adjust the incoming intensity and measurement time per "data point". Thereby yielding measurements in a larger q_z-range and lower background, allowing one to directly fit the XRR curves and thus supplying roughness and electron density data.

7. Roughness correlation in PMMA brushes

7.1 Introduction

In the development of µ-focused scattering on NMC sensors, Nett[132] investigated NMCs coated with PMMA polymer brushes. The brushes were obtained by a "grafting-from" approach as described by Bumbu et al.[66] In the investigation XRR curves as well as 2D-GISAXS images were recorded. When detector-cuts were performed in order to investigate the polymer brushes in the vertical direction, the graphs showed the characteristic yoneda and specular peak. However, the curves had additional oscillations of intensity. When compared to the measured film thickness d, they found

$$d = \frac{2\pi}{\Delta q} \tag{31}$$

with Δq being the distance between two oscillation minima. This is caused by roughness correlation. As described in chapter 2.5.6, roughness correlation is the transfer of a roughness profile from an interface to an adjacent. The scattering of the two interfaces is, therefore, no longer independent, causing interferences, which result in the observed oscillation of the intensity.

In untethered polymer films roughness correlation is a known phenomena.[133-137] Müller-Buschbaum et al.[133] investigated spin-coated polystyrene on silicon wafer and found roughness correlation. They attributed the effect to the liquid like behavior of the polymer film during the preparation process. When they heated the polymer film above T_g, the oscillations disappeared. Therefore, they concluded that the phenomenon was a result of the preparation process and not present in equilibrium. The investigated PMMA brushes on NMCs were treated with a good solvent, DCM, as well as thermally annealed before measurement. The PMMA brushes should be in equilibrium and should not show roughness correlation if the untethered case is took as comparison.

For freestanding polymer films Shin et al.[138] observed that only film with a thickness of around 2 R_g showed roughness correlation. In the literature only one investigation on the phenomena using polymer brushes can be found.[139] Akgun et al. investigated diblock copolymer brushes and found that roughness correlation is present. Even after heating the sample above its glass transition temperatures the roughness correlation did not disappear.[139] The questions whether or not this is also valid for homopolymer brushes remained unanswered. No investigation of the effect of grafting density and molecular weight of the polymer brushes was performed. Therefore, there is no explanation of the observed phenomena.

Interfacial roughness is an important characteristic in thin polymer film applications, e.g. polymer electronics. Because of the fact that typically nm-thick polymer films are used, large interfacial roughness causes a large deviation in local film thicknesses. However, to obtain a constant quality, for example, across an entire organic light emitting diode, not only a certain average but also a constant local film thickness is desired.[140, 141] The interfacial roughness is typically determined by XRR. In the case of roughness correlation, not only specular reflected intensity but also a large amount of diffuse scattered intensity is recorded. This causes an apparent increase in reflectivity and will result in incorrect roughness values if not accounted for in the analysis.[94]

Recently Emmerling et al. demonstrated a convenient method to tune the grafting density of polymer brush films.[142] By treating an ATRP starter layer with acetic acid for varying amount of time, different starter concentration on the surface can be obtained. Consecutively "grafting-from" polymerization results in polymer film with different grafting densities and polymer chains with a narrow molecular weight distribution. By synthesizing an ATRP starter with a tertiary and a primary ester bond they were able to produce a wide variety of grafting densities.

When the roughness correlation is caused by the brush nature of the film, it should be possible to investigate the phenomena by investigating films with different chain tethered density. To do so, the method describe by Emmerling et al. to obtain multiple samples with thin PMMA brush films on silicon wafers with different molecular weight polymers is used. Each sample possesses segments varying in grafting density of the "grafted-from" polymer chains. The sample segments were

investigated by XRR and GISAXS, allowing one to directly assign the roughness correlation to the chain tethered density of the investigated segment.

7.2 Experimental

7.2.1 Gradient polymer brush sample preparation

The gradient polymer brush samples were prepared according to the procedure described by Emmerling et al.[142] As samples silicon wafers (3 cm x 2,6 cm) were functionalized with ATRP starter. All samples but one were functionalized with an ATRP starter containing a primary ester bond. For the sample with 101600 g/mol an ATRP starter was used containing a tertiary ester bond. The ATRP starter were immobilized by placing the wafer in a dry solution of toluene, triethylamine and the ATRP starter and stirred for 20 h. Consecutively, the wafer was washed with Milli-Q water and the excess reactants were extracted with dichloromethane over night.

To obtain a gradient in grafting density, the functionalized wafers were vertically dipped into 1 M acetic acid using a dip-coating device. Then the wafer was pulled out of the solution in steps of 0,5 cm. A wafer contained 6 regions with different amount of active starter molecules. Overall the investigated areas of the samples were exposed to acetic acid from 5 min up to 60 min. Afterwards, the polymerization was performed by placing the wafer in a mixture of anisole (1 eq.), MMA (1 eq.), CuBr (0,01 eq.), PMDETA (0,01 eq.) and additional unbound initiator 2-EiBBr (0,01 eq.) under oxygen free conditions. The molecular weight was determined by GPC of the additionally obtained free polymer.

7.2.2 µ-GISAXS & µ-XRR

To define the position of each investigated segment of a given sample, the sample was placed on the GISAXS stage so that the grafting density gradient was horizontal to the incoming beam (Figure 7.1). After sample alignment, the sample

edge was determined by scanning the sample in the x-direction. The first segment was measured 0,25 cm away from the samples edge, and subsequent segments were measured after moving the sample by 0,5 cm in x-direction after each measurement.

At each position a 2D-XRR curve was obtained. The film thickness was determined by measuring the distance between to oscillation minima and formula (21). The resulting grafting densities and chain tethered densities were calculated by formula (2) and (3) respectively.

The GISAXS measurements were performed with a sample-detector distance of 2 m. The angle of incidence was set to α_i = 0,7°, except for samples with molecular weight of M_n = 78000 g/mol and M_n = 101600 g/mol which were measured at α_i = 1°. Increasing the incident angle results in a larger separation of yoneda and specular peak. Since the width of the modulation is inversely proportional to the film thickness, this allows for an easier detection of the modulation. Both values are well above the critical angle of the polymer brushes. Therefore, the beam penetrates the entire sample, giving rise to information of both interfaces and potential correlations. To be able to directly link the GISAXS data to the measured film thickness, the measurements were performed at the same location as the XRR measurements. To evaluate the GISAXS image, so called "detector-cuts" were performed. To do so, seven pixels were summed up along the q_z-direction in order to obtain a 1D-plot. Each 2D-image was typically recorded for 60 min.

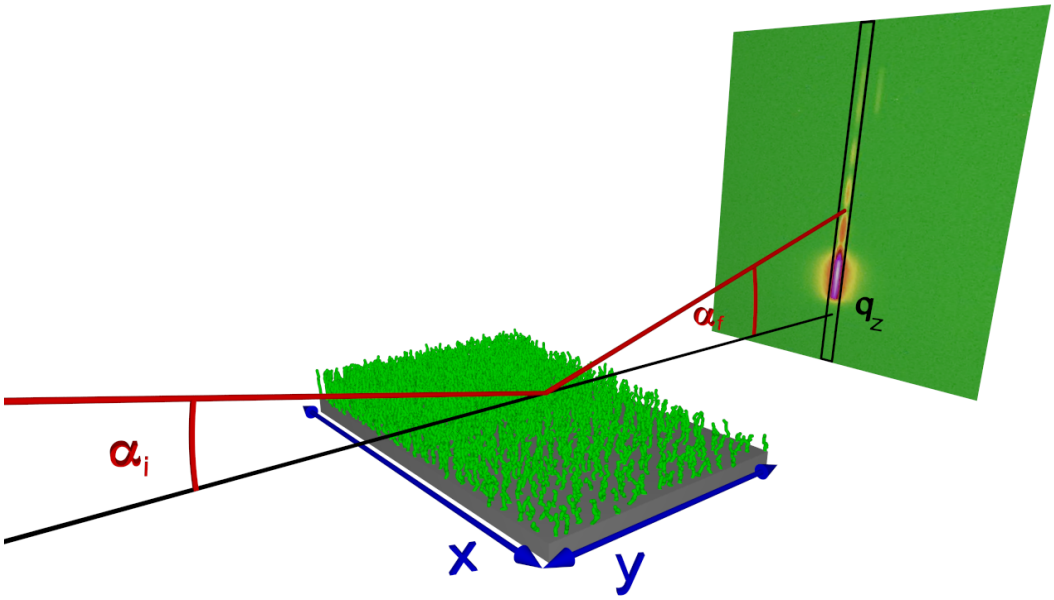

Figure 7.1: 2D-XRR geometry for the investigation of the gradient polymer samples.

7.3 Results & discussion

7.3.1 Gradient samples

First, the obtained film thicknesses are investigated. When the film thickness for each sample segment is plotted against the exposure time (Figure 7.2), the expected decrease in film thickness with increasing exposure time can be observed. When comparing different molecular weight samples, an increase in absolute slope values with increasing molecular weight can be observed. This increase is in good agreement with the assumption that the molecular weight of the polymer brush stays constant across a sample and the decrease in film thickness is due to the decrease in grafting density. The sample with M_n = 101600 g/mol resulted in much lower film thickness compared to the other films with similar exposition time. This corresponds very well with the higher cleavability of the tertiary ester compared to the primary one.

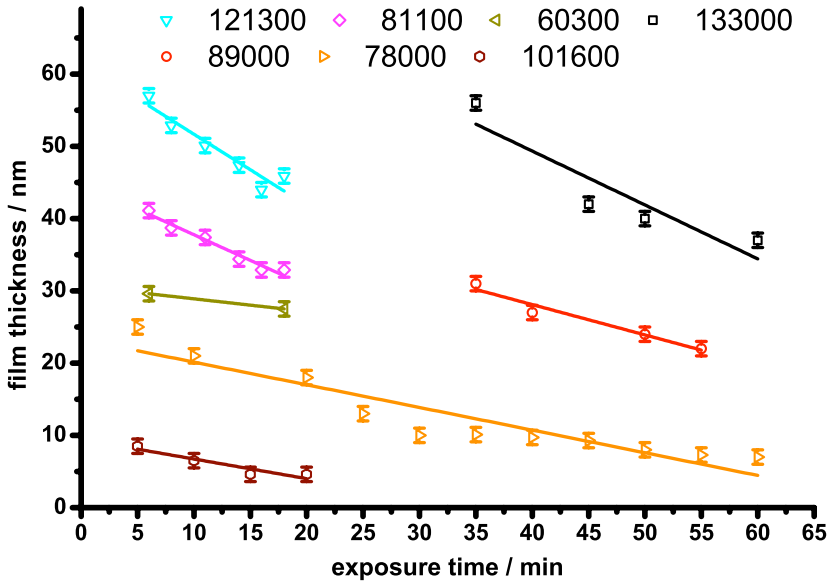

Figure 7.2: Resulting film thickness vs. exposure time of the starter layer to acetic acid.

One can conclude that the used procedure provides polymer films bearing segments with different grafting densities but same molecular weight polymer brushes (Figure 7.3). In summary, polymer brush films with grafting densities from Γ = 0,03-0,35 chain/nm^2, M_n = 60300-133000 g/mol were obtained. This resulted in chain tethered densities of Σ = 5-67.

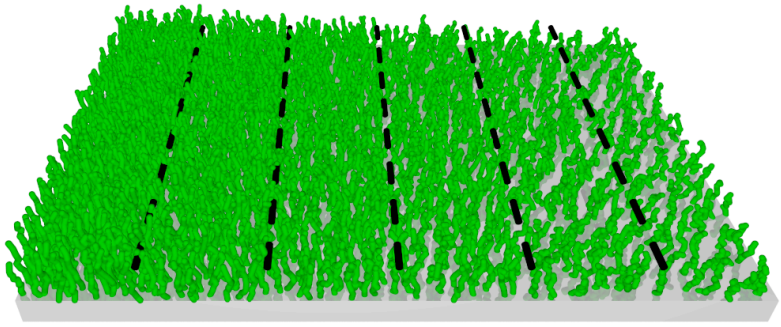

Figure 7.3: Schematic illustration of a sample with polymer brushes of the same molecular weight but regions of different grafting densities.

7.3.2 Roughness correlation

In order to investigate roughness correlation, the obtained detectors cuts were analyzed. In Figure 7.4A a detector cut obtained from an as-prepared sample with M_n = 121300 g/mol polymer brushes is displayed. The curves from three different segments show the typical yoneda peak maximum as well as additional oscillations. The oscillations show the film thickness dependence, characteristic for roughness correlation (formula 31). One can, therefore, conclude that the two interfaces of the as-prepared polymer brush film are indeed correlated.

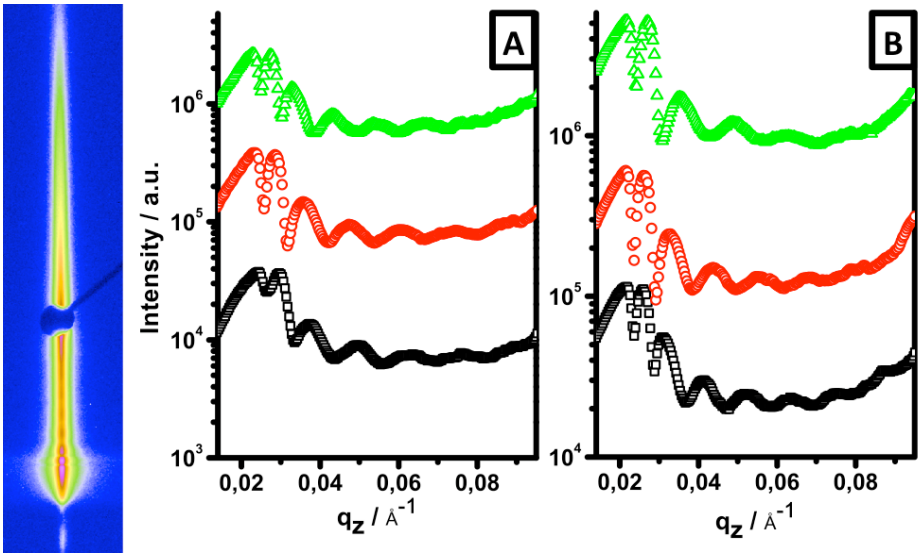

Figure 7.4: Typical 2D-image obtained from PMMA brush coated silicon wafer. Off detector cut obtained from 2D-images before (A) and after (B) thermal annealing.

To investigate, if the roughness correlation is caused by the preparation method, the film was heated to 180°C for 72 h, and slowly cooled down to room temperature. The temperature is well above the glass transition temperature of the PMMA (T_g = 105°C), and the polymer brush film is, therefore, in its thermodynamic equilibrium. Subsequent GISAXS measurements (Figure 7.4B) were performed in the same segments as in Figure 7.4A. The resulted curve showed the same features, yoneda peak and oscillations, as the unannealed

sample. Therefore one can conclude that roughness correlation is an intrinsic property of polymer brushes.

Compared to the untethered case of a spin-coated polymer film, a polymer brush has two distinctions. First of all, the tethering of each polymer chain to the substrate, and the second, being the stretching forced by the close proximity of neighboring chains. The question is whether the tethering itself or the stretching of the chains is the cause for the roughness replication. In other words, is roughness correlation an intrinsic property of a true polymer brush or of all tethered polymer films, like the so-called mushroom?

For further investigations, multiple samples, each sample featured segment with different grafting densities and differed in molecular weight of the "grafted-from" polymer chains, were investigated. To compare the obtained measurement, the lateral cutoff length R_c was determined.[143] In polymer films not all lateral structure sizes of the roughness spectrum are transferred to the overlaying interface. R_c is the smallest lateral structure size replicated by the overlaying interface[133]. To determine R_c, the decay of the modulations is investigated as a function of q_y.

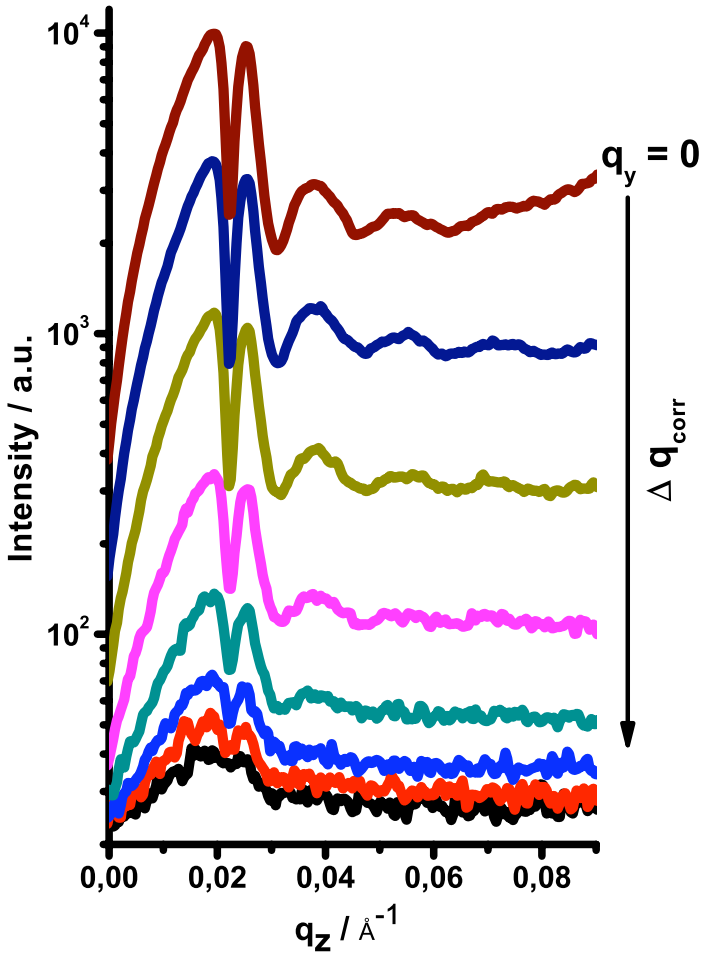

Figure 7.5: Typical plot used for the determination of Δq_{corr} necessary for the calculation of R_c.

To do so, vertical cuts parallel to the detector cut are performed. As can be seen in Figure 7.5, the intensity of the modulations decreases with increasing q_y. Δq_{corr} is defined as the lateral propagation length of these modulations. The resulting lateral cutoff length can be calculated as follows:

$$R_c = \frac{2\pi}{\Delta q_{corr}} \qquad \textbf{(32)}$$

In order to compare different molecular weight samples, the calculated lateral cutoff length R_c was normalized by 2 times the radius of gyration. To express the brush nature of each measurement sample segment, the resulting $R_c/2R_g$ was plotted against the chain tethered density Σ (Figure 7.6). The complete data set can be found in the appendix 3.

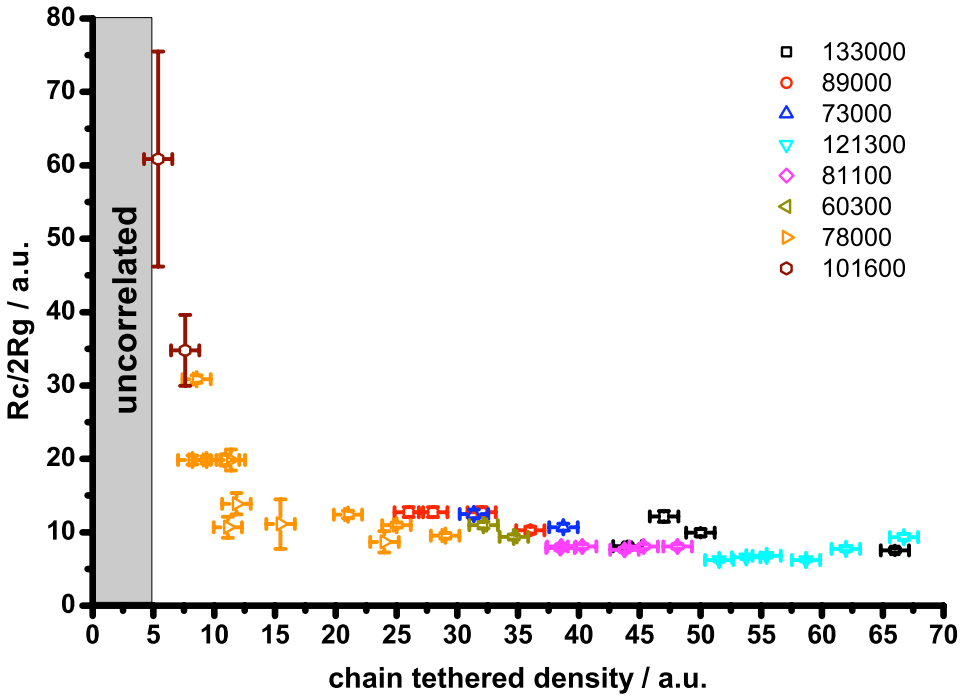

Figure 7.6: Rc/2Rg plotted against chain tethered density.

For $\Sigma > 15$ the resulting $R_c/2R_g$ is roughly equal to 10. This is comparable to values obtained for spin-coated, unannealed polymer films.[133] Having that in mind, one can conclude that for $\Sigma > 15$ the lateral cutoff length is influenced by the stiffness of the polymer, making it comparable to the untethered case. For values $\Sigma < 15$ the $R_c/2R_g$ steeply increases to values of up $R_c/2R_g = 61$ for $\Sigma = 8$. With decreasing chain tethered density each polymer chain has a larger area on top of the surface, decreasing the required stretching of each chain. During annealing above T_g, each chain has an increase in degrees of freedom allowing the chains to move closer to their untethered equilibrium state. For $\Sigma < 5$ no modulation is visible in the detector-cuts (Figure 7.7). In this case, the effect of the neighboring chains is so weak that the air/polymer interface roughness is dominated by the minimization of free energy, just like in the untethered case. When compared to the categorization of polymer brushes by Brittain and Minko[24], one can conclude that the observed roughness correlation agrees with the proposed chain states.

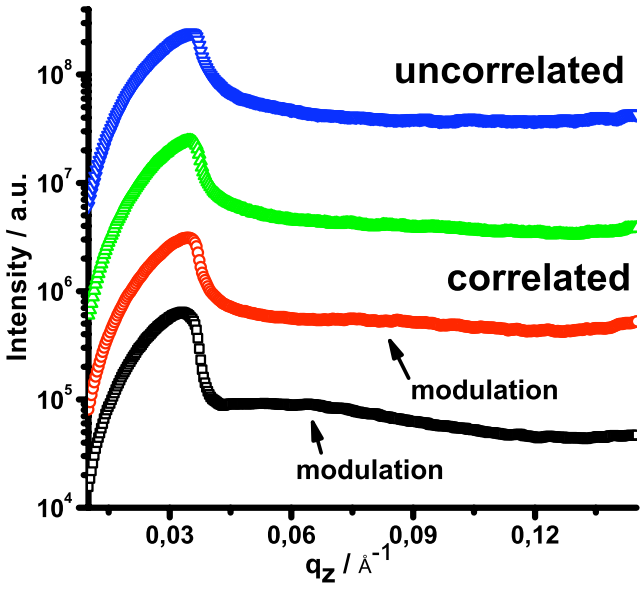

Figure 7.7: Detector cuts obtained from four different segments of a sample with molecular weight of M_n = 101600 g/mol. The bottom two curves show a modulation while the upper two curves show no modulation. The curves are shifted in the y-direction for better visibility.

7.4 Conclusion

In summary, one can conclude that roughness correlation is an intrinsic property of polymer brushes with $\Sigma > 5$. The two interfaces can, therefore, not be seen as independent. In the analysis of scattering data this correlation has to be considered. From the observed disappearance of roughness correlation at the brush-mushroom transition one can conclude that the phenomena is caused by the steric hindrance due to the limited space available for each brush.

Summary & outlook

By using a pentafluorophenol-functionalized RAFT agent, end-functionalized PS and PMMA were synthesized. By a "grafting-to" approach mixed polymer as well as homopolymer brushes were obtained. By utilizing inkjet printing the presented method also enabled one to partial coat NMCs for segmental analysis. The approach shows an elegant way to a multitude of other homo and mixed polymer brushes, especially methacrylate derivatives.

The efforts in improving the readout of NMCs presented a way to simplify NMC sensing. The assembled phase shifting interferometer along with the developed software enables even inexperienced user to obtained absolute curvature values. Performing multiple curvatures on a single NMC increases the output, while the segmental analysis shows an elegant path to handle the necessary determination of segment position. The concept also shows an innovative pathway for further advancement. Segmental analysis might also be used to detect a gradient, e.g. concentration, along the length of a NMC. When included into a microfluidic device, a suitable homogenously coated NMC should allow one to measure a concentration gradient, for example, generated by two reacting fluids. This might present a cheap alternative to the presently used techniques.[144]

The performed stress-structure correlation in the investigation of mixed polymer brushes deepened the understanding of the inner structure of mixed polymer brushes, allowing one to explain the observed domain memory effect. The study underlined the usefulness of stress data. In further investigations, polymer brushes with different composition might be studied. Stress and structure data might give a deeper inside into the dimple and ripple morphologies.

Integration of the PSI setup into the μ-focus scattering beamline BW4 demonstrated a way to simultaneously obtain stress and structure data for a direct correlation. Without major adjustment, the presented setup could be implemented in the new scattering beamline MINAXS at PETRA 3[145]. The beamline offers similar beam sizes, suitable for scattering measurement on single NMC sensors. The

increased photon flux and suitable detectors enable one to record multiple GISAXS images per second. This allows the investigation of dynamic processes, recently demonstrated in the study of cluster formation.[145]

With the help of the presented setup irreversible processes, for example melting of colloids[93], could be investigated. GISAXS studies over time would enable one to directly correlate size and shape of the colloids to the force applied on to the NMC.

Investigation of the roughness correlation in PMMA brushes confirmed the intrinsic nature of the effect. The study of different chain tethered densities allowed a direct correlation to the steric hindrance due to the limited space available for each brush.

In further investigation, the effect of treatment with different solvents could be investigated. Treatment of the polymer with a non-solvent would cause the polymer chains to collapse to the surface. Depending on the solvent quality a change in the absolute values of $R_c/2R_g$ as well as a disappearance of the roughness at higher Σ values should be measured. From the obtained data further conclusion on chain conformations could be drawn. Furthermore the effect of the molecular weight distributions could be investigated. Different length of polymer chains should result in overlapping of the polymer chains at the surface. This should result in a disappearance of the roughness correlation and would show a convenient pathway to avoid the roughness correlation while conserving the advantages of polymer brushes. The question whether there is an upper limit in Σ or not is also in question. A disappearance of roughness correlation at higher Σ, mainly achieved by higher molecular weight polymers, would be a strong hind for a vertical overlap of the polymer chains.

The samples could also be used to investigate the observed phenomena of increased wear resistivity of polymer brushes compared to untethered polymer films. By this means, the questions whether the proximity of the chains increases wear stability could be answered.[3]

Appendix

1. Scattering length densities

Scattering Length Densities used as starting values for the fit of the XRR curves (Chapter 3.2.4 & 5.3.1) with the software Parrat32. The scattering densities were calculated with scattering length density calculator available online[97].

Compound	**δ/g/cm³**	**SLD (real)/10⁻⁶ Å⁻²**	**SLD (imag)/i10⁻⁸ Å⁻²**
Si	2,34	20,1	46,7
APDES	1	9,42	5,45
PMMA	1,19	10,9	2,20
PS	1,05	9,60	1,23
PMMA/PS	1,1	10,1	1,95

2. Simplifying nanomechanical cantilever sensors

Curvature vs. curvature plots with resulting fit data for the correlation of changing curvature values in chapter 4.

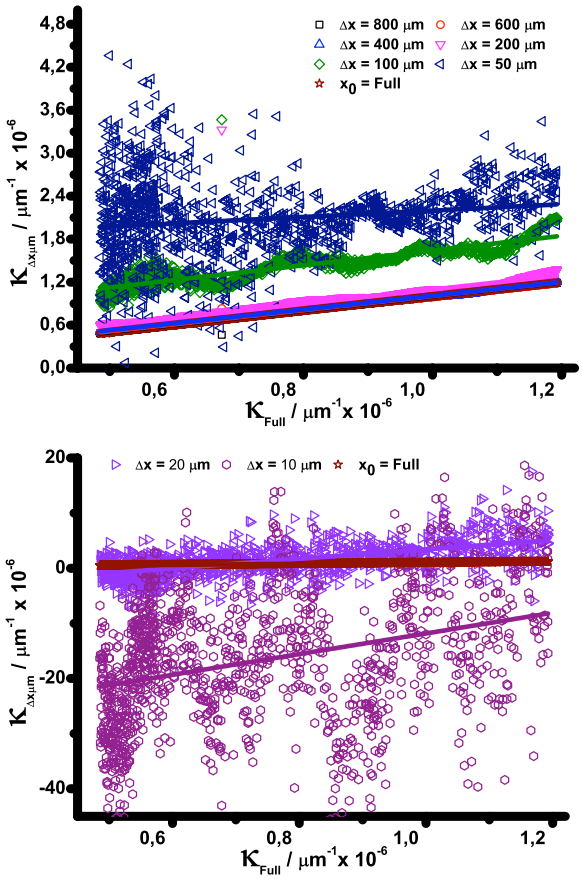

Figure A. 1: Au coated NMC Δx-investigation (Chapter 4.3.2).

Δx	m / a.u	b/ µm^{-1}	R_P /a.u
800	0,99	4,35× 10^{-10}	0,99
600	0,99	1,63× 10^{-9}	0,99
400	0,96	-7,04× 10^{-9}	0,99

200	0,99	$-4{,}6\times 10^{-8}$	0,88
100	1,03	$-1{,}13\times 10^{-7}$	0,76
50	0,45	$-2{,}13\times 10^{-7}$	0,03
30	8,59	$3{,}43\times 10^{-7}$	0,37
10	18,75	$-5{,}64\times 10^{-6}$	0,11

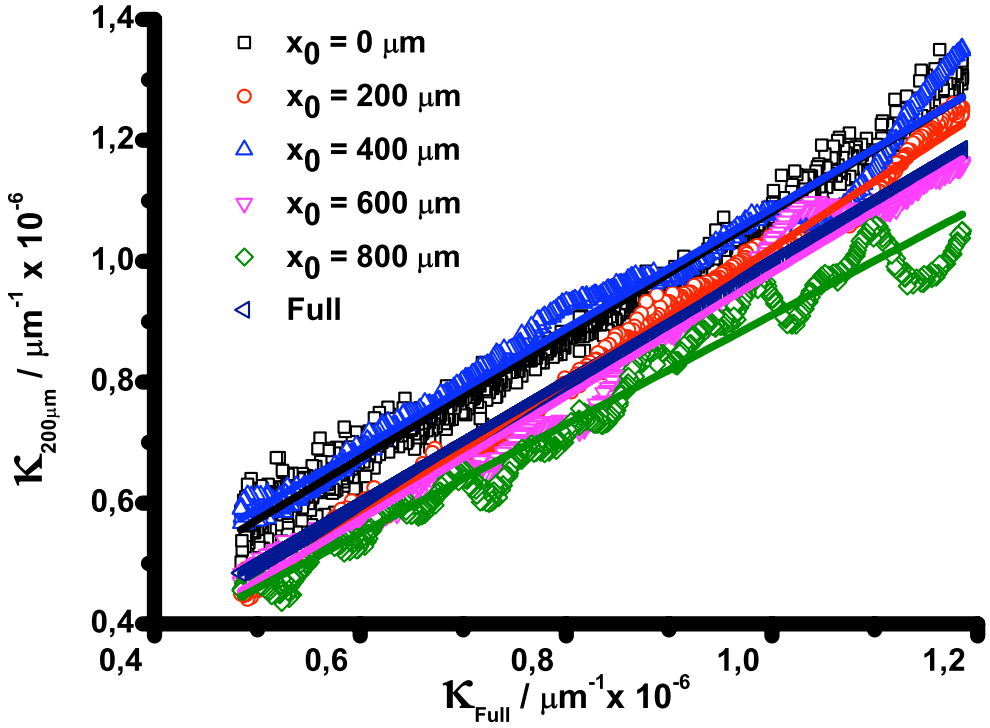

Figure A. 2: Au coated NMC (Δx = 200µm) x_0-investigation (Chapter 4.3.2).

x_0	m / a.u	b/ μm^{-1}	R_P /a.u
0	1,02	$3{,}10\times 10^{-8}$	0,99
200	1,11	$-4{,}40\times 10^{-8}$	0,99
400	0,99	$4{,}66\times 10^{-8}$	0,98
600	1,02	$-1{,}93\times 10^{-8}$	0,98
800	0,90	$4{,}13\times 10^{-8}$	0,98

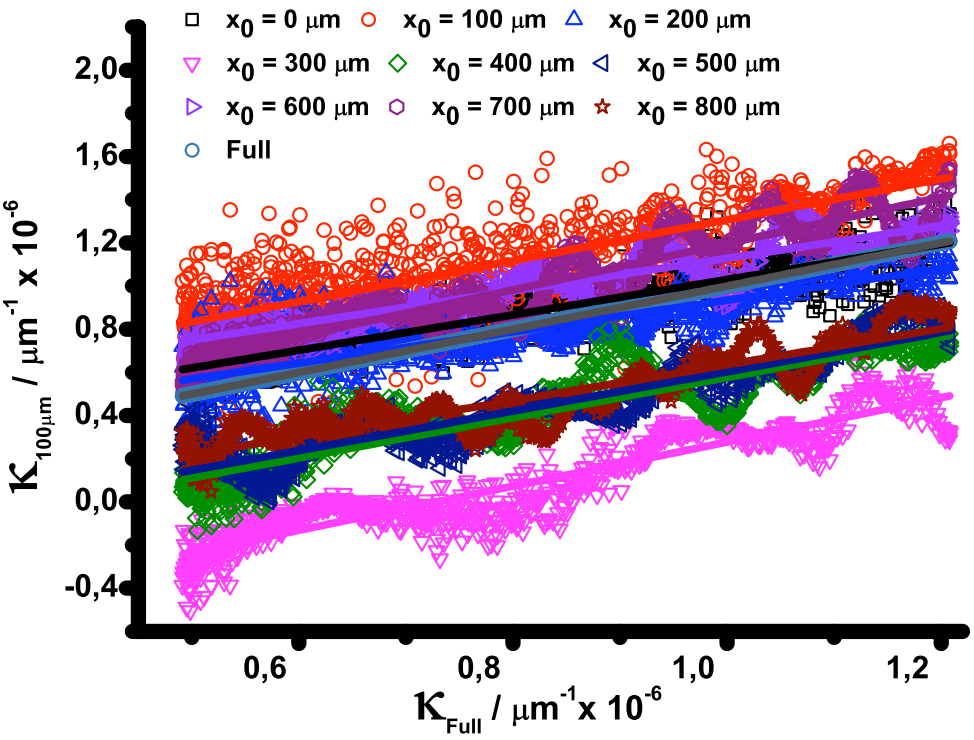

Figure A. 3: Au coated NMC (Δx = 100µm) x_0-investigation (Chapter 4.3.2).

x_0	m / a.u	b/ µm^{-1}	R_P /a.u
0	0,80	1,06× 10^{-7}	0,83
100	0,95	1,79× 10^{-7}	0,67
200	0,73	1,03× 10^{-7}	0,70
300	1,02	-3,73× 10^{-7}	0,86
400	0,93	-1,77× 10^{-7}	0,81
500	0,91	-1,55× 10^{-7}	0,85
600	0,76	1,86× 10^{-7}	0,86
700	1,07	6,22× 10^{-8}	0,88
800	0,83	-9,84× 10^{-8}	0,83

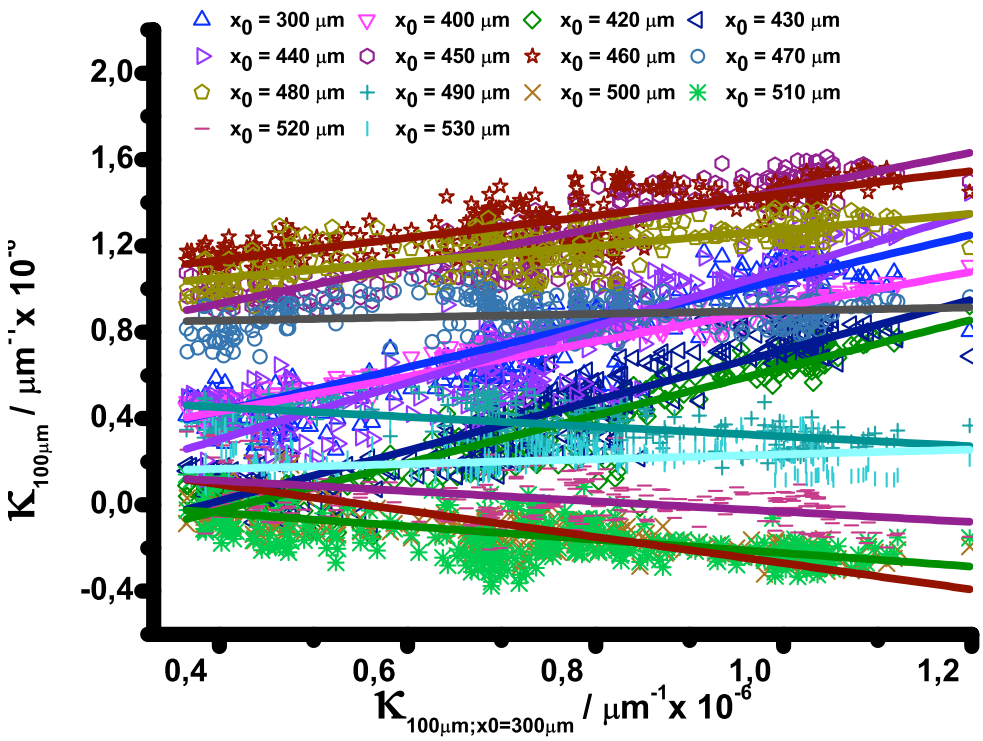

Figure A. 4: Partially Au coated NMC (Δx = 100µm) x_0-investigation; determination of segment position NMC1 (Chapter 4.3.3).

,

x_0	m / a.u	b/ μm^{-1}	R_P /a.u
400	0,81	$5,45\times 10^{-8}$	0,31
420	1,10	$-2,34\times 10^{-7}$	0,93
430	1,16	$-2,23\times 10^{-7}$	0,91
440	1,31	$-1,09\times 10^{-7}$	0,90
450	0,88	$2,91\times 10^{-7}$	0,89
460	0,52	$4,64\times 10^{-7}$	0,80
470	0,37	$4,51\times 10^{-7}$	0,70
480	0,08	$4,12\times 10^{-7}$	0,21
490	-0,23	$2,71\times 10^{-7}$	-0,54

500	-0,31	4,38× 10^{-8}	-0,72
510	-0,61	1,69× 10^{-7}	-0,22
520	-0,24	1,04× 10^{-7}	-0,43
530	0,11	6,13× 10^{-8}	0,01

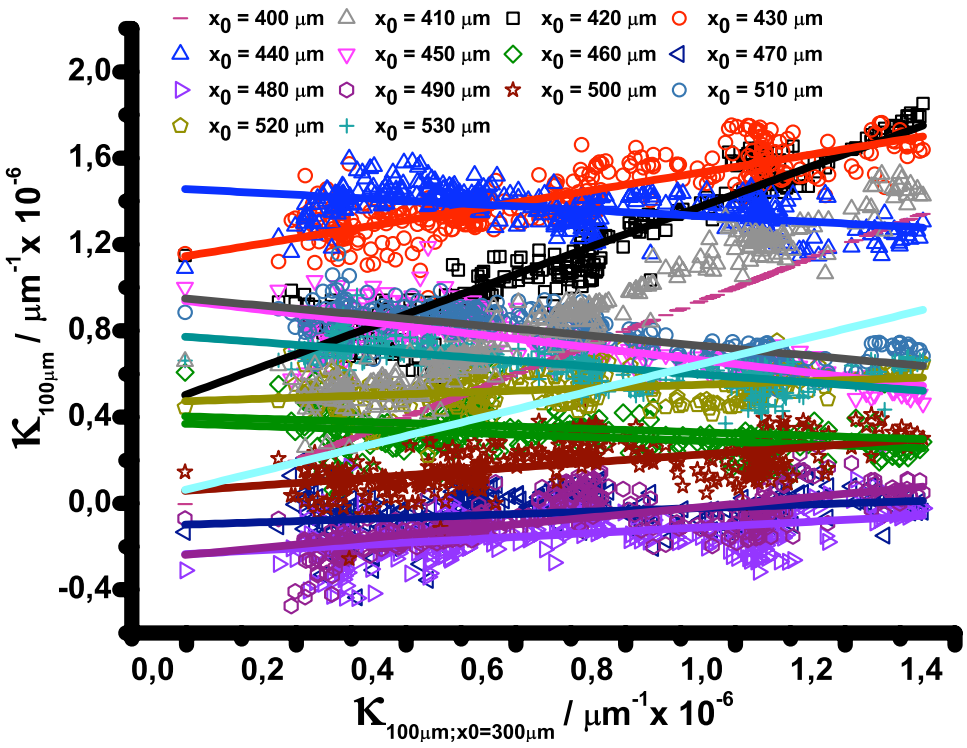

Figure A. 5: Partially Au coated NMC (Δx = 100µm) x_0-investigation; determination of segment position NMC4 (Chapter 4.3.3).

x_0	m / a.u	b/ μm^{-1}	R_P /a.u
410	0,93	1,11× 10^{-7}	0,97
420	0,93	2,53× 10^{-7}	0,95
430	0,41	5,73× 10^{-7}	0,85
440	-0,13	7,28× 10^{-7}	-0,48

450	-0,29	$4{,}69\times 10^{-7}$	-0,77
460	-0,08	$1{,}85\times 10^{-7}$	-0,30
470	0,08	$-4{,}91\times 10^{-8}$	0,30
480	0,13	$-1{,}17\times 10^{-7}$	0,43
490	0,24	$-1{,}19\times 10^{-7}$	0,65
500	0,18	$2{,}96\times 10^{-8}$	0,56
510	0,08	$2{,}37\times 10^{-7}$	0,35
520	-0,23	$4{,}74\times 10^{-7}$	-0,73
530	-0,19	$3{,}86\times 10^{-7}$	-0,69

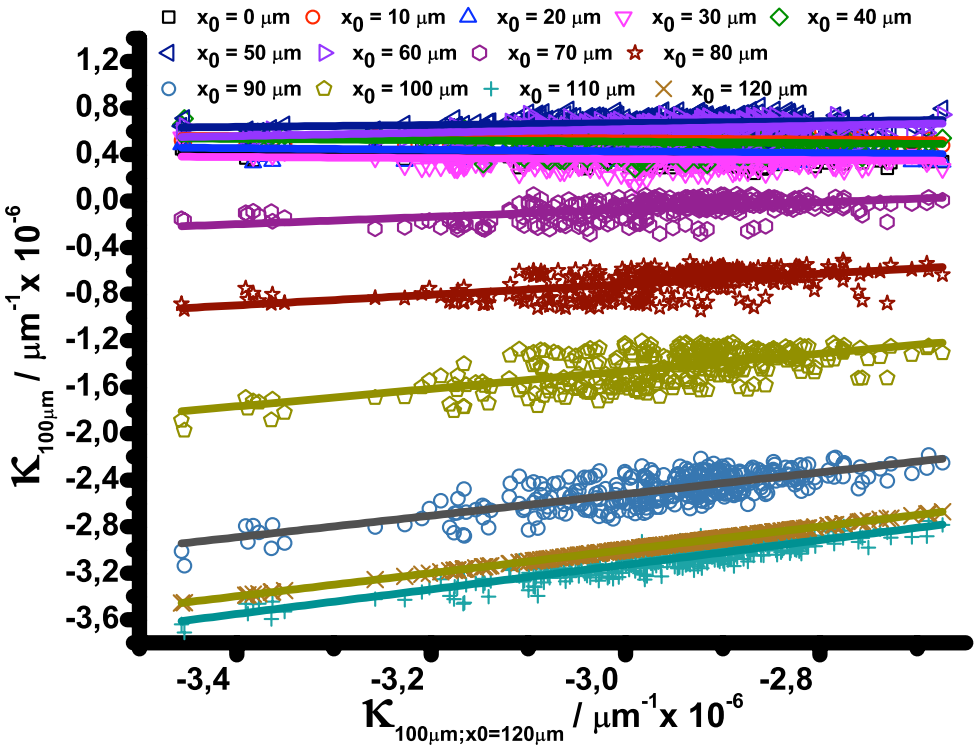

Figure A. 6: Polymer brush coated NMC (Δx = 100µm) x_0-investigation; determination of segment position apex (Chapter 4.3.4).

x_0	m / a.u	b/ μm^{-1}	R_P /a.u
0	-0,09	$5,75\times 10^{-8}$	-0,23
10	-0,05	$1,98\times 10^{-7}$	-0,12
20	-0,07	$1,08\times 10^{-7}$	-0,19
30	-0,04	$1,15\times 10^{-7}$	-0,08
40	-0,06	$1,65\times 10^{-7}$	-0,12
50	0,08	$4,58\times 10^{-7}$	0,16
60	0,15	$5,34\times 10^{-7}$	0,30
70	0,31	$4,34\times 10^{-7}$	0,49
80	0,45	$3,20\times 10^{-7}$	0,54
90	0,76	$4,02\times 10^{-7}$	0,63
100	0,93	$1,36\times 10^{-7}$	0,76
110	1,06	$2,57\times 10^{-8}$	0,90
120	1	0	1

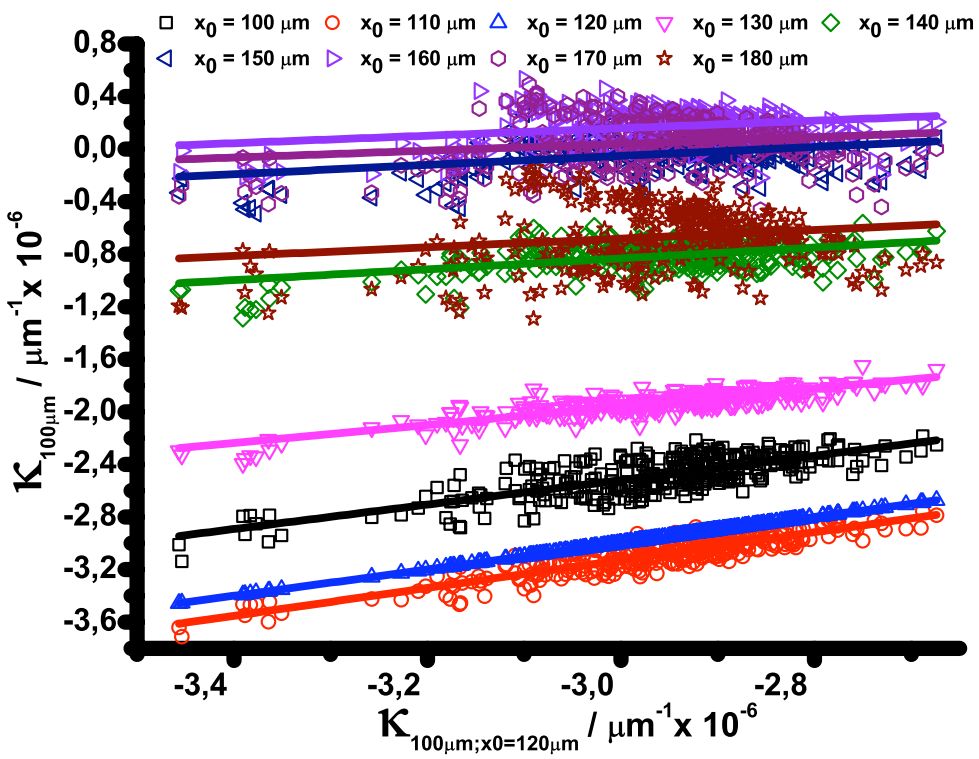

Figure A. 7: Polymer brush coated NMC (Δx = 100µm) x_0-investigation; determination of segment position apex (Chapter 4.3.4).

x_0	m / a.u	b/ µm^{-1}	R_P /a.u
100	0,93	1,36× 10^{-7}	0,76
110	1,06	2,57× 10^{-8}	0,90
120	1	0	1
130	0,69	5,75× 10^{-8}	0,86
140	0,41	2,03× 10^{-7}	0,47
150	0,35	4,91× 10^{-7}	0,38
160	0,28	5,07× 10^{-7}	0,27
170	0,26	4,08× 10^{-7}	0,18
180	0,33	1,55× 10^{-7}	0,18

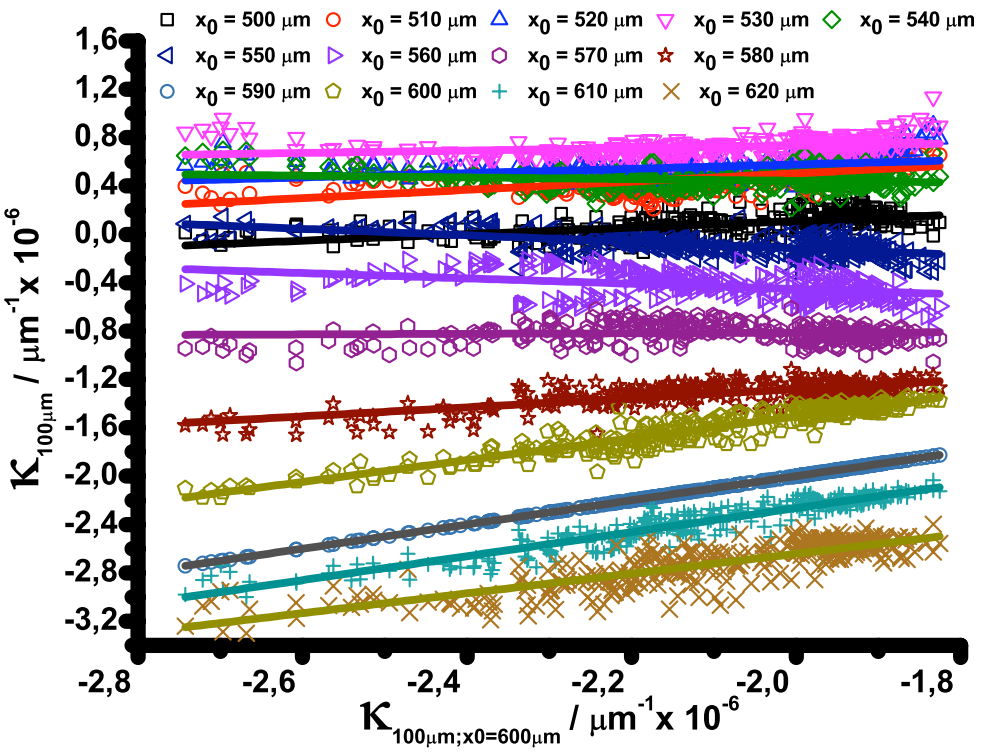

Figure A. 8: Polymer brush coated NMC (Δx = 100µm) x_0-investigation; determination of segment position tip (Chapter 4.3.4).

x_0	m / a.u	b/ µm^{-1}	R_P /a.u
500	0,27	3,26× 10^{-7}	0,56
510	0,34	5,95× 10^{-7}	0,62
520	0,18	4,67× 10^{-7}	0,43
530	0,10	4,66× 10^{-7}	0,26
540	-0,07	1,50× 10^{-7}	-0,19
550	-0,27	-3,27× 10^{-7}	-0,57
560	-0,22	-4,48× 10^{-7}	-0,41
570	0,02	-3,84× 10^{-7}	0,06
580	0,37	-2,65× 10^{-7}	0,73

590	0,90	$1,48\times 10^{-7}$	0,94
600	1	0	1
610	0,99	$-1,40\times 10^{-7}$	0,95
620	0,82	$-5,03\times 10^{-7}$	0,83

3. Roughness correlation in PMMA brushes

Summary of the obtained data of the investigated PMMA brushes for each investigated sample and segment (Chapter 7).

τ : exposition time; d : thickness; Γ : grafting density;

Σ : chain tethered density; R_c: lateral cutoff length; R_g: radius of gyration

Mn = 133000±6650 g/mol; PDI = 1,26; Rg = 8,32±0,21 nm

τ/min	d /nm	d/2Rg /a.u.	Γ /chains*nm²	Σ /a.u.	Rc /nm	Rc/2Rg /a.u.
35	56±1	3,37±0,10	0,30±0,02	66±1	125,5±4,3	7,54±0,32
45	42±1	2,52±0,09	0,23±0,01	50±1	165,4±7,4	9,94±0,51
50	40±1	2,40±0,09	0,21±0,01	47±1	202,1±11,1	12,15±0,73
60	37±1	2,22±0,08	0,20±0,01	44±1	134,8±4,9	8,10±0,36

Mn = 89000±4450 g/mol; PDI = 1,12; Rg = 6.80±0,17 nm

τ/min	d /nm	d/2Rg /a.u.	Γ /chains*nm²	Σ /a.u.	Rc /nm	Rc/2Rg /a.u.
35	31±1	2,28±0,09	0,25±0,02	36±1	139,9±5,3	10,28±0,47
40	27±1	1,99±0,09	0,21±0,01	32±1	173,3±8,1	12,73±0,68
50	24±1	1,76±0,09	0,19±0,01	28±1	173,3±8,1	12,73±0,68
55	22±1	1,62±0,08	0,17±0,01	26±1	173,3±8,1	12,73±0,68

Mn = 78000±3900 g/mol; PDI = 1,13; Rg = 6,37±0,16 nm

τ/min	d /nm	d/2Rg /a.u.	Γ /chains*nm²	Σ /a.u.	Rc /nm	Rc/2Rg /a.u.
5	25±1	1,96±0,09	0,23±0,02	29±1	121,3±3,9	9,52±0,39
5	21±1	1,61±0,09	0,19±0,01	24±1	110,6±3,3	8,68±0,34
10	21±1	1,64±0,09	0,19±0,01	25±1	139,9±5,3	10,98±0,49
20	18±1	1,41±0,09	0,17±0,01	21±1	158,2±6,8	12,42±0,61
25	13±1	1,04±0,08	0,12±0,01	15±1	141,6±5,4	11,11±0,51
30	10±1	0,75±0,08	0,08±0,01	11±1	136,1±5,0	10,69±0,48
35	10±1	0,79±0,08	0,09±0,01	12±1	176,9±8,5	13,89±0,75
40	10±1	0,76±0,08	0,09±0,01	11±1	252,8±17,3	19,85±1,45
45	9±1	0,72±0,08	0,09±0,01	11±1	252,8±17,3	19,85±1,45
50	8±1	0,63±0,08	0,07±0,01	9±1	252,8±17,3	19,85±1,45
55	7±1	0,57±0,08	0,07±0,01	9±1	393,3±41,9	30,87±3,38
60	7±1	0,55±0,08	0,06±0,01	8±1	252,8±17,3	19,85±1,45

Mn = 121300±6065 g/mol; PDI = 1,21; Rg = 7,94±0,20 nm

τ/min	d /nm	d/2Rg /a.u.	Γ /chains*nm²	Σ /a.u.	Rc /nm	Rc/2Rg /a.u.
18	46±1	2,89±0,10	0,27±0,01	54±1	104,8±3,0	6,60±0,25
16	44±1	2,77±0,09	0,26±0,01	52±1	98,9±2,6	6,23±0,23
14	47±1	2,98±0,10	0,28±0,02	55±1	107,9±3,2	6,79±0,26
11	50±1	3,15±0,10	0,30±0,02	59±1	98,9±2,6	6,23±0,23
8	53±1	3,33±0,10	0,31±0,02	62±1	122,9±4,1	7,74±0,32
6	57±1	3,59±0,11	0,34±0,02	67±1	148,5±6,0	9,35±0,44

Mn = 81100±4055 g/mol; PDI = 1,36; Rg = 6,49±0,16 nm

τ/min	d /nm	d/2Rg /a.u.	Γ /chains*nm²	Σ /a.u.	Rc /nm	Rc/2Rg /a.u.
6	41±1	3,17±0,11	0,36±0,02	48±1	104,8±3,0	8,07±0,31
8	39±1	2,98±0,11	0,34±0,02	45±1	104,8±3,0	8,07±0,31
11	37±1	2,88±0,10	0,33±0,02	44±1	98,9±2,7	7,62±0,28
14	34±1	2,65±0,10	0,30±0,02	40±1	104,8±3,0	8,07±0,31
16	33±1	2,53±0,10	0,29±0,02	39±1	104,8±3,0	8,07±0,31
18	33±1	2,53±0,10	0,29±0,02	38±1	101,8±2,8	7,84±0,29

Mn = 60300±3015 g/mol; PDI = 1,29; Rg = 5,60±0,14 nm

τ/min	d /nm	d/2Rg /a.u.	Γ /chains*nm²	Σ /a.u.	Rc /nm	Rc/2Rg /a.u.
18	28±1	2,46±0,11	0,33±0,02	32±1	122,9±4,1	10,97±0,46
6	30±1	2,64±0,11	0,35±0,02	35±1	104,8±3,0	9,36±0,35

Mn = 73000±3650 g/mol; PDI = 1,29; Rg = 6,16±0,15 nm

τ/min	d /nm	d/2Rg /a.u.	Γ /chains*nm²	Σ /a.u.	Rc /nm	Rc/2Rg /a.u.
6	27±1	2,18±0,10	0,26±0,02	32±1	153,8±6,4	12,48±0,61
3	33±1	2,67±0,11	0,33±0,02	39±1	131,8±4,7	10,70±0,47

Mn = 101600±5080 g/mol; PDI = 1,20; Rg = 7,27±0,18 nm

τ/min	d /nm	d/2Rg /a.u.	Γ /chains*nm²	Σ /a.u.	Rc /nm	Rc/2Rg /a.u.
5	9±1	0,59±0,07	0,06±0,01	10±1	505,7±69,1	34,78±4,84
10	7±1	0,45±0,07	0,05±0,01	8±1	884,9±211,9	60,86±14,65
15	5±1	0,32±0,07	0,03±0,01	5±1	-	-
20	5±1	0,32±0,07	0,03±0,01	5±1	-	-

Bibliography

1. Zhao, B.; Brittain, W. J. *Progress In Polymer Science* **2000,** 25, (5), 677-710.

2. Barbey, R.; Lavanant, L.; Paripovic, D.; Schuewer, N.; Sugnaux, C.; Tugulu, S.; Klok, H. *Chem. Rev.* **2009,** 109, (11), 5437-5527.

3. Berger, R.; Cheng, Y.; Foerch, R.; Gotsmann, B.; Gutmann, J. S.; Pakula, T.; Rietzler, U.; Schaertl, W.; Schmidt, M.; Strack, A.; Windeln, J.; Butt, H. *Langmuir* **2007,** 23, (6), 3150-3156.

4. Mamin, H. J.; Ried, R. P.; Terris, B. D.; Rugar, D. *Proceedings Of The Ieee* **1999,** 87, (6), 1014-1027.

5. Ling, Q.; Liaw, D.; Zhu, C.; Chan, D. S.; Kang, E.; Neoh, K. *Progress In Polymer Science* **2008,** 33, (10), 917-978.

6. Gotsmann, B.; Duerig, U.; Frommer, J.; Hawker, C. J. *Advanced Functional Materials* **2006,** 16, (11), 1499-1505.

7. Golriz, A. A.; Kaule, T.; Heller, J.; Untch, M. B.; Schattling, P.; Theato, P.; Toda, M.; Yoshida, S.; Ono, T.; Butt, H.; Gutmann, J. S.; Berger, R. *Nanoscale* **2011,** 3, (12), 5049-5058.

8. Klein, J. *Annual Review Of Materials Science* **1996,** 26, 581-612.

9. Joanny, J. F. *Langmuir* **1992,** 8, (3), 989-995.

10. Raviv, U.; Giasson, S.; Kampf, N.; Gohy, J. F.; Jerome, R.; Klein, J. *Nature* **2003,** 425, (6954), 163-165.

11. Senaratne, W.; Andruzzi, L.; Ober, C. K. *Biomacromolecules* **2005,** 6, (5), 2427-2448.

12. Andruzzi, L.; Senaratne, W.; Hexemer, A.; Sheets, E. D.; Ilic, B.; Kramer, E. J.; Baird, B.; Ober, C. K. *Langmuir* **2005,** 21, (6), 2495-2504.

13. Minko, S. *Polym. Rev.* **2006,** 46, (4), 397-420.

14. Papaefthimiou, V.; Steitz, R.; Findenegg, G. H. *Chem. Unserer Zeit* **2008,** 42, (2), 102-115.

15. Ionov, L.; Minko, S.; Stamm, M.; Gohy, J. F.; Jerome, R.; Scholl, A. *J. Am. Chem. Soc.* **2003,** 125, (27), 8302-8306.

16. Stuart, M. A. C.; Huck, W. T. S.; Genzer, J.; Mueller, M.; Ober, C.; Stamm, M.; Sukhorukov, G. B.; Szleifer, I.; Tsukruk, V. V.; Urban, M.; Winnik, F.; Zauscher, S.; Luzinov, I.; Minko, S. *Nature Materials* **2010,** 9, (2), 101-113.

17. Advincula, R. C., *Polymer brushes : Synthesis, Characterization, Applications*. 2004.

18. Degennes, P. G. *Macromolecules* **1980,** 13, (5), 1069-1075.

19. Milner, S. T.; Witten, T. A.; Cates, M. E. *Macromolecules* **1988,** 21, (8), 2610-2619.

20. Muller, M. *Physical Review E* **2002,** 65, (3), 030802.

21. Butt, H. J. *J. Colloid Interface Sci.* **1996,** 180, (1), 251-260.

22. Lenz, S.; Nett, S. K.; Memesa, M.; Roskamp, R. F.; Timmann, A.; Roth, S. V.; Berger, R.; Gutmann, J. S. *Macromolecules* **2010,** 43, (2), 1108-1116.

23. Lenz, S.; Ruehm, A.; Major, J.; Berger, R.; Gutmann, J. S. *Macromolecules* **2010,** 44, (2), 360-367.

24. Brittain, W. J.; Minko, S. *Journal Of Polymer Science Part A-Polymer Chemistry* **2007,** 45, (16), 3505-3512.

25. Kent, M. S. *Macromolecular Rapid Communications* **2000,** 21, (6), 243-270.

26. Wu, T.; Efimenko, K.; Genzer, J. *J. Am. Chem. Soc.* **2002,** 124, (32), 9394-9395.

27. Alexander, S. *Journal De Physique* **1977,** 38, (8), 983-987.

28. Milner, S. T.; Witten, T. A. *Journal De Physique* **1988,** 49, (11), 1951-1962.

29. Matyjaszewski, K.; Miller, P. J.; Shukla, N.; Immaraporn, B.; Gelman, A.; Luokala, B. B.; Siclovan, T. M.; Kickelbick, G.; Vallant, T.; Hoffmann, H.; Pakula, T. *Macromolecules* **1999,** 32, (26), 8716-8724.

30. Zhao, B.; He, T. *Macromolecules* **2003,** 36, (23), 8599-8602.

31. Zhao, B. *Polymer* **2003,** 44, (15), 4079-4083.

32. Brittain, W. J.; Boyes, S. G.; Granville, A. M.; Baum, M.; Mirous, B. K.; Akgun, B.; Zhao, B.; Blickle, C.; Foster, M. D. *Surface- Initiated Polymerization* **2006,** 198, 125-147.

33. Zhao, B.; Brittain, W. J.; Zhou, W. S.; Cheng, S. Z. D. *J. Am. Chem. Soc.* **2000,** 122, (10), 2407-2408.

34. Minko, S.; Usov, D.; Goreshnik, E.; Stamm, M. *Macromolecular Rapid Communications* **2001,** 22, (3), 206-211.

35. Minko, S.; Patil, S.; Datsyuk, V.; Simon, F.; Eichhorn, K. J.; Motornov, M.; Usov, D.; Tokarev, I.; Stamm, M. *Langmuir* **2002,** 18, (1), 289-296.

36. Draper, J.; Luzinov, I.; Ionov, L.; Minko, S.; Varshney, S. K.; Stamm, M. *Polymer Preprint (ACS)* **2003,** 225, U623-U624.

37. Zhao, B.; Haasch, R. T.; MacLaren, S. *J. Am. Chem. Soc.* **2004,** 126, (19), 6124-6134.

38. Santer, S.; Kopyshev, A.; Donges, J.; Ruehe, J.; Jiang, X.; Zhao, B.; Mueller, M. *Langmuir* **2007,** 23, (1), 279-285.

39. Santer, S.; Kopyshev, A.; Donges, J.; Yang, H. K.; Ruhe, J. *Langmuir* **2006,** 22, (10), 4660-4667.

40. Santer, S.; Kopyshev, A.; Yang, H. K.; Ruhe, J. *Macromolecules* **2006,** 39, (8), 3056-3064.

41. Wang, J.; Mueller, M. *J. Phys. Chem. B* **2009,** 113, (33), 11384-11402.

42. Muller, M.; Smith, G. D. *Journal Of Polymer Science Part B-Polymer Physics* **2005,** 43, (8), 934-958.

43. Wenning, L.; Muller, M.; Binder, K. *Europhysics Letters* **2005,** 71, (4), 639-645.

44. Tieke, B., *Makromolekulare Chemie*. 2005.

45. Chiefari, J.; Mayadunne, R. T. A.; Moad, C. L.; Moad, G.; Rizzardo, E.; Postma, A.; Skidmore, M. A.; Thang, S. H. *Macromolecules* **2003,** 36, (7), 2273-2283.

46. Barner-Kowollik, C.; Davis, T. P.; Heuts, J. P. A.; Stenzel, M. H.; Vana, P.; Whittaker, M. *Journal Of Polymer Science Part A-Polymer Chemistry* **2003,** 41, (3), 365-375.

47. Barner-Kowollik, C., *Handbook of RAFT Polymerization*. 2008.

48. Wang, J. S.; Matyjaszewski, K. *J. Am. Chem. Soc.* **1995,** 117, (20), 5614-5615.

49. Matyjaszewski, K.; Xia, J. H. *Chem. Rev.* **2001,** 101, (9), 2921-2990.

50. Kong, X. X.; Kawai, T.; Abe, J.; Iyoda, T. *Macromolecules* **2001,** 34, (6), 1837-1844.

51. Husseman, M.; Malmstrom, E. E.; McNamara, M.; Mate, M.; Mecerreyes, D.; Benoit, D. G.; Hedrick, J. L.; Mansky, P.; Huang, E.; Russell, T. P.; Hawker, C. J. *Macromolecules* **1999,** 32, (5), 1424-1431.

52. Pyun, J.; Jia, S. J.; Kowalewski, T.; Patterson, G. D.; Matyjaszewski, K. *Macromolecules* **2003,** 36, (14), 5094-5104.

53. Koylu, D.; Carter, K. R. *Macromolecules* **2009,** 42, (22), 8655-8660.

54. Gorman, C. B.; Petrie, R. J.; Genzer, J. *Macromolecules* **2008,** 41, (13), 4856-4865.

55. Turgman-Cohen, S.; Genzer, J. *J. Am. Chem. Soc.* **2011,** 133, (44), 17567-17569.

56. Devaux, C.; Chapel, J. P.; Beyou, E.; Chaumont, P. *European Physical Journal E* **2002,** 7, (4), 345-352.

57. Pasetto, P.; Blas, H.; Audouin, F.; Boissiere, C.; Sanchez, C.; Save, M.; Charleux, B. *Macromolecules* **2009,** 42, (16), 5983-5995.

58. Berger, R.; Delamarche, E.; Lang, H. P.; Gerber, C.; Gimzewski, J. K.; Meyer, E.; Guntherodt, H. J. *Science* **1997,** 276, (5321), 2021-2024.

59. Dutta, P.; Tipple, C. A.; Lavrik, N. V.; Datskos, P. G.; Hofstetter, H.; Hofstetter, O.; Sepaniak, M. J. *Analytical Chemistry* **2003,** 75, (10), 2342-2348.

60. Chen, T.; Chang, D. P.; Liu, T.; Desikan, R.; Datar, R.; Thundat, T.; Berger, R.; Zauscher, S. *Journal Of Materials Chemistry* **2010,** 20, (17), 3391-3395.

61. Thundat, T.; Oden, P. I.; Warmack, R. J. *Microscale Thermophys. Eng.* **1997,** 1, (3), 185-199.

62. Datar, R.; Kim, S.; Jeon, S.; Hesketh, P.; Manalis, S.; Boisen, A.; Thundat, T. *MRS Bull.* **2009,** 34, (6), 449-454.

63. Raiteri, R.; Grattarola, M.; Butt, H. J.; Skladal, P. *Sens. Actuator B-Chem.* **2001,** 79, (2-3), 115-126.

64. Yang, R.; Huang, X.; Wang, Z.; Zhou, Y.; Liu, L. *Sens. Actuator B-Chem.* **2010,** 145, (1), 474-479.

65. Lim, S.; Raorane, D.; Satyanarayana, S.; Majumdar, A. *Sens. Actuator B-Chem.* **2006,** 119, (2), 466-474.

66. Bumbu, G. G.; Kircher, G.; Wolkenhauer, M.; Berger, R.; Gutmann, J. S. *Macromol. Chem. Phys.* **2004,** 205, (13), 1713-1720.

67. Abu-Lail, N. I.; Kaholek, M.; LaMattina, B.; Clark, R. L.; Zauscher, S. *Sens. Actuator B-Chem.* **2006,** 114, (1), 371-378.

68. Zhou, F.; Biesheuvel, P. M.; Chol, E. Y.; Shu, W.; Poetes, R.; Steiner, U.; Huck, W. T. S. *Nano Lett.* **2008,** 8, (2), 725-730.

69. Zhou, F.; Shu, W. M.; Welland, M. E.; Huck, W. T. S. *J. Am. Chem. Soc.* **2006,** 128, (16), 5326-5327.

70. Jun, Z.; Berger, R.; Gutmann, J. S. *Appl. Phys. Lett.* **2006,** 89, (3), 33110-1-33110-33110-3.

71. Jung, N.; Jeon, S. *Macromolecules* **2008,** 41, (24), 9819-9822.

72. Jung, N.; Seo, H.; Lee, D.; Ryu, C. Y.; Jeon, S. *Macromolecules* **2008,** 41, (19), 6873-6875.

73. Toda, M.; Joseph, Y.; Berger, R. *Journal Of Physical Chemistry C* **2010,** 114, (5), 2012-2017.

74. Bumbu, G. G.; Wolkenhauer, M.; Kircher, G.; Gutmann, J. S.; Berger, R. *Langmuir* **2007,** 23, (4), 2203-2207.

75. Bradley, C.; Jalili, N.; Nett, S. K.; Chu, L.; Foerch, R.; Gutmann, J. S.; Berger, R. *Macromol. Chem. Phys.* **2009,** 210, (16), 1339-1345.

76. Toda, M.; Itakura, A. N.; Igarashi, S.; Buscher, K.; Gutmann, J. S.; Graf, K.; Berger, R. *Langmuir* **2008,** 24, (7), 3191-3198.

77. Jeon, S.; Thundat, T. *Appl. Phys. Lett.* **2004,** 85, (6), 1083-1084.

78. Lang, H. P.; Berger, R.; Andreoli, C.; Brugger, J.; Despont, M.; Vettiger, P.; Gerber, C.; Gimzewski, J. K.; Ramseyer, J. P.; Meyer, E.; Guntherodt, H. J. *Appl. Phys. Lett.* **1998,** 72, (3), 383-385.

79. Helm, M.; Servant, J. J.; Saurenbach, F.; Berger, R. *Appl. Phys. Lett.* **2005,** 87, (6), 3.

80. Wehrmeister, J.; Fuss, A.; Saurenbach, F.; Berger, R.; Helm, M. *Review of Scientific Instruments* **2007,** 78, (10), 9.

81. Martinez, N. F.; Kosaka, P. M.; Tamayo, J.; Ramirez, J.; Ahumada, O.; Mertens, J.; Hien, T. D.; Rijn, C. V.; Calleja, M. *Review of Scientific Instruments* **2010,** 81, (12), 125109.

82. Korsunsky, A. M.; Cherian, S.; Raiteri, R.; Berger, R. *Sensors And Actuators A-Physical* **2007,** 139, (1-2), 70-77.

83. Malacara, D. **2007**.

84. Hariharan, P.; Oreb, B. F.; Eiju, T. *Applied Optics* **1987,** 26, (13), 2504-2506.

85. Jaing, C.; Shie, Y.; Tang, C.; Liou, Y.; Chang, C.; Yang, C. *Optical Review* **2009,** 16, (2), 170-172.

86. Cavaliere, A. Development of a microcantilever deflection detection method based on Phase Shifting Interferometry. 2009.

87. Katherine, C. *Progress in Optics* **1988,** 26, 349-393.

88. Goldstein, R. M.; Zebker, H. A.; Werner, C. L. *Radio Science* **1988,** 23, (4), 713-720.

89. Herraez, M. A.; Burton, D. R.; Lalor, M. J.; Gdeisat, M. A. *Applied Optics* **2002,** 41, (35), 7437-7444.

90. Lukacs, G.; Maloney, N.; Hegner, M. *Journal of Sensors* **2011**.

91. Bietsch, A.; Zhang, J. Y.; Hegner, M.; Lang, H. P.; Gerber, C. *Nanotechnology* **2004,** 15, (8), 873-880.

92. Deegan, R. D.; Bakajin, O.; Dupont, T. F.; Huber, G.; Nagel, S. R.; Witten, T. A. *Nature* **1997,** 389, (6653), 827-829.

93. Liu, T.; Pihan, S.; Roth, M.; Retsch, M.; Jonas, U.; Gutmann, J. S.; Koynov, K.; Butt, H.; Berger, R. *Macromolecules* **2012,** 45, (2), 862-871.

94. Tolan, M., *X-ray scattering from Soft-Matter Thin Films*. 1999.

95. Russell, T. P. *Materials Science Reports* **1990,** 5, (4), 171-271.

96. Parratt, L. G. *Physical Review* **1954,** 95, (2), 359-369.

97. http://www.ncnr.nist.gov/resources/sldcalc.html.

98. Lenz, S.; Bonini, M.; Nett, S. K.; Lechmann, M. C.; Emmerling, S. G. J.; Kappes, R. S.; Memesa, M.; Timmann, A.; Roth, S. V.; Gutmann, J. S. *European Physical Journal-Applied Physics* **2010,** 51, (1), 10601.

99. Ilavsky, J.; Jemian, P. R. *Journal of Applied Crystallography* **2009,** 42, (2), 347-353.

100. Tidswell, I. M.; Rabedeau, T. A.; Pershan, P. S.; Kosowsky, S. D. *Physical Review Letters* **1991,** 66, (16), 2108-2111.

101. Grunberg, P.; Schreiber, R.; Pang, Y.; Brodsky, M. B.; Sowers, H. *Physical Review Letters* **1986,** 57, (19), 2442-2445.

102. Fullerton, E. E.; Kelly, D. M.; Guimpel, J.; Schuller, I. K.; Bruynseraede, Y. *Physical Review Letters* **1992,** 68, (6), 859-862.

103. Payne, A. P.; Clemens, B. M. *Phys. Rev. B* **1993,** 47, (4), 2289-2300.

104. Salditt, T.; Metzger, T. H.; Peisl, J.; Goerigk, G. *Journal Of Physics D-Applied Physics* **1995,** 28, (4A), A236-A240.

105. Salditt, T.; Metzger, T. H.; Peisl, J.; Reinker, B.; Moske, M.; Samwer, K. *Europhysics Letters* **1995,** 32, (4), 331-336.

106. Gibaud, A.; Cowlam, N.; Vignaud, G.; Richardson, T. *Physical Review Letters* **1995,** 74, (16), 3205-3208.

107. Timmann, A.; Doehrmann, R.; Schubert, T.; Schulte-Schrepping, H.; Hahn, U.; Kuhlmann, M.; Gehrke, R.; Roth, S. V.; Schropp, A.; Schroer, C.; Lengeler, B. *Review of Scientific Instruments* **2009,** 80, (4), 046103.

108. Roth, S. V.; Dohrmann, R.; Dommach, M.; Kuhlmann, M.; Kroger, I.; Gehrke, R.; Walter, H.; Schroer, C.; Lengeler, B.; Mueller-Buschbaum, P. *Review of Scientific Instruments* **2006,** 77.

109. Wolkenhauer, M.; Bumbu, G.; Cheng, Y.; Roth, S. V.; Gutmann, J. S. *Appl. Phys. Lett.* **2006,** 89, (5), 054101.

110. Garcia, R.; Perez, R. *Surface Science Reports* **2002,** 47, (6-8), 197-301.

111. Butt, H.; Graf, K.; Kappl, M., *Physics and Chemistry of Interfaces*. 2006.

112. Ade, H.; Hitchcock, A. P. *Polymer* **2008,** 49, (3), 643-675.

113. Stoehr, J., *NEXAFS Spectroscopy*. 1992.

114. Mezger, M.; Jerome, B.; Kortright, J. B.; Valvidares, M.; Gullikson, E. M.; Giglia, A.; Mahne, N.; Nannarone, S. *Phys. Rev. B* **2011,** 83, (15), 155406.

115. Roth, P. J.; Wiss, K. T.; Zentel, R.; Theato, P. *Macromolecules* **2008,** 41, (22), 8513-8519.

116. Kelling, S.; Paoloni, F.; Huang, J.; Ostanin, V. P.; Elliott, S. R. *Review of Scientific Instruments* **2009,** 80, (9), 093101.

117. Sappat, A. *ECTI-CON* **2011**, 34-37.

118. Lee, D.; Kim, S.; Jung, N.; Thundat, T.; Jeon, S. *Journal Of Applied Physics* **2009,** 106, (2), 024310.

119. Dohn, S.; Sandberg, R.; Svendsen, W.; Boisen, A. *Appl. Phys. Lett.* **2005,** 86, (23), 233501.

120. Luzinov, I.; Minko, S.; Tsukruk, V. V. *Progress In Polymer Science* **2004,** 29, (7), 635-698.

121. Prokhorova, S. A.; Kopyshev, A.; Ramakrishnan, A.; Zhang, H. N.; Ruhe, J. *Nanotechnology* **2003,** 14, (10), 1098-1108.

122. Draper, J.; Luzinov, I.; Minko, S.; Tokarev, I.; Stamm, M. *Langmuir* **2004,** 20, (10), 4064-4075.

123. Sidorenko, A.; Minko, S.; Schenk-Meuser, K.; Duschner, H.; Stamm, M. *Langmuir* **1999,** 15, (24), 8349-8355.

124. Zhao, B.; Haasch, R. T.; MacLaren, S. *Polymer* **2004,** 45, (23), 7979-7988.

125. Marko, J. F.; Witten, T. A. *Physical Review Letters* **1991,** 66, (11), 1541-1544.

126. Soga, K. G.; Zuckermann, M. J.; Guo, H. *Macromolecules* **1996,** 29, (6), 1998-2005.

127. Minko, S.; Luzinov, I.; Luchnikov, V.; Muller, M.; Patil, S.; Stamm, M. *Macromolecules* **2003,** 36, (19), 7268-7279.

128. Gall, W. G.; McCrum, N. G. *Journal Of Polymer Science* **1961,** 50, (154), 489-&.

129. Natta, G. *Journal Of Polymer Science* **1955,** 16, (82), 143-154.

130. Edwards, S. F.; Vilgis, T. *Polymer* **1986,** 27, (4), 483-492.

131. Urayama, K.; Yamamoto, S.; Tsujii, Y.; Fukuda, T.; Neher, D. *Macromolecules* **2002,** 35, (25), 9459-9465.

132. Nett, S. K. Dissertation : Functional Polymer Coatings - µ-Pattering and µ-Analysis. Dissertation, Johannes Gutenberg University Mainz, 2009.

133. Muller-Buschbaum, P.; Gutmann, J. S.; Lorenz, C.; Schmitt, T.; Stamm, M. *Macromolecules* **1998,** 31, (26), 9265-9272.

134. Muller-Buschbaum, P.; Stamm, M. *Macromolecules* **1998,** 31, (11), 3686-3692.

135. Gutmann, J. S.; Muller-Buschbaum, P.; Schubert, D. W.; Stribeck, N.; Stamm, M. *Journal Of Macromolecular Science-Physics* **1999,** B38, (5-6), 563-576.

136. Kraus, J.; Muller-Buschbaum, P.; Bucknall, D. G.; Stamm, M. *Journal Of Polymer Science Part B-Polymer Physics* **1999,** 37, (20), 2862-2874.

137. Gutmann, J. S.; Muller-Buschbaum, P.; Schubert, D. W.; Stribeck, N.; Smilgies, D.; Stamm, M. *Physica B* **2000,** 283, (1-3), 40-44.

138. Shin, K.; Pu, Y.; Rafailovich, M. H.; Sokolov, J.; Seeck, O. H.; Sinha, S. K.; Tolan, M.; Kolb, R. *Macromolecules* **2001,** 34, (16), 5620-5626.

139. Akgun, B.; Brittain, W. J.; Li, X. F.; Wang, J.; Foster, M. D. *Macromolecules* **2005,** 38, (21), 8614-8616.

140. Jung, Y.; Kline, R. J.; Fischer, D. A.; Lin, E. K.; Heeney, M.; McCulloch, I.; DeLongchamp, D. M. *Advanced Functional Materials* **2008,** 18, (5), 742-750.

141. Hung, L. S.; Chen, C. H. *Materials Science & Engineering R-Reports* **2002,** 39, (5-6), 143-222.

142. Emmerling, S. G. J.; Langer, L. B. N.; Pihan, S. A.; Lellig, P.; Gutmann, J. S. *Macromolecules* **2010,** 43, (11), 5033-5042.

143. Mol, E. A. L.; Wong, G. C. L.; Petit, J. M.; Rieutord, F.; deJeu, W. H. *Physical Review Letters* **1997,** 79, (18), 3439-3442.

144. Schafer, D.; Mueller, M.; Bonn, M.; Marr, D. W. M.; van Maarseveen, J.; Squier, J. *Optics Letters* **2009,** 34, (2), 211-213.

145. Roth, S. V.; Herzog, G.; Koerstgens, V.; Buffet, A.; Schwartzkopf, M.; Perlich, J.; Kashem, M. M. A.; Doehrmann, R.; Gehrke, R.; Rothkirch, A.; Stassig, K.; Wurth, W.; Benecke, G.; Li, C.; Fratzl, P.; Rawolle, M.; Mueller-Buschbaum, P. *Journal Of Physics-Condensed Matter* **2011,** 23, (25), 254208.

Abbreviations

1D	one-dimensional
2D	two-dimensional
3D	three-dimensional
A	area
AA	acetic acid
AIBN	azobisisobutyronitrile
APDES	(3-Aminopropyl)dimethylethoxysilan
ATRP	Atom transfer radical polymerization
b	y-intercept
CCD	charge-coupled device
d	film thickness
DCM	dichloromethane
E	elastic modulus
eV	electron volt
F	free energy
F(q)	form factor
FT-IR	Fourier transform infrared
GISAXS	grazing incidence small angle X-ray scattering
GPC	gel permeation chromatography
Hz	hertz
I	initiator
I(q)	intensity
iβ	refractive index (imaginary part)
K	packing factor
k	wave vector
m	slop
M	monomer
M_n	number average molecular weight

N	newton
n	refractive index
N_A	Avogadro constant
NEXAFS	near edge X-ray absorption fine structure
NMC	nanomechanical cantilever
NMR	nuclear magnetic resonance
NMRP	nitroxide mediated radical polymerization
P	Porod regime exponent
p	pressure
PDI	polydispersity index
PFP	pentafluorophenol
PMMA	poly(methyl methacrylate)
PNIPAAM	poly(N-isopropylacrylamide)
PS	polystyrene
PSI	phase shifting interferometry/interferometer
q	wave vector transfer
r	reflected amplitude
r_0	electron radius
$\overline{R}$	Fresnel reflectivity
RAFT	reversible addition-fragmentation chain transfer
R_c	lateral cutoff length
R_g	radius of gyration
R_P	Pearson R
rpm	rounds per minute
s	seconds
S(q)	interference function
SAM	self assembled monolayer
SEM	scanning electron microscopy
SFM	scanning force microscpoy
SLD	scattering length density
SPM	scanning probe microscopy
T	temperature

T_g	glass transition temperature
THF	tetrahydrofuran
x_0	NMC segment starting position
Δx	NMC segment size
XPS	X-ray photoelectron spectroscopy
XRR	X-ray reflectivity
α_i	incident angle
α_c	critical angle
α_f	exit angle; reflected beam
α_t	exit angle; transmitted beam
β_{ref}	refractive index (imaginary part)
Γ	grafting density
Δ	delta/change
ρ	density
δ_{ref}	refractive index (real part)
Θ	exit angle parallel to the surface
κ	curvature
λ	wavelength
μ	micro
μ_{abs}	mass absorption coefficient
ν	Poison ratio
ξ	radius of correlation
ρ_{el}	electron density
Σ	chain tethered density
σ	stress
σ_{av}	standard deviation
σ_{rms}	root mean squared roughness
τ	exposition time
φ	phase